Hydraulically-Actuated Microscale Traveling Energy Recovery

by

Michael F. Robbins

S.B. EE, M.I.T., 2008

Submitted to the Department of Electrical Engineering and Computer Science

in Partial Fulfillment of the Requirements for the Degree of

Master of Engineering in Electrical Engineering and Computer Science

at the Massachusetts Institute of Technology

June, 2009

Author_____
Department of Electrical Engineering and Computer Science
May 08, 2009

Certified by_____
Elliot Ranger
Group Leader, Charles Stark Draper Laboratory
VI-A Company Thesis Supervisor

Certified by_____
Joeseph A. Paradiso
Associate Professor, M.I.T. Media Lab
M.I.T. Thesis Supervisor

Accepted by_____
Arthur C. Smith
Professor of Electrical Engineering
Chairman, Department Committee on Graduate Theses

[This page intentionally left blank.]

Hydraulically-Actuated Microscale Traveling Energy Recovery

by

Michael F. Robbins

Submitted to the
Department of Electrical Engineering and Computer Science

May 22, 2009

in Partial Fulfillment of the Requirements for the Degree of
Master of Engineering in Electrical Engineering and Computer Science

ABSTRACT

As the demand for portable electrical power grows, alternatives to chemical stored energy may enable users with additional system capabilities. This thesis presents a miniature hydroelectric turbine system for use in wearable energy harvesting applications. A radial outflow turbine, which trades performance for manufacturability, is designed and built. A permanent magnet generator is designed and embedded within the turbine to enable a compact overall system. Fluidic rectification is pursued with the goal of harnessing more of the available mechanical power. A method for reliably conveying pressurized fluid to and from the shoe is developed. Results for the turbine and generator system are presented under a variety of test conditions.

Thesis Supervisor: Elliot Ranger
Title: Mixed-Signal Group Leader

Thesis Advisor: Joseph A. Paradiso
Title: Associate Professor

[This page intentionally left blank.]

ACKNOWLEDGEMENTS

This thesis was prepared at The Charles Stark Draper Laboratory, Inc., under an Internal Research and Development program.

Publication of this thesis does not constitute approval by Draper of the findings or conclusions contained herein. It is published for the exchange and stimulation of ideas.

Many thanks to Elliot Ranger for being an excellent mentor at Draper, and for offering me a wide range of interesting opportunities and challenges over the past three years. The balance between guidance and independence during the course of this project has been immensely rewarding for me. I am grateful to have worked under his supervision and hope that many future students will have the opportunity to do so.

Special thanks to Joe Paradiso for welcoming me into the Responsive Environments Group at the Media Lab, and providing both useful context and technical insights into this project topics. His knowledge and intuition about systems and design at all levels has challenged me to think across engineering domains, and has inspired me to consider the hard questions at every turn.

To Don Fyler and Andrew Pinkham at Draper, who provided useful guidance on the electromagnetics design, and to Steve Bellio at Draper, who helped me implement the turbine test setup.

To Mark Belanger, Fred Cote, and Tony Caloggero at the MIT Edgerton Center Student Machine Shop, and to Tom Lutz at the MIT Media Lab Machine Shop, and to Tom Howe at Draper's AVL shop, who were all helpful at various points in teaching me the multitude of machining skills needed for this project, and ultimately for helping bring this design from paper to metal.

To Rob Truax, for providing a mechanical engineer's perspective on many critical design issues. To Humberto Evans, for indirectly helping me write this document with a daily mix of challenging technical questions and motivation to keep going.

Finally, to my parents and my sister, for their constant love, encouragement, and unwavering confidence in me.

---------- --

Michael F. Robbins

[This page intentionally left blank.]

Table of contents

List of figures

List of tables

1 Introduction

1.1 Portable Power Demand

As mobile electronics become more and more pervasive in our lives, the demand for mobile electrical power has grown. Most portable devices today rely on batteries, which store electrical energy in chemical form. The electrochemical potential of reactions within the battery are used to drive current through a load. In its simplest form, a battery is simply a place to store a fixed amount of energy:

$$(\text{Power}\,[W]) \times (\text{Time}\,[\text{hr}]) = (\text{Energy Density}\,[\frac{W\,\text{hr}}{\text{kg}}]) \times (\text{Battery Mass}\,[\text{kg}]) \tag{1}$$

With typical energy densities for today's common lithium polymer (Li-Po) batteries on the order of 100 to 200 $\frac{W\,\text{hr}}{\text{kg}}$, limited by current electrochemistry, a tradeoff emerges between device power consumption, battery lifetime, and mass.

Fortunately for the average person, the battery lifetime of many devices (most cell phones, some laptops, etc.) has reached a point where once-daily charging is sufficient to keep the device alive for typical use profiles. Since people tend to sleep once per 24-hour period under normal circumstances, this also provides a time for portable devices to be temporarily connected to a wired charging system. In the consumer space, advances in battery energy density beyond this point will typically lead either to lighter batteries, or to enabling higher power-consumption features. Such features may include higher-data-rate wireless links (where an increase in channel bandwidth requires an increase in transmit power to maintain the same SNR over a white-noise background), larger or higher-brightness displays (where backlight power consumption often dominates), or advanced computational capability (like 3D graphics rendering).

However, for some military uses in particular, there are several differences from the consumer case. First, the amount of power needed is often significantly higher, with the need for long-range radio links, bright outdoor-visible displays, special equipment like tactical flashlights, laser rangefinders, and other sensors, and more. Second, the assumption of once-daily charging is no longer appropriate, as access to wall power may not be frequent or reliable. According to the U.S. Department of Defense, "future warfighters will carry about 9kg of batteries to complete a 96 hour mission" [13]. At more than 12% of the mass of the typical 70kg soldier, these batteries represent a significant extra weight to be carried, adding fatigue and reducing maneuverability.

Additionally, in the consumer space, power tends to be a dominant engineering constraint for portable devices. If this constraint is eased, it might lead to features yet unimagined. This could include higher-frequency updates for wearable health monitoring systems, or smaller wearable communications devices.

One often overlooked approache to reducing this burden is to generate power through the user's normal body motion. While there are many possible places to extract power, the footstep/walking motion presents an especially concentrated power opportunity, and also allows for a device to be included in footwear. There is an upcoming and immediate need for wearable power generation, and the focus of this project is to design and prototype a system to efficiently extract energy and supply electricity to the user.

1.2 Wearable Energy Harvesting Systems

One early motivation for wearable energy recovery was in powering artifical organs, dating back to at least 1971, although these systems did not produce electrical power [10][11]. In a 1995 project, the focus was still on artificial organs, though now electrical energy was

the target [1]. As electronics miniaturization has proceeded particularly over the last decade, a new target has taken shape: power for mobile electronics.

A study of several methods of wearable energy harvesting mechanisms was conducted, including solar, RF, thermal, respiration, blood pressure, inertial proof masses, keyboard typing force, pedaling, and walking [17]. One conclusion of the survey was that for power on the scale of more than a few milliWatts, extracting footstep energy was the primary possibility without overly burdening the user.

There are a few other wearable energy opportunities also worth mentioning, including a backpack-mounted proof mass system, where the vertically-translating mass drives a rack and pinion to drive an electromagnetic generator. This system extracts 7.4 W while walking with a 38kg load [14]. Another project focused on extracting energy from knee motion, driving a brushless motor with a knee brace, and captured 7.0 W while walking, and even generated 4.8 W when configured only to extract energy when the knee was decelerating [3].

1.3 Footstep Energy Harvesting Systems

1.3.1 Energy Availability

For a 70kg user (including equipment/backpack weight) pushing through a 3mm shoe sole displacement, there is roughly

$$E_{\text{push}} = (70\text{kg})(9.81\frac{m}{s^2})(3\frac{\text{mm}}{\text{push}}) = 2.06\,\frac{\text{Joules}}{\text{push}} \tag{2}$$

available per compression. For one shoe, two pushes (heel and ball) per footstep, and one full cycle per second (one footstep per foot), there is approximately

$$P_{\text{shoe}} = (2.06\,\frac{\text{Joules}}{\text{push}})(2\,\frac{\text{pushes}}{\text{step}})(1\frac{\text{step}}{\text{second}}) = 4.12\,\text{Watts} \tag{3}$$

of mechanical power that is theoretically extractable from a single shoe, or 8.24 Watts for a pair of shoes. These levels are directly proportional to the 3mm displacement distance. (For comparison, the recent DOD energy storage competition requested a wearable device to generate 20 Watts average electrical power over a 96 hour mission [13].)

The displacement distance must result from a balance between energy and comfort, as (unlike a normal "springy" shoe material) most of the work done will not be returned to the wearer. However, experience with shoes and insoles leads the author to believe that this optimum will occur between 1mm to 1cm displacement.

1.3.2 Biophysics of Walking

To get a better sense of the energy that might be extracted, the literature provides data about the forces and pressures involved in a footstep. While we would like to be able to distinguish between the front and back strike events, the data collected to date presents only aggregate force and pressure profiles.

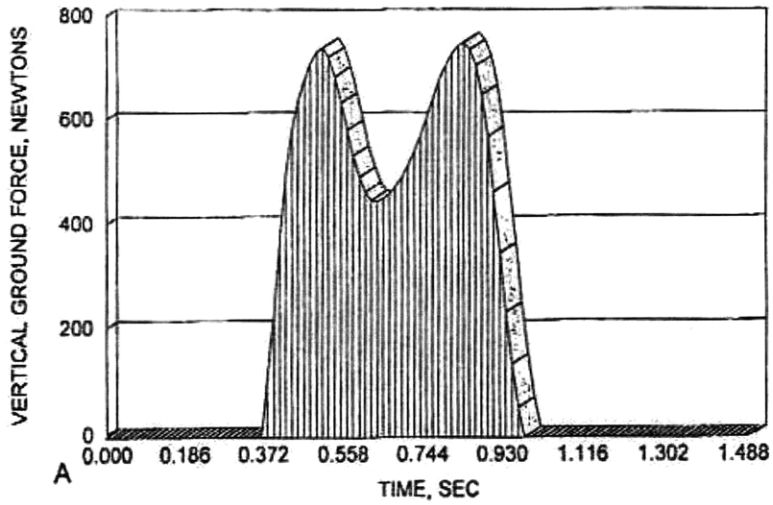

Figure 1. Force profile of a single step, 70kg person walking, from [1]

In Figure 1, the two peaks are clearly visible, which the original article characterizes as "a double peak at approximately 1.2 times the body weight, occurring as a result of the heel strike and forefront push-off" [1].

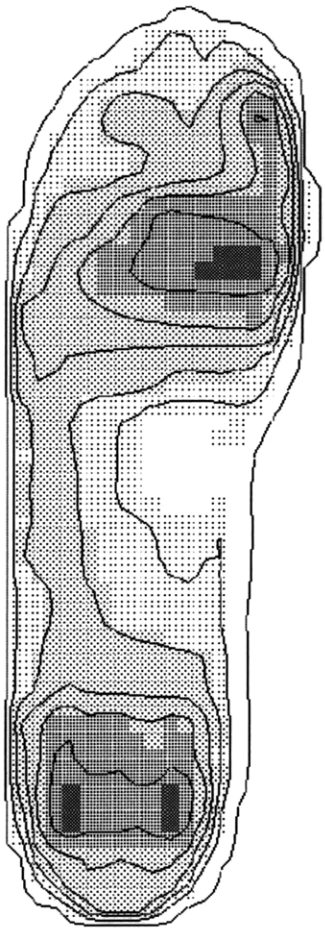

Figure 2. 50kPa contours of peak pressure while running in "well-cushioned" shoes, from [16]

In Figure 2, the peak pressure contours during a running step are shown. There are two

regions which reach $\geqslant$300kPa pressure: one at the heel, and one at the ball of the foot.

While Figure 2 is for running and we are designing a system for walking conditions, it is still useful for estimating the area over which we should expect to see the user's weight distributed. Clearly, by quasistatic force balance assuming the shoe is in contact with the non-accelerating ground, the user's applied weight at a moment in time (like that shown in Figure 1) must be balanced by the area integral of the pressure in the sole pushing up on the foot.

$$F(t) = \int\int P(\bullet)\,\mathrm{dA} \tag{4}$$

Since the force is effectively set by the user's weight (and gait, to a lesser extent), the area is important in determining the pressure at which our hydraulic system will be able to operate.

1.3.3 Prior Implementations

There are several existing implementations of shoe-mounted energy scavengers. For the following description, I consider electrical power to be "regulated" if it offers a predominantly DC voltage at the rated power, and "unregulated" if it instead consists predominantly of voltage impulses corresponding to the step frequency and higher.

A system which uses a mechanical advantage of 35:1 to stress piezoelectric cylinders can produce 300-600mW unregulated average electrical power out [1]. A system which uses a bending dual opposing piezoelectric unimorphs produced on the order of 10mW of regulated average electrical power out, and demonstrated a (best-known) electrical regulation

efficiency of 17.6% [15].

Another system used a dynamic capacitor with an electroelastomeric material, which was charged to several kilovolts and strained [9]. This is a similar concept to the piezoelectric systems, except that the bias is explicitly applied instead of being intrinsic to the long-term poling of the material. This group reported 0.8J per step, or 800mW if we use the same $1\frac{\text{step}}{s}$ rate as earlier. However, this does not appear to include electrical regulation efficiency, and the group also reported reliability issues in reaching beyond 10^5 steps.

Another project focused on conventional electromagnetic generation but with shoe integration in mind [6]. Using off-the-shelf DC motors as generators, a lever and gearbox were designed to capture heel strike energy. While no specific dimensions are given, the system was built into an approximately 3"x1.5"x0.75" package and fully embedded inside a conventional sneaker.

Demonstrating the continuing interest particularly from the military in this area of energy harvesting, an article still in press as of April 2009 describes a heel strike generator evaluated by the US Army which uses a lead screw and cam to transform the linear motion of a heel strike into a sinusoidal excitation of multiple piezoelectric elements [7]. The average regulated output power of this entire system was 93mW.

Another turbine-based implementation of a footstep energy harvesting system became known to this author in April 2009 as this document was being prepared. A group at NTT in Japan describes a vane motor turbine, described in more detail later. The authors claim power generation of 1.2 Watts under normal walking conditions [19]. As this work in Japan evolved essentially concurrently with this thesis, it supports the idea

that a turbine-based energy conversion approach may have promise.

Source	Year	Method	Power (regulated)	Power (unregulated)
[1]	1995	Piezo w/ amplification		300-600mW
[15]	1999	Piezo unimorph bending	10mW	
[6]	2000	Lever w/ electromagnetics		58mW*
[9]	2002	Electroelastomer		800mW
[19]	2008	Vane motor turbine	1200 mW	
[7]	2009	Piezo w/ leadscrew	93mW	

*58mW was delivered at low electrical impedance and in the correct voltage range, so regulation would not have caused significant losses.

Table 1. Survey of existing footstep energy scavengers.

Clearly, after examining Table 1 and comparing to the estimates of Equation 3, there is much performance left to be achieved. In particular, piezoelectric approaches trade a simplified mechanical design for lower potential power, plus additional difficulties in electrical conversion and a severe penalty in the electrical regulation efficiency. If we instead shift the problem and are willing to tackle a more complex mechanical system, we may be rewarded with greater overall system efficiency.

1.4 Mechanical to Electrical Conversion Mechanisms

1.4.1 Dynamic Capacitors

While capacitors are usually though of as purely electrical-domain devices, they can in fact be use to move energy between mechanical and electrical forms when the plates are allowed to move. In a familiar example of the coupling between electrical and mechanical domains, transformers in electronics often dissipate energy in friction and magnetostriction as the turns of nearby coils force each other together and apart due to work from the magnetic field, sometimes audible as a buzzing sound. This (unintentionally) couples

magnetic field energy into mechanical work, which is then dissipated as sound and heat (in addition to the heat produced by ohmic losses in the transformer). Similarly, although perhaps less familiar to the reader, a parallel-plate capacitor with moveable plates can be used to couple between mechanical work and the electric field. This technique is used frequently in MEMS devices such as accelerometers, which use this effect to actuate and measure moving multi-finger capacitor structures.

A parallel plate capacitor with plate area A, separator dielectric constant ε, and separation distance d has capacitance $C = \frac{\epsilon A}{d}$, and at voltage V stores energy

$$W = \frac{1}{2}CV^2 = \frac{Q^2}{2C} = \frac{Q^2}{2\epsilon A}d \tag{5}$$

in the electric field. The opposite charges on the plates will naturally want to attract each other together. However, if the capacitor is kept open-circuit (keeping Q constant) and an external force $F = \frac{\partial W}{\partial d} = \frac{Q^2}{2\epsilon A}$ is applied to gradually increase the separation distance d, mechanical work can be converted to additional energy in the electric field.

$$\Delta W_{1\to 2} = \left(\frac{Q^2}{2\epsilon A}\right)(d_2 - d_1) \tag{6}$$

In this case, the increase in stored electrical energy is directly proportional to the displacement.

Similar calculations can be made while holding the capacitor at constant-voltage instead of constant-charge, but again it is found that energy can be coupled between mechanical and electrical domains.

The implementation of this kind of device faces several hurdles not expressed in the math above. First of all, most commonly-used high-ϵ materials are solids, intended to act as physical insulators to prevent the plates from physically touching. They would most

likely crack under the large deformations needed here, and in any case would not be conformal to the expansions, which would reflect uncaptured energy. Second, even if a high-ϵ liquid like specialized oils were used, and some sort of thin insulation were also present to prevent the plates from directly contacting, there is always some voltage at which dielectric breakdown will occur. Also, the areas involved are small if any practical energy is to be realized. Practical discrete capacitors involve multiple layers or rolls to achieve useful area. The high voltages involved also can present a challenge for the circuitry used to efficienctly generate such voltages, and might present a hazard to the user upon any device failure.

Groups working with electroelastomers [9] are essentially using the dynamic capacitor properties of their material, and have reported promising results.

1.4.2 Piezoelectric Materials

Piezoelectric materials, such as quartz or PVDF, are well-structured crystalline solids which exhibit coupling between mechanical strain and surface charge. By coating these materials with conductive electrodes, as would be done to any dielectric in a capacitor, this surface charge can be accessed. In fact, harvesting energy from deformable piezoelectrics is very similar to the dynamic capacitor concept discussed above, although no explicit voltage polarization is needed ahead of time. Instead, poling is inherent to the material.

Piezoelectric approaches are common in the energy harvesting field because they have no "moving" parts (beyond the small deformations of the piezoelectric material itself). This makes them simple systems and relatively easy to fabricate and integrate. However, mechanically, they have high stiffness and therefore allow little work input for a given

applied force. Approaches such as membrane deflection reduce this stiffness and may allow more deflection, but are compromised because much of the strain energy is put into the thicker backing metal plate than into the piezoelectric film. Additionally, from the electrical side, piezoelectrics have high output impedance, looking mostly like a capacitor, which makes coupling power out difficult.

Another MIT project sought to use piezoelectrics in a novel fashion as part of a resonant hydraulic transducer [4]. This study involved using active valves to very rapidly control fluid flow into and out of a control volume, inside which a piezoelectric element would expand or contract against the nearly-incompressible fluid. In this fashion, the device could act as a pump or a turbine, converting pressure energy to electrical energy, which would be perfect for this kind of energy harvesting challenge. Ultimately, the model predicted tremendous power densities on the order of 1W/g for a microfabricated system, but the system was never built.

1.4.3 Microturbines

While turbomachinery is a part of our everyday lives, from gas turbine power plants to the compressor in our air conditioning system, small-scale fluid-power systems are still relatively rare. There are a number of reasons for this disparity. First, conventional fabrication processes dictate that gap dimensions won't scale nearly as quickly as overall dimensions, making leakage path losses more significant. Second, boundary-layer and viscous effects tend to become more prominent, which can complicate the analysis. Third, big amounts of power still require big devices. Still, newer machining processes (DRIE MEMS fabrication) and new successes are pushing on the design envelope, and the appli-

cations for smaller devices are becoming more apparent.

The most well known tiny turbomachinery project is the MIT Microengine Project, which attempted to build a gas turbine electrical generator using silicon fabrication processes, mostly Deep Reactive Ion Etching (DRIE) and anodic bonding of multiple silicon wafers. The overall dimensions were 21x21x3.7mm, and a goal of 10W was established. While using conventional IC processes allowed for excellent dimensional control in the x-y plane, the thickness dimension faced many tolerance challenges because of the variability of the etch processes. The nonuniformities in cuts through the thickness became a limiting issue particularly with the journal bearings, and was only managed after years of process tuning. Other issues included maintaining thermal isolation between regions of the heat engine, forming good bonds between wafers, start-up dynamics, and coupling the mechanical work to either magnetic or electric generation systems. Dozens of MIT faculty, staff, and students worked on the project for more than a decade, and the project is currently drawing to a close with lots of successful component demonstrations but no integrated system.

Because the footstep energy harvesting system only has flow work, and not added chemical (fuel) energy, the power per volumetric flow rate is significantly lower than for the MIT Microengine. This means that our operating point is not nearly as bleeding-edge as was the case for the case of the MIT Microengine, in terms of aggressive scaling, rotation rates, and the downstream effects of those parameters. Also, not being a heat engine, there are no thermal issues to battle.

There has been some interest in pumps at small scales, particularly in biological/chemical/medical equipment for moving small volumes around, however these designs have not

been suited to reversible operation as turbines. In particular, there is a class of micropumps that operate by controlling the pressure at various parts of a membrane in a binary fashion, and with channels and reservoirs fabricated appropriately on the opposite side of the membrane, these pumps can draw a fluid into a chamber, close the inlet valve, and then push on the fluid. However, this approach is not particularly power-friendly and is intended primarily for bench-top lab equipment.

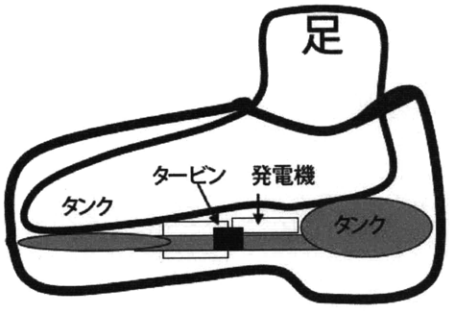

Fig.1 提案する歩行発電システ

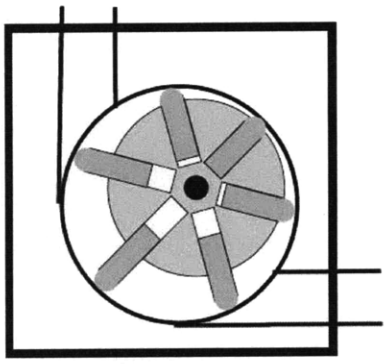

Fig.2 試作タービン

Figure 3. NTT vane-motor turbine figures, from [19]

As shown in Figure 3, the 2008 NTT shoe turbine work describes a similar system. The caption of the sub-figure on the left is roughly, "Walking generator with a turbine," showing labels for a leg, two water-filled bladders, a turbine, and a generator. For the sub-figure on the right, the caption is roughly "Vane-motor-type turbine." The turbine in this system was constructed with six spring-loaded vanes which create sealed and non-sealed volumes within the rotating turbine. These volumes occur between a rotor and stator with offset axes of rotation. The pressure difference directly pushes on the vanes, and spins a connected electromagnetic generator. The generator is external to the turbine, allowing them to use an off-the-shelf permanent magnet dynamo for this purpose, instead of attempting to tightly integrate the turbine and generator as was done in this thesis work. Although one would expect severe issues with keeping an incompressible

fluid inside a changing volume, first with compression until failure and second with cavitation upon expansion (producing tremendous forces that would both load the bearing and retard the motion of the rotor), the authors suggest that the performance is in fact quite good, reaching efficiencies of roughly 32% and generating 1.2 Watts while walking [19].

1.5 Thesis Contribution

Although the use of miniature turbines in energy harvesting applications has been proposed in the past, including a 2001 U.S. Patent proposing a similar in-shoe turbine and fluid rectification system [8] and a 2008 Japanese Patent proposing a in-shoe turbine integrated with a generator [18], this thesis project is one of the first known implementations of such a system. In fact, this is among the smallest working hydraulic turbine design to be found in the literature, at roughly the same scale as the parallel shoe turbine work done at NTT [19]. The only known previous project implementing a smaller turbine is the MIT Microengine, which spent more than a decade in development without producing a working prototype.

While the actual embedding of the system within the shoe and miniaturization of external package size is not within the scope of this thesis, the project is focused on demonstrating technologies that would translate directly to future integration, such as thin radial-flow turbines, and generator electromagnetics integrated directly with the rotor, instead of coupling to an external dynamo.

Despite these challenges, this thesis demonstrates one of the first working wearable-scale hydraulic turbines known in the academic literature, and lays the groundwork for future developments in the field, particularly toward manufacturing a compact and integrated design.

2 Design Overview

In order to overcome the various manufacturing and theoretical problems with other energy harvesting techniques described earlier, this project will focus on a novel design based around a small but conventionally-manufacturered rotating water turbine.

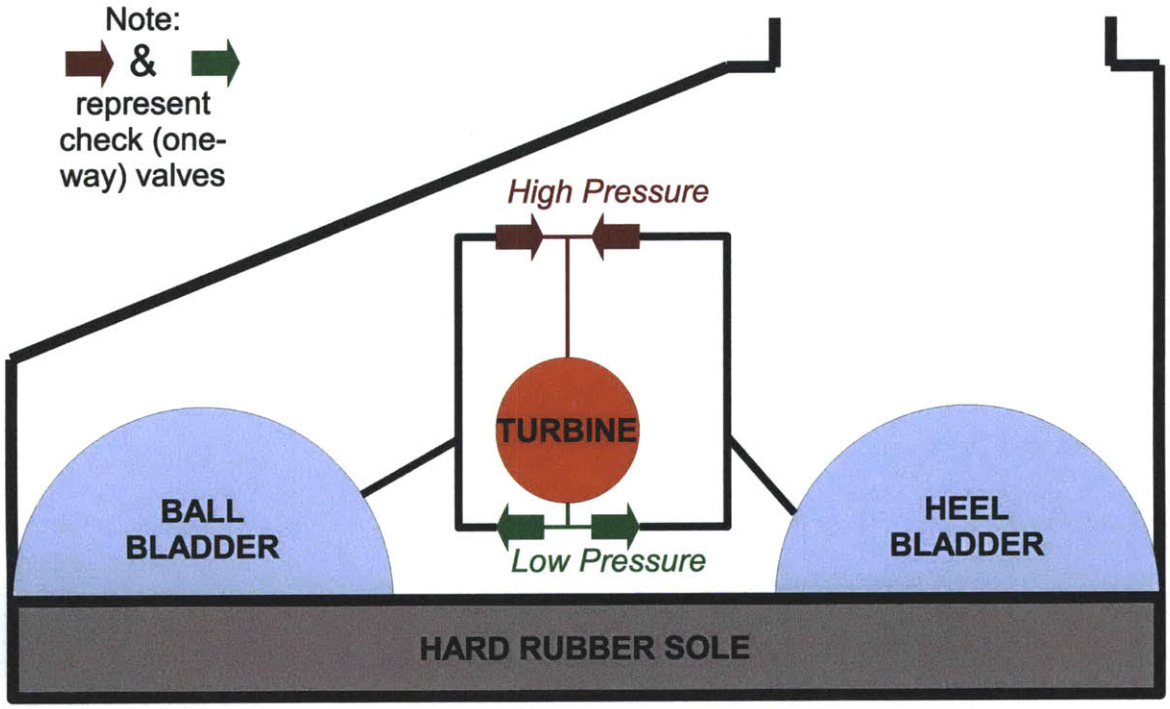

Figure 4. System conceptual sketch

As shown in the conceptual sketch in Figure 4, there are three major system components: deformable fluid bladders at the front and back of the shoe, check valves to ensure one-way fluid motion, and finally the turbine itself.

The system forces an incompressible liquid through two bladders, four check valves, and a turbine. The user, in the natural process of walking, alternates their weight between the back (heel) and front (ball) of the foot. To borrow from electrical engineering terminology, this alternating pressure differential is "rectified" by a "diode bridge" consisting of passive mechanical check valves.

A key efficiency feature of this design is that the turbine is allowed to rotate continuously in one direction, at the cost of the pressure drops through the check valves. In comparison, other designs in the literature generally have an element that is strained and unstrained each cycle. Again going back to electrical engineering analogies, the importance of impedance matching across a wide range of frequencies is greatly reduced by the diode bridge.

The turbine is connected to an electromagnetic generator. Another novel feature of this implementation is that the generator is itself integrated within the turbine, leading toward further miniaturization and eliminating a rotating fluid seal.

2.1 Force-Displacement Plane

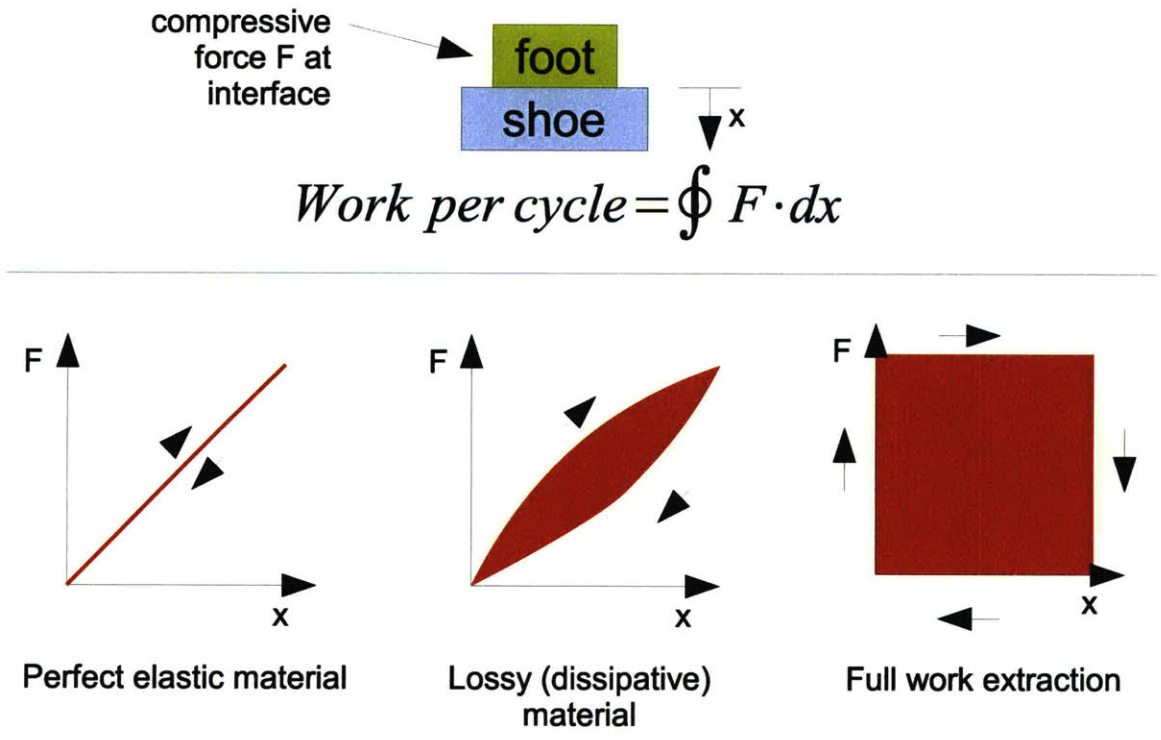

Figure 5. Force-displacement plane

In order to create a simple model of the interaction between shoe and foot, and to examine the possibilities for extracting energy, consider Figure 5. Since the foot and shoe surface are not attached, only a compressive force can exist at the interface. For the same reason, the displacement from equilibrium can only be in the $+x$ direction as labeled.

While applying a load to a part of the shoe, the force and displacement both increase from the origin. During unloading, the force might be equal to or less than it was at the same displacement during the loading process. That is, while loading the shoe, the person puts energy into the material. However, it is not necessarily the case that the same amount of energy is returned to the person as they remove that load. The area in this cycle (red) is the amount of work that is potentially extractable by the shoe.

The maximum force is set by the user's weight. The maximum displacement is set by some comfortable displacement, where we might assume 3mm or so. Therefore, to maximize the work extraction, we have to maximize the area of our loop between (0, 0) and (3mm, $m * g$). This is only possible with the rectangular loop shown in the right-most subgraph in Figure 5. The interface force jumps immediately to its full value F, and only then does the interface move through a distance x. As unloading begins, F drops to zero, so no work is done back on the foot. Therefore, a full work product $F \cdot x$ is done and might be recovered by our system.

Even if this proves to not be a comfortable way to walk, it is possible to add a "springy" elastic material on top of our system, which would adjust the right-hand graph to look more like the middle one by adding a elastically-returned displacement in series with the non-returned displacement.

The system design proposed here provides a force-displacement profile exactly like the right-hand graph of Figure 5, the full rectangle. This is because the user's full weight is

applied essentially instantly (thanks to the incompressible turbine working fluid), and continues until the entire bladder is discharged through the turbine. At that point, the bladder exerts no force back on the foot, because of the check valve arrangement. Therefore, in contrast to all of the other prior work mentioned except [6], the force-displacement plane is maximally utilized for energy capture (for a given user weight and permissible displacement).

2.2 Thermodynamics

Ultimately, the turbine is going to be constrained by the First Law of Thermodynamics for a control volume:

$$\frac{\mathrm{dE}}{\mathrm{dt}} = \dot{Q}_{\text{in}} - \dot{W}_{\text{shaft}} + \sum_{\text{inputs}} \dot{m}(h + gz + \frac{\alpha \bar{v}^2}{2}) - \sum_{\text{outputs}} \dot{m}(h + gz + \frac{\alpha \bar{v}^2}{2}) \tag{7}$$

where E is energy stored in the control volume (including the flywheel energy stored in the rotating turbine), $\dot{Q}$ is heat flow power in, $\dot{W}_{\text{shaft}}$ is shaft power out (includin the generator plus bearing friction), h is specific enthalpy, gz is gravitational potential energy per unit mass, $\alpha = 1$ for turbulent and $\alpha = 2$ laminar flow, and $\bar{v}^2$ is the square of the average flow velocity.

For the moment, we will assume steady state operation, no heat transfer, no frictional shaft work, negligible effects due to gravity, and neglibible effects due to inlet and outlet kinetic energy. The equation then simplifies to:

$$\dot{W}_{\text{shaft}} = \dot{m}(h_{\text{in}} - h_{\text{out}}) \tag{8}$$

The Second Law of Thermodynamics for the control volume must also be brought to bear:

$$\frac{dS}{dt} = \dot{S}_{\text{gen}} + \sum \frac{\dot{Q}_{\text{in}}}{T} + \sum_{\text{inputs}} \dot{m}s - \sum_{\text{outputs}} \dot{m}s \tag{9}$$

where S is the total entropy inside the control volume, $\dot{S}_{\text{gen}}$ is the entropy generation rate (representing losses), $\dot{Q}_{\text{in}}$ are any heat transfers into or out of the device, and s is the specific enthalpy of a flow. Again assuming steady state operation, minimum losses, and thermal equilibrium (no heat transfer), this simplifies to:

$$s_{\text{out}} = s_{\text{in}} \tag{10}$$

The constraint in Equation 10 says that the entropy per unit mass of the inlet and outlet flows must be essentially identical.

2.3 Selection of Turbine Working Fluid

Given Equation 8, we can now recall the constitutive relationships for both incompressible fluids and for ideal gases to compare their behavior in our system.

	Incompressible Fluid	**Ideal Gas**
Specific Energy, u	cT	$c_v T$
Specific Enthalpy, $h = u + \frac{P}{\rho}$	$cT + \frac{P}{\rho}$	$c_p T$
Specific Entropy, s	$c\ln(T)$	$c_p \ln(T) - R\ln(P)$

Table 2. Constitutive relations for incompressible fluid and ideal gas

While at first it may appear that there is great similarity between the incompressible fluid and ideal gas models since we've so far needed only to consider the enthalpy of the flows, the entropy relationship described in Equation 10 also applies, and says that the specific entropy at inlet and outlet must be identical.

This is where significant differences between the incompressible fluid and ideal gas model take shape. For an incompressible fluid, Equation 10 implies $T_{\text{in}} = T_{\text{out}}$. However, for an ideal gas, it instead implies $c_p \ln(\frac{T_{\text{in}}}{T_{\text{out}}}) = R\ln(\frac{P_{\text{in}}}{P_{\text{out}}})$. Since we know we will have a pressure as our driving force, if we use an ideal gas, a pressure ratio will lead to a temperature

ratio as well! This will cause all sorts of undesired issues with thermal management and losses.

In general, unless one is trying to extract energy from a temperature difference, it is best to avoid an ideal gas as a working fluid because of the unavoidable coupling between mechanical (pressure) and thermal domains.

Additionally, with the force-displacement diagram presented in Figure 5, it must be noted that an ideal gas will only be at finite pressure after some displacement x, which will not allow the full rectangle of energy extraction to occur. In contrast, with an incompressible fluid, only an infinitesimal displacement x is needed for pressurization by definition.

Therefore, we select an incompressible fluid as our turbine working fluid, and can substitute to reveal:

$$\dot{W}_{\text{shaft}} = \dot{m}\frac{P_{\text{in}} - P_{\text{out}}}{\rho} = \dot{V}(P_{\text{in}} - P_{\text{out}}) = \dot{V} \cdot \Delta P \tag{11}$$

where $\dot{V}$ is the volumetric flow rate (in m^3/s) and ΔP is the pressure difference across the turbine (in Pa).

Equation 11 shows that the maximum extractable power is related directly to the volume flow rate and to the pressure across the turbine. However, we will not be able to achieve this amount of power in practice because we will leave kinetic energy in the outlet flow, and because of various system losses.

2.4 Angular Momentum Conservation

This turbine, as well as all rotating turbomachinery in general, is able to generate a torque because of the law of conservation of angular momentum around the axis of the machine. The angular momentum of a particle with mass m at location $\bar{r}$ from the axis

and traveling with velocity vector $\bar{v}$ is $\bar{h} = m(\bar{r} \times \bar{v})$. The total torque applied to the system equals the time rate of change of the angular momentum of the enclosed particles. For an inertial control volume:

$$\frac{d\bar{H}}{dt} = \sum \bar{T} + \sum_{\text{inputs}} \dot{m}(\bar{r} \times \bar{v}) - \sum_{\text{outputs}} \dot{m}(\bar{r} \times \bar{v}) \tag{12}$$

which is rearranged from eqn 3.56 in [21], where $\bar{H}$ is the total angular momentum inside the control volume (including both fluid and the rotor itself), $\bar{T}$ is any external torque on the control volume (again including both fluid and the rotor itself), and $\dot{m}$ is a mass flow rate. From the presence of vector cross products, it is clear that only velocities that are tangential to the rotor can produce any torque.

In the steady state for a turbine which has a single flow in and out, this equation simplifies to:

$$\bar{T}_{\text{total}} = \dot{m}[(\bar{r} \times \bar{v})_{\text{out}} - (\bar{r} \times \bar{v})_{\text{in}}] \tag{13}$$

where $\bar{T}_{\text{total}}$ is the sum of all torques on the control volume, including electromagnetic torques from the generator, plus frictional torques from external fluid and bearing surfaces.

There are a few considerations to keep in mind when applying Equation 13.

First, the velocities $\bar{v}$ are relative to the inertial frame. This is important because the rotation of a rotor itself needs to be accounted for relative to the fluid: $\bar{v} = \bar{v}_{\text{rel}} + \bar{\omega} \times \bar{r}$, where $\bar{v}_{\text{rel}}$ is the fluid's velocity relative to the rotating frame of the spinning rotor.

Second, velocity actually appears as a squared term in the torque equation for a given design, because $\dot{m} = \rho A v$ for constant cross-sectional area flow with mass density ρ. This highlights the importance of high tangential velocities within the turbine.

Third, the torque contribution appears to be maximized when the $\bar{r} \times \bar{v}$ are maximized, such that the velocity is purely tangential.

Fourth, conservation of energy will imply particular maximum absolute velocities in the turbine. For an incompressible fluid, a pressure P represents a volumetric potential energy density. If the fluid is initially at rest and that energy is converted losslessly to kinetic energy, it becomes $\frac{1}{2}\rho v^2$, a volumetric kinetic energy density. This sets an essential constraint on the magnitude of fluid velocity that can be obtained solely from a driving pressure of $|\bar{v}| \leqslant \sqrt{\frac{2P}{\rho}}$. Note that combustion-based gas turbines do not necessarily need to obey this rule, both because of compressibility of the working fluid, and more importantly because a significant amount of additional energy is added via the chemical reaction of combustion.

Finally, various rotor designs yield different constraints on the $\bar{r}$, $\bar{v}$ components in Equation 13, and these will be discussed later in more detail.

2.5 Viscous Flow Losses

A common analogy for the viscosity of a fluid is its "stickiness" – its resistance to flowing over itself or any boundary. At the microscale level, this model imposes the no-slip boundary condition, which forces the infinitesimally thin fluid layer directly in contact with the wall to have the same velocity as the wall itself. In an enclosed static pipe, this means that the fluid at the wall must be stationary, and any bulk velocity must occur because of some velocity profile that evolves over the cross-section of the pipe.

Additionally, there are two primary regimes of fluid flow: laminar flow, and turbulent flow. These arise because of competing momentum and viscous effects, where momentum effects tend to suggest the primacy of intra-fluid interactions, and viscous effects suggest

the primacy of interactions with the boundary elements of the flow. For a fluid of viscosity μ with density ρ traveling at mean velocity $\bar{v}$ through a channel with hydraulic diameter D_h, the Reynolds number

$$Re = \frac{\rho \bar{v} D_h}{\mu} \tag{14}$$

is typically large ($\gg$ 2300) for turbulent flows where momentum dominates (high momentum per unit volume $\rho\bar{v}$), and is typically small ($\ll$ 2300) for laminar flows where the viscous interactions with boundaries dominate (high viscosity μ and low distance to walls D_h).

For a circular duct, like a round tube, the hydraulic diameter D_h is equal to the actual diameter of the tube. But for other flow geometries:

$$D_h = \frac{4A}{P} \tag{15}$$

where A is the flow area, and P is the wetted perimeter of the duct. For a rectangular channel with dimensions W by H, the hydraulic diameter is $D_h = \frac{4WH}{2(W+H)}$, and for a square channel, $D_h = \frac{4W^2}{2(W+W)} = W$.

For flow in any enclosed duct, the force between the walls and the moving fluid can be simplified to a friction factor f, where the total pressure drop through the channel of length L is:

$$\Delta P = f \frac{L}{D_h} \left(\frac{1}{2} \rho \bar{v}^2 \right) \tag{16}$$

For laminar flow in a smooth duct, the friction factor can be calculated analytically, and it can be shown that $f = \frac{64}{\mathrm{Re}}$. For turbulent flow in a smooth duct, the friction factor must be determined analytically, and a correlation of $f = (0.790 * \ln(\mathrm{Re}) - 1.64)^{-2}$ holds over a wide pressure range [2].

For a variety of flow rates, for water where $\rho \approx 1000\,[\mathrm{kg}/m^3]$ and $\mu \approx 8.538 \times 10^{-4}\,[\mathrm{Pa}\,s]$,we can summarize these results against various tube/pipe sizes:

D_h (inches)	1 mL/s	5mL/s	10mL/s	15mL/s	20mL/s	30mL/s
0.032" (=1/32")	0.876357	20.605867	68.365090	138.933275	230.476595	472.213419
0.039" (=1mm)	0.347869	6.938312	22.881434	46.359056	76.753124	156.852957
0.063" (=1/16")	0.054772	0.791484	2.575733	5.183918	8.545636	17.366659
0.078" (=5/64")	0.022435	0.278498	0.899911	1.804778	2.968388	6.014759
0.079" (=2mm)	0.021742	0.268471	0.867289	1.739131	2.860179	5.794882
0.094" (=3/32")	0.010819	0.118859	0.381707	0.763180	1.252767	2.532040
0.118" (=3mm)	0.004295	0.040523	0.129056	0.256975	0.420715	0.847461
0.125" (=1/8")	0.003423	0.031132	0.098936	0.196791	0.321967	0.647990
0.156" (=5/32")	0.001402	0.007011	0.034812	0.068946	0.112489	0.225597
0.188" (=3/16")	0.000676	0.003381	0.014857	0.029314	0.047713	0.095398
0.219" (=7/32")	0.000365	0.001825	0.007243	0.014243	0.023133	0.046126
0.250" (=1/4")	0.000214	0.001070	0.003892	0.007629	0.012367	0.024599
0.281" (=9/32")	0.000134	0.000668	0.001336	0.004402	0.007123	0.014137
0.313" (=5/16")	0.000088	0.000438	0.000876	0.002694	0.004352	0.008618
0.344" (=11/32")	0.000060	0.000299	0.000599	0.001728	0.002788	0.005510
0.375" (=3/8")	0.000042	0.000211	0.000423	0.001153	0.001857	0.003664

All pressure drop entries are in kPa/cm. Laminar flow entries higlighted in yellow.

Table 3. Viscous flow loss calculations

Considering that the total pressure differential in this system will be on the order of 100kPa, and that components will be spread over centimeters of distance, it is important to keep track of the losses in Table 3 to ensure that viscous plumbing losses are kept to a minimum.

2.6 Other Plumbing Losses

Besides the losses due to viscosity, other elements of the plumbing will cause pressure drop losses. In general, these losses are proportional to the flow energy per unit volume, and can therefore be written as a pressure drop:

$$\Delta P = K\left(\frac{1}{2}\rho \bar{v}^2\right) \tag{17}$$

Different plumbing features like turns, valves, expansions, and contractions will have different constants K typically of order 0.1 to 10, which are tabulated experimentally. Being proportional to the flow energy per unit volume, it is be useful to calculate this for a variety of flow rates and diameters:

D_h (inches)	1 mL/s	5mL/s	10mL/s	15mL/s	20mL/s	30mL/s
0.032" (=1/32")	2.042	51.050	204.200	459.450	816.799	1837.798
0.039" (=1mm)	0.811	20.264	81.057	182.378	324.228	729.513
0.063" (=1/16")	0.128	3.191	12.762	28.716	51.050	114.862
0.078" (=5/64")	0.052	1.307	5.228	11.762	20.910	47.048
0.079" (=2mm)	0.051	1.267	5.066	11.399	20.264	45.595
0.094" (=3/32")	0.025	0.630	2.521	5.672	10.084	22.689
0.118" (=3mm)	0.010	0.250	1.001	2.252	4.003	9.006
0.125" (=1/8")	0.008	0.199	0.798	1.795	3.191	7.179
0.156" (=5/32")	0.003	0.082	0.327	0.735	1.307	2.940
0.188" (=3/16")	0.002	0.039	0.158	0.355	0.630	1.418
0.219" (=7/32")	0.001	0.021	0.085	0.191	0.340	0.765
0.250" (=1/4")	< 0.001	0.012	0.050	0.112	0.199	0.449
0.281" (=9/32")	< 0.001	0.008	0.031	0.070	0.124	0.280
0.313" (=5/16")	< 0.001	0.005	0.020	0.046	0.082	0.184
0.344" (=11/32")	< 0.001	0.003	0.014	0.031	0.056	0.126
0.375" (=3/8")	< 0.001	0.002	0.010	0.022	0.039	0.089

All pressure entries are in kPa.

Table 4. Flow energy per unit volume

Table shows the value of $\frac{1}{2}\rho\bar{v}^2$ which goes into Equation 17 for a particular diameter and flow rate. Some useful values K that combine with Table 4 and Equation 17 are:

Description of Obstacle	Typical K Value(s)
Sharp entrance	0.5
Sharp re-entrant entrance	1.0
Abrupt enlargement	$(1 - A_1/A_2)^2$ with respect to A_1, v_1
Abrupt contraction	$\approx 0.5(1 - A_2/A_1)$ with respect to A_2, v_2
90 degree elbow	0.65 to 1.5
Tee – line flow	~ 0.9
Tee – branch flow	~ 2.4

Table 5. Typical K flow loss values

The values in Table 5 are tabulated from [2] and [21].

3 Turbine Rotor Design

This chapter explores the design of the rotor, which is the active part of the turbine, including both modeling and manufacturing considerations.

3.1 Types of Turbines

In general, there are several classification categories of hydroelectric turbines.

The first classification generally identifies a device as either a impulse or reaction device. This distinction is used to indicate where in the system pressure energy is converted to kinetic energy. If a garden hose is sprayed into a rotating set of buckets free in air, the pressure drop is entirely in the nozzle, and the buckets are set in motion only by the impulse (momentum change) of the water – this is an impulse turbine. However, a reaction turbine depends on pressure changes within the fluid to convey a force. Ultimately, the same conservation laws apply to both types of devices, but for historical purposes, it should be noted that any closed and submerged system like the one described in this thesis is considered a reaction turbine, because the pressure changes happen at the same time and place that work is delivered to the device [20].

The second classification typically refers to the orientation of the flow within the device, whether axial or radial, and if radial, whether inward or outward flowing. In an axial device, like a windmill or an aircraft turbine, the flow through the device is primarily oriented along the axis of rotation. Radial turbines instead feature flow primarily perpendicular to the axis of rotation. However, even in radial turbines, geometry requires that either the inlet or outlet be at least somewhat out-of-plane in the axial direction to allow for fluid to be conveyed to or from the active radial area.

For this thesis, a radial outflow turbine was selected because it allows for a maximally flat overall system design and also makes manufacturing of the device significantly simpler. In contrast to axial systems like windmills or jet engines, which require complex twisting geometries that may not be parallel or perpendicular to any axis of the machine, radial turbomachines often have features that are primarily two-dimensional in nature. This is because in radial machines, the tangential velocity of the rotor itself $\overline{\omega} \times \overline{r}$ and the flow velocity are all entirely in one plane that is perpendicular to the axis of rotation.

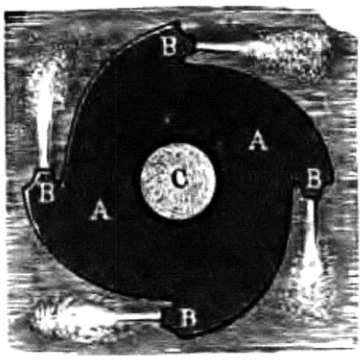

Figure 6. Reaction wheel turbine, from [20]

The device shown in Figure 6 is a device very similar to that which will be constructed in this thesis. The original text next to the figure states, "The efficiency of such a wheel, exceedingly simple as it is, may easily be made as high as $\frac{2}{3}$" [20].

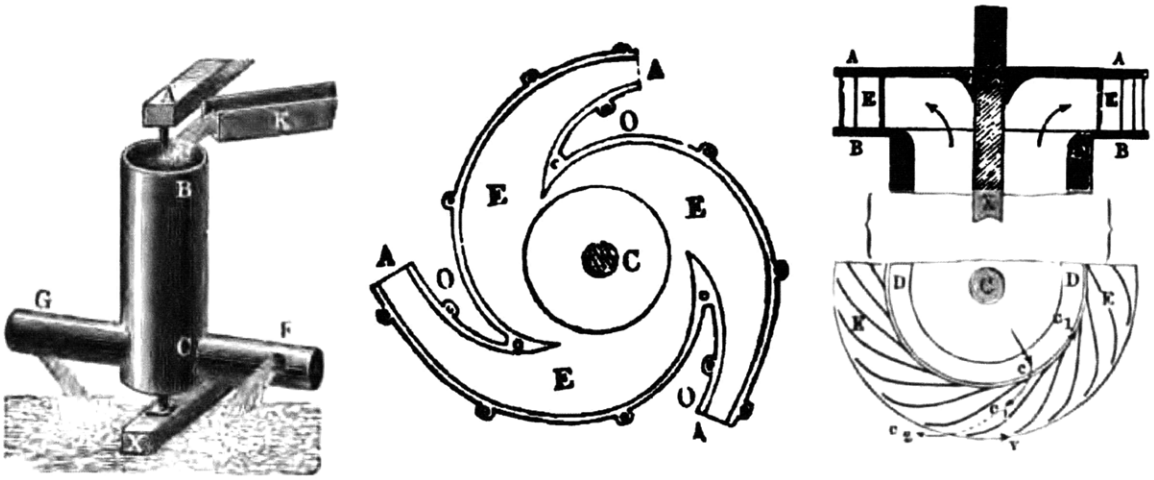

Figure 7. Two-arm reaction wheel, Whitelaw/Scottish turbine, and Combes wheel, from [20]

The simplest such device is highlighted on the left of Figure 7, and other implementations are shown as well. The Whitelaw/Scottish turbine, in the center of Figure 7, uses curved arms, while the Combes reaction wheel on the right shows a multitude of curved vanes. But in all cases, the concept is the same: fluid enters axially, travels radially outward, and is turned to exit tangentially, or substantially tangentially in the case of the Combes device.

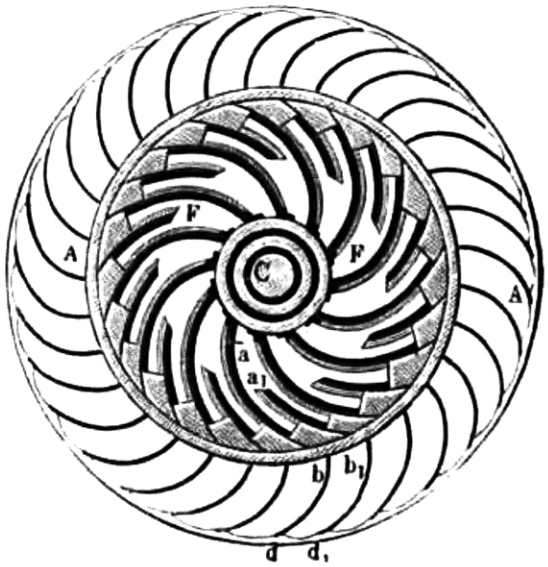

Figure 8. Fourneyron Turbine, from [20]

This is in contrast to other turbine designs, like the Fourneyron Turbine shown in Figure 8, which also has static guide vanes (labeled F in the diagram) that impart a tangential velocity to the fluid before entering the rotor. In the reaction wheels shown in Figure 7, the fluid goes from zero to large tangential velocity while passing through the rotor. In contrast, in the Fourneyron Turbine, the fluid enters the rotor with large tangential velocity, and ideally leaves with zero. This leaves much less kinetic energy remaining in the outlet flow, allowing for more to be extracted as work by the turbine.

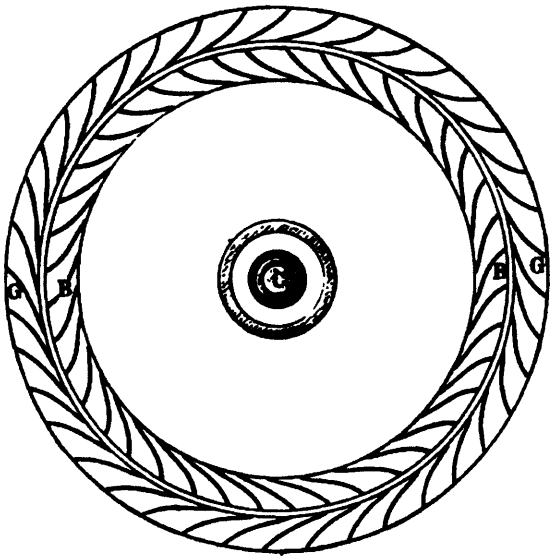

Figure 9. Francis Turbine, from [20]

The Fourneyron Turbine presents a manufacturing challenge because fixed stator vanes must be placed inside a pressurized, rotating rotor. However, the Francis Turbine as shown in Figure 9 is a similar design but with the stator vanes outside the rotor, and therefore also with fluid flow reversed and now flowing radially inward. This provides the same advantages regarding less kinetic energy remaining in the outlet flow, but is generally easier to manufacture.

In any case, because manufacturability is a primary concern of this project, the reaction wheel turbine as shown in Figure 6 was selected as the model for this thesis project. While Figure 6 shows four outlet nozzles, this project will use two, which is the minimum needed for the thrust forces to cancel and produce only a net moment, and not a radial load on the bearing. Additionally, this design will try to maintain a cylindrically-symmetric profile in an attempt to reduce drag from the "arms" being dragged through the submerged outlet area.

3.2 Sizing of Turbine Outlet Nozzles

For an incompressible fluid flowing through any port at average velocity $\overline{v}$, a volumetric flow rate of $\dot{V} = A\overline{v}$ or a mass flow rate of $\dot{m} = \rho A\overline{v}$ is obtained. But as discussed earlier, a driving pressure difference ΔP across a nozzle results in a maximum velocity of $\sqrt{2\frac{\Delta P}{\rho}}$. For water and pressures in the range of 15-30 psi (103-207 kPa), this represents a velocity range of approximately 14 to 20 m/s.

While it may appear from Equation 13 that more torque will be generated for higher mass flow, this discounts the significant effect that higher mass flow rates will cause higher losses in all parts of the system, like those losses described in Tables 4 and 5. These losses will cause pressure drops of their own, which will reduce the pressure difference across the nozzle and therefore the velocity.

In fact, since we are not interested in the instantaneous power generation but really the total amount of energy extracted over an entire step, the flow rate should be selected to be essentially as low as possible while still allowing the entire desired volume of fluid to be moved in each heel and ball strike. Although the instantaneous $\dot{m}$ in Equation 13 will decrease, the velocities will be higher because of reduced losses, and therefore the total time-integrated angular momentum change and extractable generator energy will be increased.

While several nozzle geometries were considered, eventually a 0.040" square channel was selected for each of the two nozzles. This has a total area of $2.06 \times 10^{-6} m^2$, and therefore at the driving pressures 15-30psi (103-207 kPa), allows for maximum volumetric flow rates of 30 to 42 mL/s. Because the expected time that a user's weight is on either the heel or

ball bladder is roughly at most $\frac{1}{4}$ their total walk period, at a brisk 1 Hz walk, this allows for a maximum of roughly 7.5 to 10.5 mL of fluid total to traverse the system.

3.3 Torque and Power Model

To develop a model for the torque and output power of this type of turbine, angular momentum and energy conservation laws are applied.

First, because the fluid enters the rotor axially and leaves purely tangentially, Equation 13 can be simplified to:

$$T_{\text{generator}} + T_{\text{losses}} = T_{\text{total}} = \dot{m} r v \tag{18}$$

where v is the inertial frame exit velocity of the fluid. A torque at a particular speed causes a work flow rate:

$$\dot{W}_{\text{shaft}} = T_{\text{total}} \omega \tag{19}$$

and from energy conservation in Equation 7, this power is equal to the difference between the energy in the inlet and outlet flows.

As described previously, for a pressure drop across any nozzle, the fluid velocity relative to the nozzle is:

$$v_{\text{rel}} = \sqrt{\frac{2\Delta P}{\rho}} \tag{20}$$

However, in the inertial frame, the true velocity of the fluid must also account for the rotation of the rotor itself:

$$v = v_{\text{rel}} - \omega r = \sqrt{\frac{2\Delta P}{\rho}} - \omega r \tag{21}$$

The torque can then be written as a function of ω and ΔP:

$$T_{\text{total}} = \dot{m} r v = \rho A v_{\text{rel}} r (v_{\text{rel}} - \omega r) \tag{22}$$

and the extracted power is then:

$$\dot{W}_{\text{shaft}} = \rho A v_{\text{rel}} r (v_{\text{rel}} - \omega r) \omega \tag{23}$$

The input power is always $\dot{W}_{\text{in}} = \dot{m} \frac{\Delta P}{\rho} = A v_{\text{rel}} \Delta P$.

If all shaft work is extractable in the generator, which means that none is due to overcoming frictional or other losses, then the efficiency can be written:

$$\eta = \frac{\dot{W}_{\text{shaft}}}{\dot{W}_{\text{in}}} = \frac{\rho}{\Delta P} \left(\sqrt{\frac{2\Delta P}{\rho}} - \omega r \right) \omega r \tag{24}$$

or after reorganizing,

$$\eta = 2 \left(\frac{\omega r}{\sqrt{\frac{2\Delta P}{\rho}}} \right) \left[1 - \left(\frac{\omega r}{\sqrt{\frac{2\Delta P}{\rho}}} \right) \right] \tag{25}$$

This function reaches a maximum efficiency of 50% when $\omega r = \frac{1}{2} \sqrt{\frac{2\Delta P}{\rho}}$, and is back to zero at the no-load operating point of $\omega r = \sqrt{\frac{2\Delta P}{\rho}}$. This demonstrates clearly the penalty to using this type of turbine design without guide vanes, where a significant amount of energy is left in the outlet stream. For some sample numbers, with $\Delta P = 138\,\text{kPa}$ (20 psi) and $r = 0.5''$, the no-load speed is 1308 rad/s, or 12490 rpm, and the peak efficiency (and power) occurs at half that speed, or 6245 rpm.

A slightly more complicated version of this model can be found in some places in the literature (such as [20]) that also takes into account the pressure rise from the center axis to the outside of a rotating fluid volume, and adds this pressure to the externally-applied ΔP. However, since this is for an adverse pressure gradient (flow in a direction of increasing pressure) and since no structures will be provided to actually ensure such rotation occurs uniformly within the rotor, this extra pressure is not considered in this model.

3.4 Torque and Power Model with Losses

While the earlier efficiency calculations assumed that all fluid-developed torque was opposed only by electromagnetic generator torque, in reality there are frictional torques as well that must be accounted for as well. (Note that these are separate from and in addition to the pressure-drop losses that occur due to various plumbing features, as described earlier.)

The loss model will consist of two types of losses: those where the torque is proportional to the rotor speed, and those where the torque is proportional to the square of the rotor speed. Eddy current losses are an example of a loss source where the torque is proportional to the speed. Viscous drag losses are an example of a loss source where the torque is proportional to the square of the speed. The model is then:

$$T_{\text{total}} = T_{\text{generator}} + T_{\text{losses}} \tag{26}$$

$$T_{\text{losses}} = B \cdot \omega + C \cdot \omega^2 \tag{27}$$

Because loss torques are present regardless of whether any power is being extracted from the generator or not, this shifts the measured no-load speed down.

The output shaft work is then $T_{\text{generator}}\omega$, or

$$\dot{W}_{\text{out}} = \omega T_{\text{generator}} = \omega(T_{\text{total}} - T_{\text{losses}}) = \omega\big(\rho A v_{\text{rel}} r(v_{\text{rel}} - \omega r) - (B \cdot \omega + C \cdot \omega^2)\big) \tag{28}$$

so the efficiency is now

$$\eta_{\text{with losses}} = \frac{\dot{W}_{\text{out}}}{\dot{W}_{\text{in}}} = \frac{\omega\big(\rho A v_{\text{rel}} r(v_{\text{rel}} - \omega r) - (B \cdot \omega + C \cdot \omega^2)\big)}{A v_{\text{rel}} \Delta P} \tag{29}$$

Clearly, the maximum efficiency level (and the ω for which it occurs) will be lower than in the case with losses. The fit of these B, C loss parameters will be explored in the Results chapter of this document.

3.5 Flywheel Energy Storage Mode

While the preceding analysis has been concerned with the steady state operation of the turbine, it is also important to separately consider the dynamics of the system. The primary energy storage mode of the turbine is the rotational kinetic energy of the spinning rotor.

The energy stored in a rotating object is equal to

$$E_{\text{fw}} = \frac{1}{2} I \omega^2 \tag{30}$$

and for a uniform disc, the moment of inertia

$$I = \frac{1}{2} m r^2 = \frac{1}{2} \rho_m \pi r^4 t \tag{31}$$

Using the design values from the drawings in the appendix, there are three primary disc regions: one on the rotor top piece, one on the rotor bottom piece, and one consisting of the magnet holder and magnets. The steel has a thickness of approximately 0.137", while the two aluminum sections have a total thickness of about 0.143", and all have a diameter of 1.200".

The total moment of inertia is then approximately $3.13 \times 10^{-6}\,\text{kg} \cdot m^2$. At a rotor speed of 1500 rpm, this represents 38.6 mJ of stored energy, while at 5000 rpm, it represents 429 mJ.

In any case, depending on the operating speed of the turbine, the flywheel stores on the order of 10^{-1} to 10^{0} seconds worth of output power. (Note that this is output power, and ideally would also include power drained to system losses.) This quantity should ideally be higher to keep the system operating near its peak efficiency point for a longer fraction of the step period.

3.6 Manufacturing Considerations

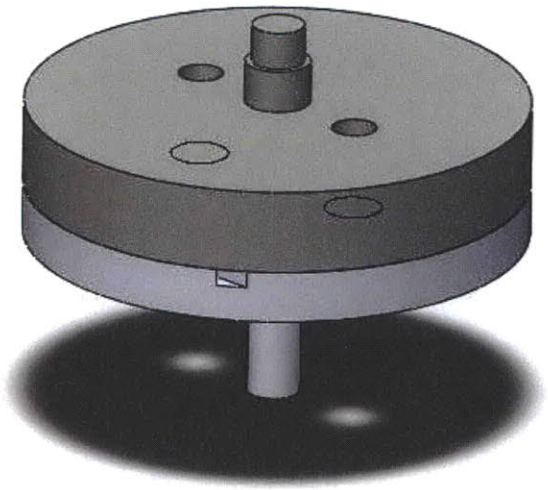

Figure 10. Rotor assembly: collapsed view

As shown in Figure 10, the rotor is built in two parts. This is to allow for the construction of internal geometry for flow channels.

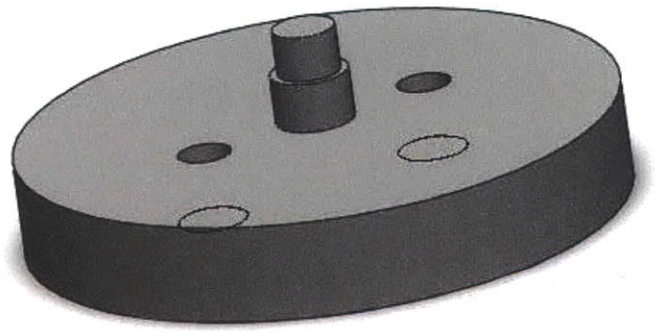

Figure 11. Rotor top piece: top view

The top part of the rotor has two threaded #6-32 holes that facilitate the joining of the two halves of the rotor. Additionally, it has two sections which are turned down to small diameters.

First, closest to the body of the piece, there is a section that is turned down to allow the magnet holder to mount and center itself. This magnet holder will be discussed later.

The second turned section is to fit within the ball bearing that allows for free rotation of the rotor.

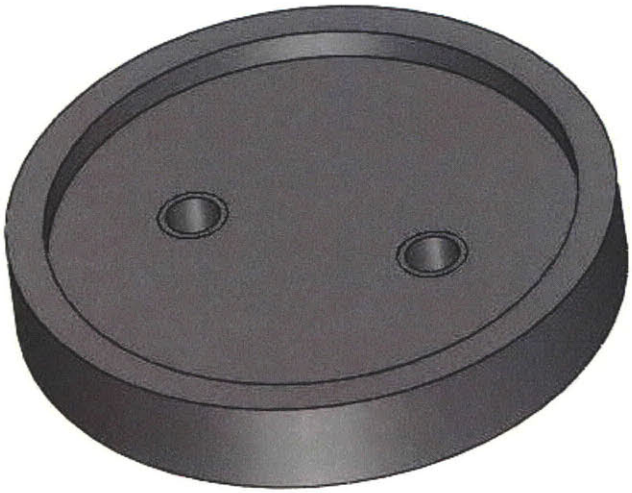

Figure 12. Rotor top piece: bottom view

On the internal side of the rotor top piece, as shown in Figure 12, there is simply a cavity which provides a space for fluid to flow radially outwards.

The rotor top piece is constructed of steel, both because of increased flywheel inertia, and because of its role in the magnetic flux path of the generator.

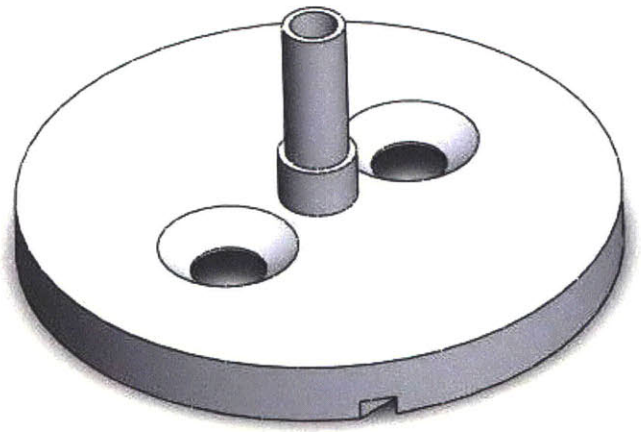

Figure 13. Rotor bottom piece: bottom view

The rotor bottom piece is constructed of aluminum simply because it is easier to work with in the machine shop. As shown from the external side in Figure 13, there are two countersinked holes that hold the #6-32 screws that will hold the two rotor pieces together.

There is also an axial flow path for fluid to enter the rotor. This is made using a 3/32" (0.094") diameter drill bit. The outer diameter of this inlet section is 0.125" to accomodate the plain bearing used to support the rotor, as discussed later, which means that the remaining wall thickness here is approximately 0.016". This is quite thin and requires special attention during machining so as not to inadvertently deform it during handling.

There is also a section near the body of the rotor bottom piece that is turned to a slightly larger diameter. This is to provide a hard stop against which the rotor can not pass through the plain bearing, but in practice this is not used because the rotor is magnetically attracted to the top plate.

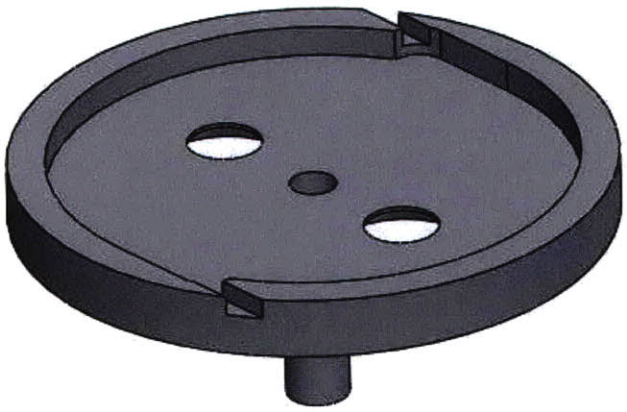

Figure 14. Rotor bottom piece: top view

From Figure 14, one can see that the interior of the rotor bottom piece is very similar to that of the rotor top piece: it is largely a cylindrical void that is used for radial fluid flow.

However, this piece also contains the turbine outlet nozzles, which controls the area and direction of the flow exiting from the rotor.

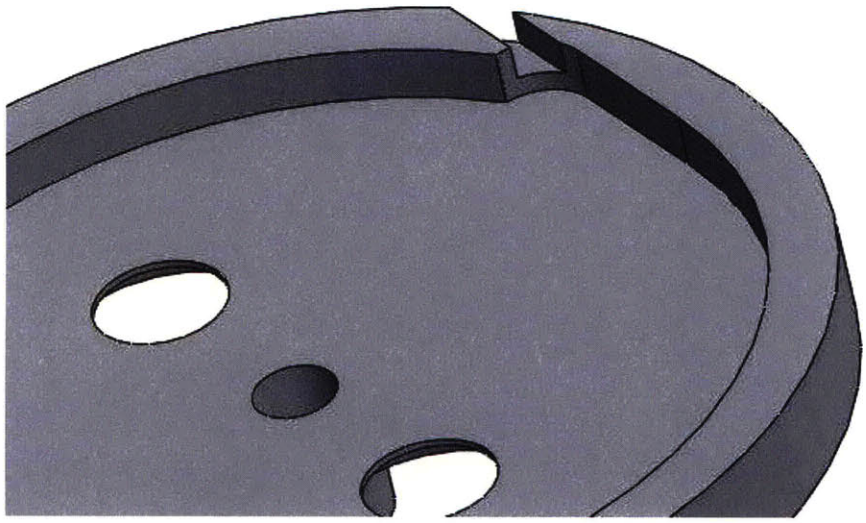

Figure 15. Rotor bottom half: channel closeup

The close-up view shown in Figure 15 highlights the relative sizing of the 0.040" square channel to the rest of the rotor. While the majority of the rest of the rotor is machined on a lathe, the channels are cut on a milling machine, using a miniature end mill at high cutting speed. The length of the square channel is approximately 2 to 3 times its dimension, which is known to provide a reasonable tradeoff between accurately directing the

flow and frictional losses to the walls of the rotor [21].

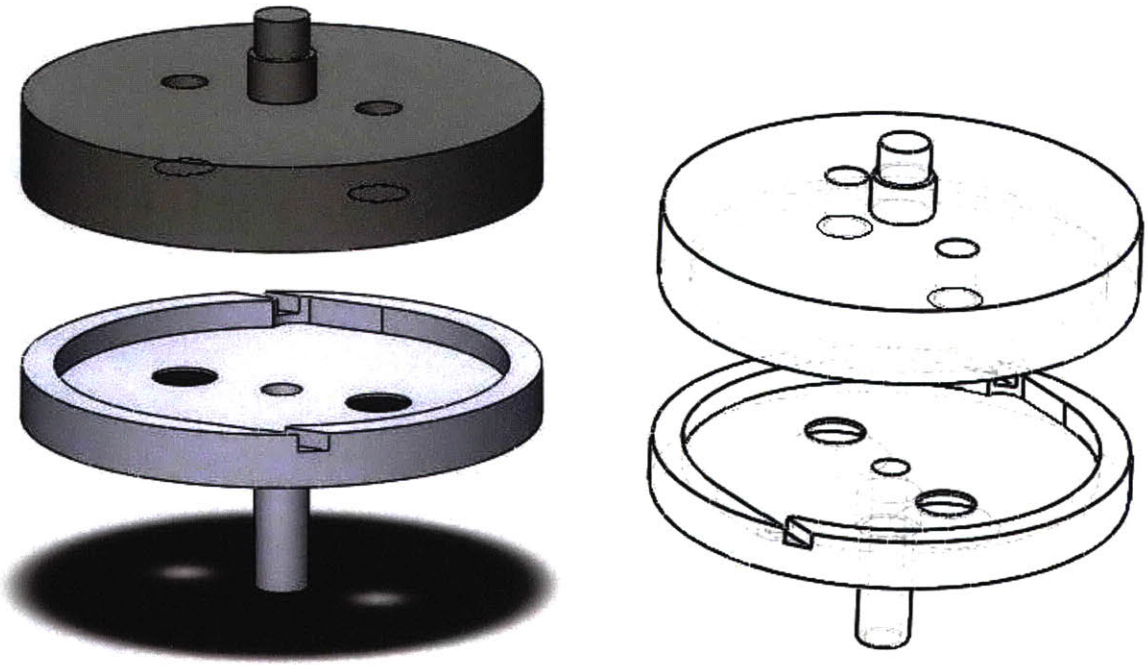

Figure 16. Rotor assembly: exploded view

The exploded view shown in Figure 16 highlights how the two pieces of the rotor come together to form one enclosed volume. There are also two screws, which are indeed constantly rotating through the radial fluid path, which may cause some viscous losses. However, after several iterations of rotor designs with different internal structures, this approach was measured to provide the best performance.

There were significant initial manufacturing challenges with building these two pieces separately.

The first problem encountered was significant leakage around the rim of the joined area.

This was overcome by expanding the radial contact area to be a lip of width 0.075" around the circumference of the both pieces.

The second challenge was alignment. Because both top and bottom pieces were to be held in rotating bearings, it was extremely critical that they were perfectly coaxial. The solution to this problem proved to be to not turn the 0.125" diameter bearing surface region of the bottom rotor piece to its finished diameter until after it was attached to the top piece. The countersinked screws did seem to provide reliable and repeatable alignment, such that the rotor could be disassembled and re-assembled, if the identity of the screw holes was maintained.

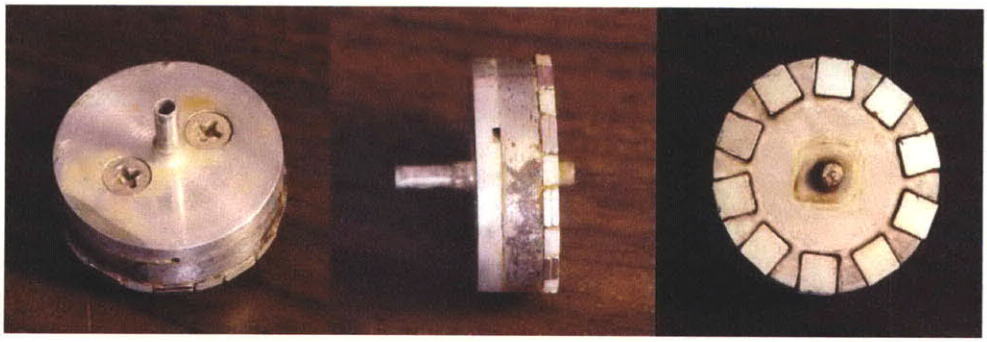

Figure 17. Rotor assembly photo with magnet holder and magnets

The photos in Figure 17 show the final rotor, along with the mounted magnet holder and magnets. (The color on the rotor top piece is due to some oxidation that occured due to the use of non-stainless steel in water.) One of the two rotor outlet nozzles is visible in the center photo.

The two-part rotor design also allows for faster iteration, particularly because the magnetics are contained in the top half, and the fluid flow channels are in the bottom half.

Overall, the rotor lives up to its expectations, maintaining a seal between its two halves, and producing tangentially-directed jets from an axial input.

4 Turbine Stator Design

While the stator of the turbine is a static component, it must fulfill several requirements simultaneously, many of which are core to the proper operation of the rotor. In particular, it must maintain the pressure seal as a closed system, while allowing the rotor to rotate freely in well-aligned bearings and busings. The stator must allow and direct fluid to and from the rotor. Finally, it must hold the generator coils, and act as a magnetic flux return path.

4.1 Fluidic Port Design

To provide for a simple, standardized interface to the 1/8" tubing used outside of the system, a small plastic pipe adapter was used that provided a 1/8" male barb on one side, and a standard #10-32 thread on the other side (McMaster-Carr part number 5643K127). This approach allowed for easy manufacturability and quick testing with different outside devices, such as the check valve arrangements, the bladders themselves, and a constant-pressure test setup.

One compromise made when using this kind of connection is that a significant contraction in hydraulic diameter takes place through the adapter itself. In this case, the diameter quickly changes from 0.125" in a tube, to 0.091" in the adapter. While this does not seem like a tremendous shift, it should be noted that area is proportional to the square of diameter, velocity is inversely proportional to the area, and the flow energy and most losses are proportional to $\frac{1}{2}\rho\bar{v}^2$, so effectively losses are inversely proportional to diameter to the fourth power. In this case, $\left(\frac{0.091}{0.125}\right)^{-4} = 3.56$, which suggests that frictional losses in this area could be 3.5x as bad as losses elsewhere, not to mention losses associated with the sudden contraction and enlargement.

Another concern with this type of interface is leakage. As with any plumbing connection, any non-soldered joint presents a possible flow path through the joint itself. In metal-to-metal plumbing, where the materials of each pipe are quite stiff, a Teflon tape is typically used as an intermediary between the two thread surfaces. This fills up the gaps between the threads, and is displaced and deformed to essentially completely block the undesired flow path. Also, normal household NPT plumbing makes use of tapered threads, where matching tapers provide an extremely strong mechanism for self-alignment and tightening. In contrast, this #10-32 based adapter uses neither a tapered thread nor a intermediate seal. However, because the adapter itself is plastic, the threads are able to elastically deform enough to form a tight seal in the aluminum host.

In practice, some leakage did occasionally occur through these ports, because it was easy for the threads to become slightly loose. When not fully tightened down with the flange of the adapter reacting against the aluminum, the threads were not forced to fully engage. However, when tightened properly, no leakage was observed through the threads. In a finished-product system, a thread sealant adhesive would be used to permanently affix the adapter in place. Ultimately, this system worked well for this development phase of the project, and could be easily made to work on a more permanent installation.

4.2 O-Ring Seal Design

Since the stator is fabricated in three sections and should be a closed fluidic system, it is necessary to provide watertight seals at the interfaces of the sections. To facilitate the multiple open/close cycles needed for a research unit, standard rubber O-rings were used to seal between the sections.

However, in a mass-production unit, the stator would likely be sealed once, and options such as welding or adhesive bonding would probably be preferred for simplicity.

The two O-ring seals have somewhat different pressure requirements. In the original system concept, with the check valves, the O-ring on the inlet side always has to deal with the pressure difference between the high pressure side and ambient, while the O-ring on the outlet side only has to handle the difference low-pressure side and ambient – almost zero. However, when system development occured without the check valve in place, as described later, the higher pressure requirement pertained to both seals.

Standard O-rings have a circular cross-section, and also naturally lie in the form of a circle. To avoid the issue of making the O-ring sit in a non-circular contour path, which would present an additional challenge every time the unit was assembled, the O-ring gland was made circular, so that the ring was unstressed in the radial direction. This also has the effect of prolonging the cycle life of the O-ring, although this was not a primary concern in this application. Choosing circular O-ring glands constrained many of the other sizes in the system, since it is easier to mill rectangular features, but they now must enclose or be enclosed by a circle.

For a given O-ring outside diameter, there are several options for the thickness of the ring itself. In this case, the largest possible size of 0.125" was chosen, because this would tolerate more misalignment while preserving a seal. Following the advice of the Machinery's Handbook, a gland depth of 0.110" was chosen for this seal [12]. This means that the rubber material is crushed by 0.015" in the axial direction, spreading out along the rest of the channel, which provides the sealing action.

Because rubber has a significant tendency to deform rather than compress, it was necessary to provide enough cross-sectional area within the 0.110" tall gland for the entire

cross-section of the original O-ring. Otherwise, the rubber can be forced into the small space between the plates, causing it to be cut on the walls of the gland and fail prematurely.

For the upper O-ring seal, a type 230 O-ring was used, with a nominal ID of 2.500" and nominal OD of 2.750". The gland was cut with an ID of 2.400" and an OD of 2.800".

For the lower O-ring seal, a type 206 O-ring was used, with a nominal ID of 0.500" and nominal OD of 0.750". The gland was cut with an ID of 0.400" and an OD of 0.770".

4.3 Stator Middle Plate Design

The core of the stator is the middle plate, which was machined from 0.750" thick 6061 aluminum. The outside dimensions of 2.900" square were chosen so as to be a reasonable reduction from a 3" rough stock piece.

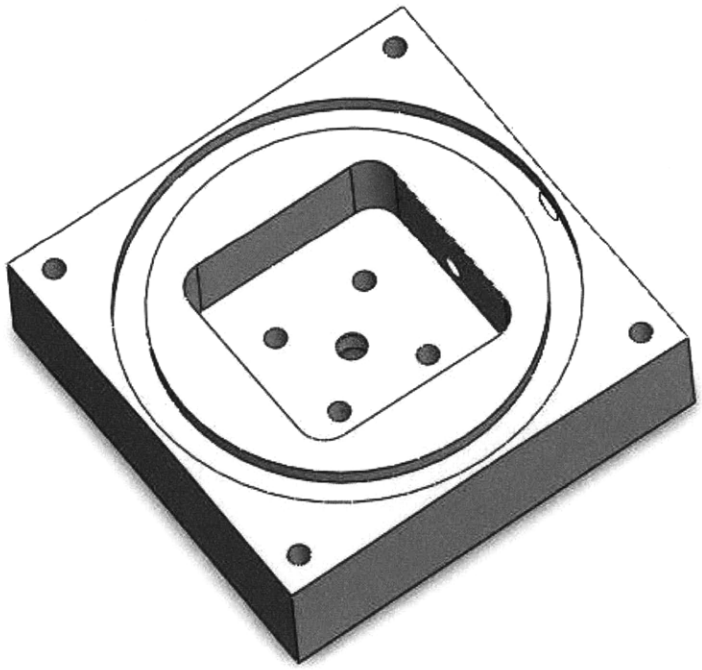

Figure 18. Stator middle plate: top view

As shown in Figure 18, this piece must accomodate mechanical connections to the top and bottom plates, O-ring seals between all plates, the turbine outlet, and the rotating seal and turbine inlet. This figure shows the top view, which highlights the rectangular pocket that is milled into the block. This pocket is filled with water during normal turbine operation, and it is where the fluid exiting the tangential rotor nozzle is directed.

For ease of manufacturing, this pocket was made as a rectangular pocket which was plunge-milled into the face of the block. Its corners therefore take a fillet with the radius of the 0.375" end mill tool used to cut the pocket.

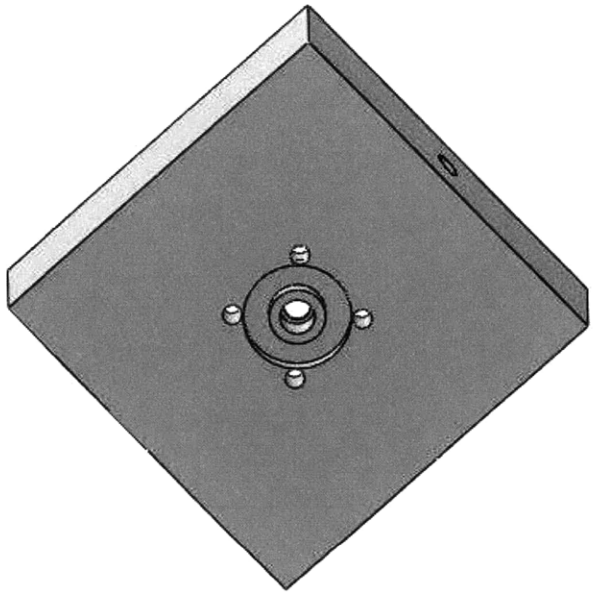

Figure 19. Stator middle plate: bottom view

The bottom view shown in Figure 19 shows where high-pressure fluid enters the turbine. The four screws for the bottom plate do penetrate into the low-pressure fluid area inside the stator, but given the thread length and the low pressure differential, leakage was not a problem here.

From the bottom, a retaining structure for the rotating seal is also constructed. This area has a 0.250" diameter to hold the rotating seal element, while there is a small flange back-stop to prevent the seal from moving up into the stator component.

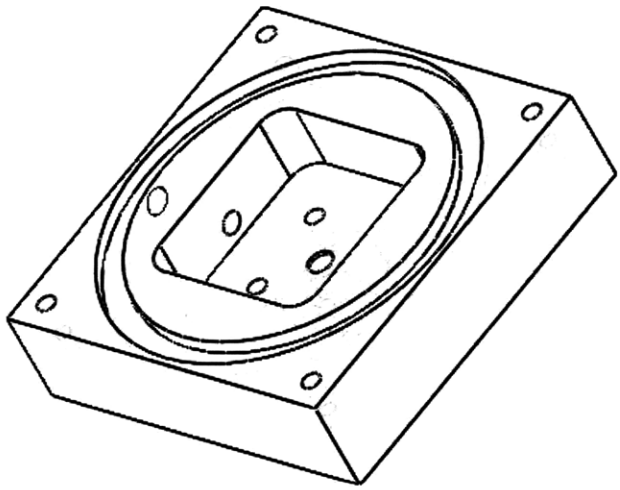

Figure 20. Stator middle plate: wireframe view

The wireframe view shown in Figure 20 highlights the fact that this middle segment of the stator is particularly complex and has many features which are integral to the proper operation of the turbine. However, because it was designed with adaptability in mind, it only had to be machined once during the course of this project.

In future work, this part could be made significantly smaller and lighter simply by removing the constraint that the O-ring gland should be circular, or by making the fluid

pocket itself be circular and just slightly larger than the rotor's outside diameter. This would allow the size of the overall device to shrink considerably, and eliminate a lot of "dead mass" in this component.

4.4 Stator Bottom Plate Design

The bottom plate of the stator is made from 0.250" thick 6061 aluminum. Its sole purpose is to allow the high-pressure working fluid to enter from the tube adapter, turn the flow 90 degrees, and allow it to enter the rotor axially.

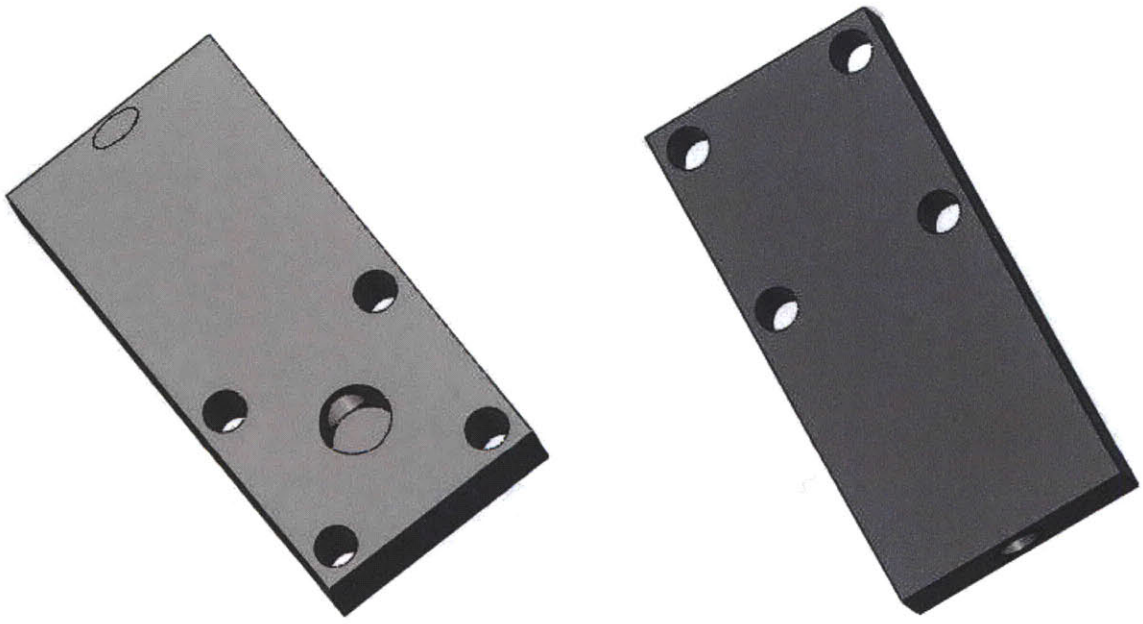

Figure 21. Stator bottom plate: top and bottom views

As is shown in Figure 21, the length of the piece is so as to allow the fluid port to be flush with the wall of the middle stator plate. Otherwise, the adapter might not be able to be screwed in fully and firmly, and the tube might have trouble fitting properly.

After emerging from the adapter, the fluid must travel about 1.2" distance at a diameter of the tap drill for the #10-32 adapter, which is 0.159". At that point, it is suddenly turned and forced into the rotor. A sudden turn like this can be a source of head loss. However, this is a tradeoff that must be made in order to turn the flow without an excessively thick bottom plate. In future iterations, it might be possible to try using a ball-end endmill instead of a square-end endmill, which could be used to create a rounded corner.

4.5 Stator Top Plate Design

The top plate of the stator is machined from 0.250" thick steel (not stainless), painted with blue Krylon spray paint to prevent rusting. The material is intentionally a soft magnetic (ferromagnetic) material, with high relative permeability μ_r. Type 1018 alloy steel was used in the original development work, but later iterations used an unknown, magnetically soft, non-stainless steel alloy provided by the MIT Central Machine Shop.

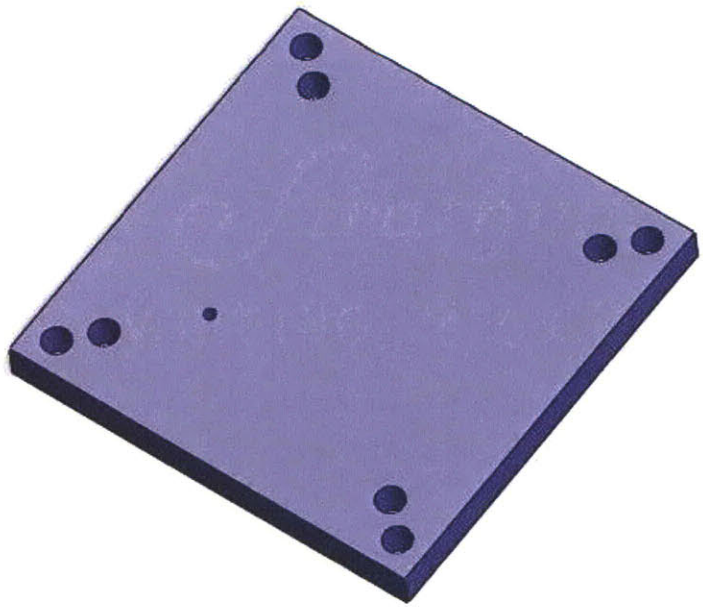

Figure 22. Stator top plate: top side

As is shown in Figure 22, the top stator plate contains mounting holes to attach it to the middle plate, as well as a hole drilled for wire passthrough. While this figure shows 8 mounting holes (2 per corner) and the middle plate shows only 4 (1 per corner), the reality is that a broken #6-32 tap is embedded in the middle plate aluminum. Because this tap was not able to be extracted, alternate mounting holes were prepared. In any case, only one hole per corner is used at any time.

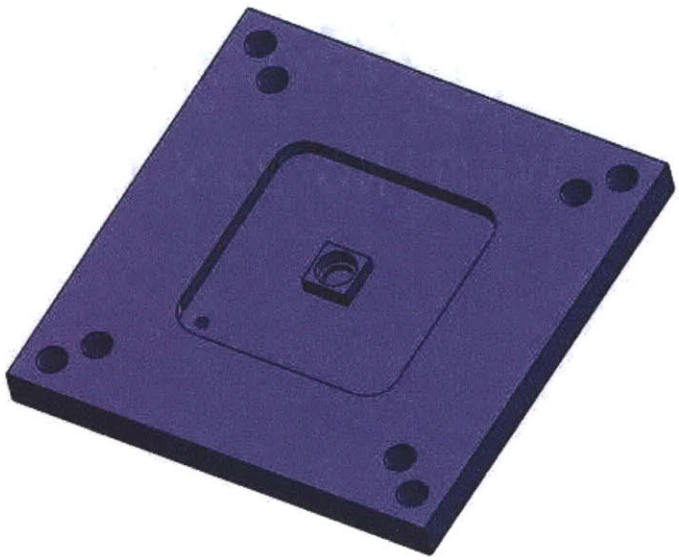

Figure 23. Stator top plate: bottom side

The water-facing side of the top plate is shown in Figure 23. This contains detailed features that are critical to both the electromagnetics and to the mechanical operation of the

turbine. At the center is a milled circular 0.250" diameter pocket to hold the ball-bearing which supports both the thrust load and any radial load of the spinning rotor. Around it is a larger, 1.500" square rounded-rectangle pocket, which holds the electromagnetic coils. The depths of each of these pockets is critical to ensuring proper clearance of the rotor from the coils.

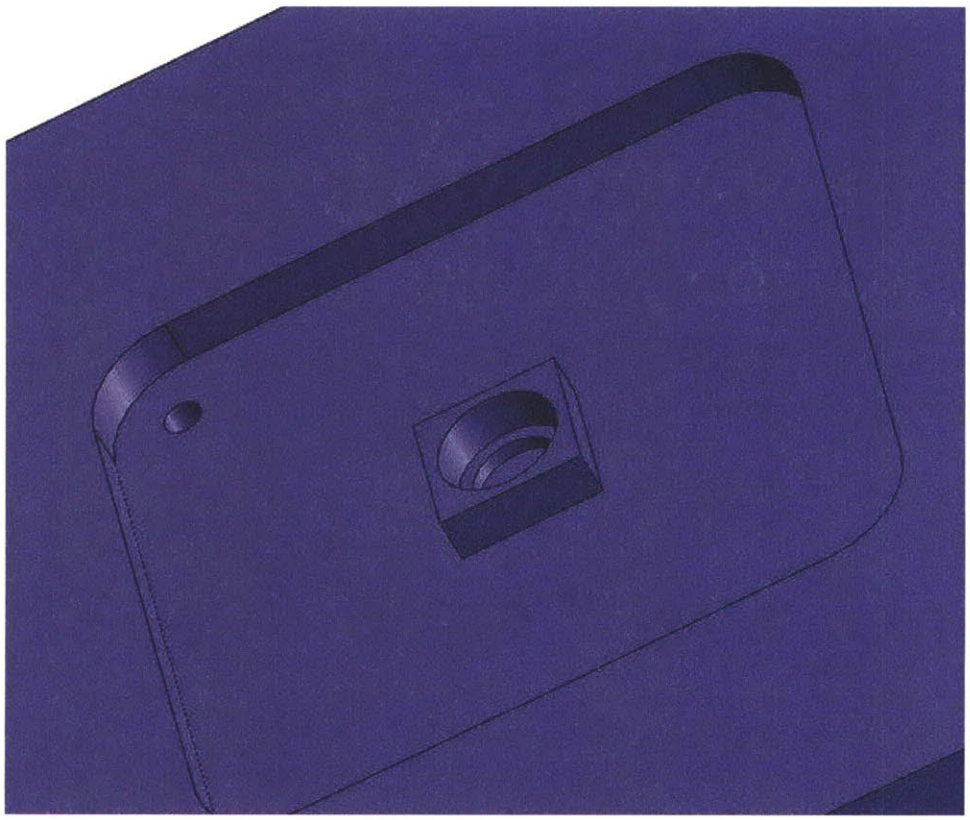

Figure 24. Stator top plate: closeup of bearing pocket

In the close-up of the bearing pocket shown in Figure 24, the two-step bearing pocket can be seen. The outer ring of the ball bearing sits in the outer step, while the inner step is milled at a slightly smaller diameter but only 0.010" deep, simply to prevent the inner ring of the ball bearing from contacting the surface. This allows the inner ring of the bearing to rotate freely, which is critical for proper operation of the turbine.

4.6 Overall Stator Assembly

Eight screws are used to hold together the entire stator assembly: four from the top to middle plate, and four from the bottom to middle plate. All threads are on the middle plate, with the exception of the turbine fluid inlet #10-32 thread on the bottom plate.

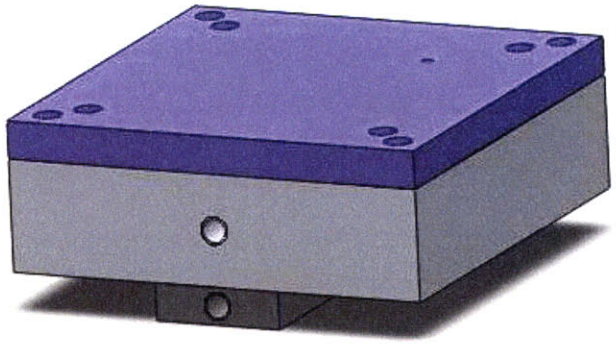

Figure 25. Stator assembly: collapsed view

As shown in Figure 25, both the fluid inlet and outlet are on the same face of the device.

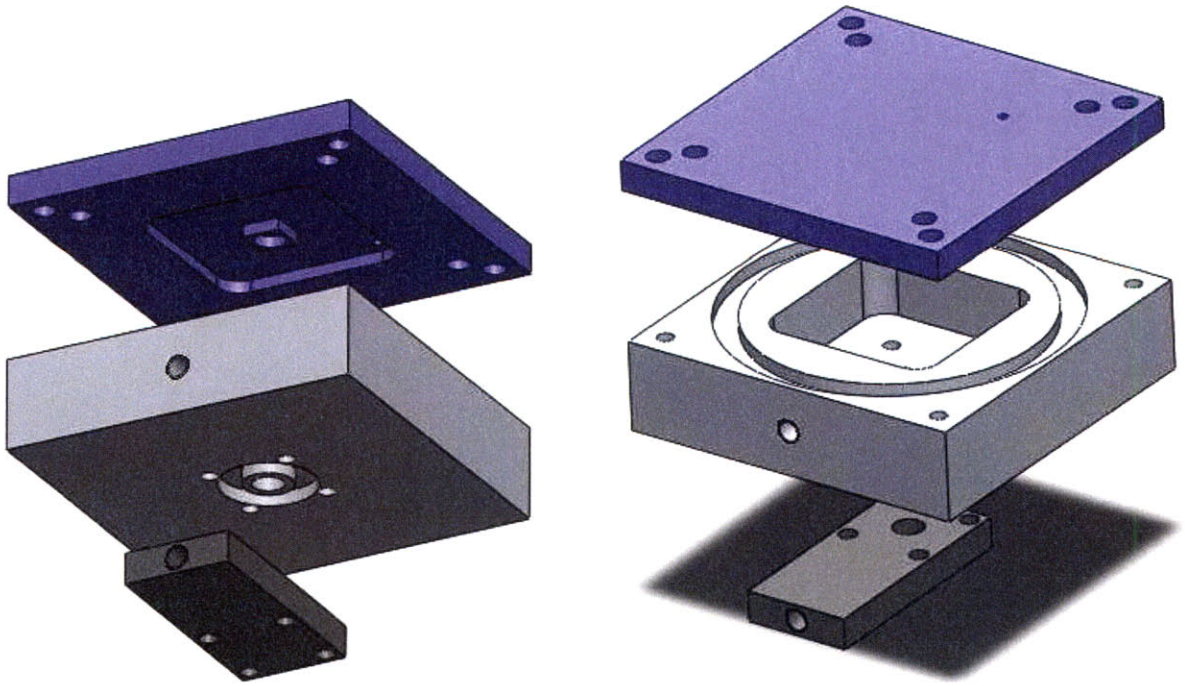

Figure 26. Stator assembly: exploded view

Exploded views of the stator assembly in Figure 26 provide reference for the internal alignment of the parts, and ultimately, of the fluid path.

Although every attempt was made to use good machine shop practice to produce parts to excellent accuracy (on the order of $\pm 0.003''$), there were still several opportunities for this novice machinist to make errors. To account for this, it was necessary to oversize the clearance screw holes at the corners of the top plate. This allowed for the plate to be slightly shifted in any direction, which was important to making sure that the bearing in the top plate was directly centered over the fluid seal in the middle plate. This alignment and final tightening was made while fluid was run through the system and the rotor was allowed to run.

Over the course of the project, the stator remained relatively constant, with only one iteration of the middle plate, two of the bottom plate, and four of the top plate. Overall, it successfully provided a closed system, with the needed fluidic ports, that served the needs of the active rotor and electromagnetics components.

4.7 Ball Bearing Load

To properly choose the type of bearing to be used, it is necessary to estimate the forces that the bearing will see. Bearing lifetime is a strong function of load level.

4.7.1 Radial Loading

Ideally, if all components are balanced around the centerline of the rotor, there will be zero radial loading. Any radial loading results from imbalances. We will estimate the magnitude of three different sources of radial imbalance.

Suppose the entire rotor disc is offset by $0.001" = 25.4\mu m$ from the centerline. (Since this will be made on a lathe, even this level of imbalance in the entire structure is highly unlikely. However, it might result from compliance in the bearings rather than the rotor itself.) At 6245 rpm and a rotor mass of approximately 30 grams, this will result in a radial force $F_1 = m\omega^2 r_{\text{offset}} = 0.326$ Newtons.

Suppose that of the two nozzles, one is pointed with perfectly tangentially, but the other has a 5° offset. For $\dot{V} = 30\frac{\text{mL}}{s}$ and 138 kPa (20 psi), this will result in a net radial force $F_2 = \frac{\dot{m}}{2}\frac{v_{\text{rel}}}{2}\sin(5°) = 0.011$ Newtons.

Suppose that one of the magnets is misaligned by $0.010" = 254\mu m$ at a radius of 13mm. Suppose each magnet weighs about 400mg (5 × 5 × 2mm). This results in a net radial force $F_3 = m_{\text{mag}}\omega^2((254\mu m + 13\text{mm}) - 13\text{mm}) = 0.043$ Newtons.

4.7.2 Thrust Loading

In the axial direction, there are three key forces that need to be supported.

First, there is the gravitational weight of the rotor. This is approximately $F_1 = mg = 0.286$ Newtons.

Second, there is the axial momentum imparted by turning the flow from an axial one into a radial one. From the conservation of momentum for a control volume,

$$\sum F = \frac{\partial}{\partial t}\iiint_V \rho\vec{v}\,\text{dV} + \iint_A \rho\vec{v}\cdot\vec{v}\,d\vec{A} \tag{32}$$

At steady state, and only considering the axial forces, this force $F_2 = \rho\bar{v^2}A \approx \frac{4}{3}\rho A\bar{v}^2$ for laminar flow [21]. Noting that $\dot{V} = A\bar{v}$, we can rewrite $F_2 = \frac{4}{3}\frac{\rho\dot{V}^2}{\pi r_{\text{in}}^2}$. For $\dot{V} = 30\frac{\text{mL}}{s}$, and

$r_{in} = 3/64''$, we have $F_2 = 0.269$ Newtons.

Third, there is a force from the electromagnetic interaction of the rotor magnets and the stator coils. Because the prototype contained only one set of stator coils, there is a magnetic force attracting the rotor to the top plate of the stator. We can estimate this force by considering the gradient of the magnetic field energy. In the low-permeability air gap, the magnetic field energy density is $\frac{1}{2\mu_0}B^2$. The total energy is then:

$$W_m = g \cdot A\left(\frac{1}{2\mu_0}B^2\right) \tag{33}$$

where g is the air gap length, and A is the total magnet area. The force can be found as

$$F_m = \frac{\partial W_m}{\partial g} = A\left(\frac{1}{2\mu_0}B^2\right) \tag{34}$$

With estimated values (explained later in this document) of a magnetic field strength of 0.5 Tesla, a magnet area of $10 \times (0.200'')^2$, and an air-gap of $0.100''$, the force is approximately 25.7 Newtons.

This is a substantial force, and imposes a load on the ball bearing which must be supported. However, this could be substantially nulled by having two sets of magnets and coils: one on top and one on the bottom (which would be advantageous from a power density standpoint as well).

4.7.3 Environmental Loading

Another form of loading that the bearings must accomodate is the inertial shock that the device must take every footstep. By making the turbine not rigidly connected to the base of the shoe, it can accomodate some damping to reduce the peak accelerations involved.

One source claims that the acceleration felt by the leg bones at impact is 5-15g [16]. If a similarly large impact is felt by the turbine, there will be an axial force of $F_1 = 15mg = 4.3N$. This shock is felt for a relatively short amount of time, and the duration is inversely proportional to the magnitude ($v_f = v_o + at$).

4.8 Ball Bearing Lifetime

Since reliability is a key constraint, we want to guarantee that if the system must last 5.3×10^6 steps (one year at 4 hours per day of 1Hz walking), and is revolving at 6245 rpm or 104 Hz, we require that the ball bearings can last for 551 million revolutions! The basic equation for estimating bearing life is, from [5]:

$$L_{10} = \left(\frac{C}{P}\right)^3 \times 10^6 \text{ revolutions} \tag{35}$$

where C is the dynamic load rating of the bearing (from the manufacturer), P is the equivalent dynamic load, and L_{10} is the number of revolutions that 90% of the bearings will survive. We therefore require $\frac{C}{P} \geqslant 8.2$. The equivalent dynamic load is related both to the axial and radial loads, and a quick conservative estimate is $P = F_r + 3F_a$. Radial is easy, about 0.4 Newtons from our approximations above. Our axial load varies, and the literature suggests a way of time averaging:

$$F_a = \sqrt[3]{\frac{1}{T}\int_T F_a^3 \, dt} \tag{36}$$

So for the 15g axial environmental load occuring for 10% of the time, $F_a \approx 25.8$ Newtons. (This is almost entirely dominated by the unbalanced attractive force due to single-sided magnetics!) This yields a total estimated $P = 77.8N = 17.5$ lbf. Therefore, we require a

bearing rated for a dynamic loading of $C \geqslant 143.5\,\text{lbf}$. This is large for off-the shelf parts.

However, if the unbalanced magnetics were instead replaced by magnets on both sides of the rotor, therefore mostly cancelling the attaction to the top side, the bearing load will be greatly reduced. The bearing reliability constraint can then be satisfied by off-the-shelf parts. For example, on McMaster-Carr, part 57155K346 is a 1/8"ID, 1/4"OD bearing rated for $C = 64\,\text{lbf}$ and 80,000rpm, for $6.62.

4.9 Rotating Seal Design

The seal present in the stator middle plate must serve two important purposes: 1) prevent leakage across the pressure differential from the high-pressure inlet to the low-pressure exhaust, and 2) allow the rotor to spin freely.

A first attempt at designing a rotating seal utilized a ball bearing plus a long, narrow annulus between the rotor shaft and the metal of the stator middle plate. However, the issues were numerous, including that it allowed for too much leakage based on calculations (even for 0.001" radial clearance, which would have been extremely difficult to machine), and in practice was impossible to align so as to make it spin at all.

The concept of a rigid annulus to arrest the flow was therefore abandoned, and instead a nylon bushing was used as a rotating seal element, both to simultaneously provide the proper bearing constraints on the rotor and also to prevent flow across the pressure differential. The nylon bushing measured 0.250"OD, 0.125"ID, and 0.250" long. By now making the rotor shaft slightly oversized, we could use friction to our advantage, allowing the nylon busing to wear slightly in order to perfectly accomodate the diameter of the

shaft.

4.9.1 Rotating Seal Testing

Because of concerns that fluid would leak between the outer diameter of the rotor shaft and the inner diameter of the seal element, a simple test was devised to estimate leakage through this annulus. The rotor was separated into its two halves, and the inner volume was filled with ordinary printer paper, cut and folded to the approximate inner shape of the rotor, and the rotor was then reassembled. This prevented any fluid from traveling up the axial flow path of the rotor and out through the tangential nozzles (as verified by applying a pressurized tube directly to the axial rotor inlet).

In this "clogged" state, the rotor was allowed to sit in the seal element with the stator middle and bottom plates assembled. With only manual force applied to counter the thrust of the pressure differential in order that the rotor not shoot upwards, any leakage into the stator volume was observed. In practice, essentially zero leakage was observed up to 30psi – far less than 1mL/sec, and too little to measure.

This test suggests that the rotating seal presents an extremely tortuous flow path. In fact, this result is so good that it raises concerns that the seal might be too tight, and might be providing excess friction. Future experimenters might attempt to use the electromagnetic coil arrangement to measure static friction "in-vivo" – with the system fully submerged, and with the generator coils instead being used to attract or repel the magnets. The current requried to produce any non-zero back-EMF could be used along with the measured back-EMF constant to solve for the static frictional torque present.

5 Electromagnetics Design

After the turbine converts pressure energy into rotational kinetic energy of the rotor, the system must next convert this rotational kinetic energy into electrical energy. Conventional electromagnetic motors and generators have efficiently served this purpose for more than a century at a wide variety of scales. Time-varying magnetic flux through a wire coil will induce an EMF, which can drive a current in order to deliver electrical power to a load.

Although motors at all scales are widely available commercially, and have been optimized in their performance, a key goal of this project was to integrate the electromagnetics into the same rotor as the turbine to demonstrate that future miniaturized versions might be feasible. Although all permanent-magnet motors can be run reversibly as a generator, using an external motor would have added the complexity and reliability issues associated with gearing and associated losses, plus either running that motor submerged in water, or adding a rotating seal that would transmit torque but not allow fluid to leave the closed system. Magnetic couplings can be used to transmit torque through a barrier that is impermeable to fluid, however this would have further increased the size of the overall device. As one project goal was to produce a maximally flat system design, the integrated generator-turbine was pursued.

The turbine was first developed without any electrical generation capability. This was done by manufacturing the rotor top plate out of 0.250" thick transparent polycarbonate. (The design of this transparent stator top plate was identical to the steel top plate used in the final product described earlier, except that no pocket for generator coils or wire passthrough was created. This allowed the part to be almost entirely created on the 2D

waterjet, except for the bearing pocket which requried two simple plunge-mill operations.) This direct visibility into the stator fluid chamber aided the initial diagnostics, and also allowed for no-load performance measurements in the form of tachometer readings using alternating light/dark areas temporarily added on the top of the rotor. All iterations of the rotor design took place with this transparent stator top.

In the initial phase of generator design, it was already clear that cogging torque, which is the tendency of a motor/generator to magnetically prefer a particular orientation, could be a problem. The initial generator design made use of a low cogging torque design, but not a truly zero cogging torque, and in fact this proved to be too great a barrier for the turbine to overcome. Because the cogging torque plus static frictional torque was greater than the fluid torque from the rotor, the rotor would not spin at all.

A new generator design, which traded a more complicated manufacturing process for zero cogging torque, was pursued, and this is the design discussed here.

5.1 Generator Design Equations

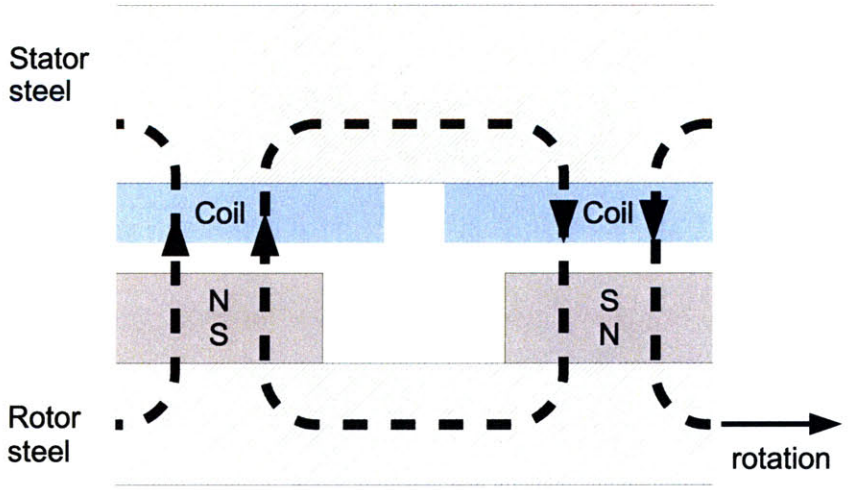

Figure 27. Generator magnetic flux path

The analysis of magnetic circuits is analogous to electrical circuits in many ways. After sketching the flux path caused by the rotor's permanent magnets, we can write:

$$\oint \overline{H} \cdot d\bar{l} = \sum \text{MMF} \tag{37}$$

For a permanent magnet, the MMF equivalent amp-turns is $\frac{B_r L_{\text{magnet}}}{\mu_{\text{magnet}}}$, where here $\mu_{\text{magnet}} = \mu_0$. The full magnetic circuit equation is then:

$$2H_{\text{airgap}}(L_{\text{airgap}} + L_{\text{magnet}}) + 2H_{\text{steel}}L_{\text{steel}} = 2\,N_{\text{turns}}\,I_{\text{coil}} + 2\frac{B_r L_{\text{magnet}}}{\mu_{\text{magnet}}} \tag{38}$$

Because the relative permeability of the back iron on both rotor and stator is much greater than unity, we will assume $\mu_{r,\,\text{steel}} \gg (\frac{L_{\text{steel}}}{L_{\text{airgap}} + L_{\text{magnet}}})(\frac{A}{A_{\text{steel}}})$. With this in mind, we can simplify the equation, and also solve for the zero-current case:

$$H_{\text{airgap}}(L_{\text{airgap}} + L_{\text{magnet}}) = \frac{B_r L_{\text{magnet}}}{\mu_{\text{magnet}}} \tag{39}$$

or since $\mu_{\text{magnet}} = \mu_0$ and $B_{\text{airgap}} = \mu_0 H_{\text{airgap}}$,

$$B_{\text{airgap,max}} = B_r \frac{L_{\text{magnet}}}{L_{\text{airgap}} + L_{\text{magnet}}} \tag{40}$$

This neglects the effects of fringing fields, but provides a simple and useful design guide.

With the designed $L_{\text{magnet}} = 0.080''$, $L_{\text{airgap}} = 0.100''$, and $B_r \approx 1.2T$, we get $B_{\text{airgap,max}} = 0.53T$. To use a conservative round number, $0.5T$ will be used in future calculations.

Now, using Faraday's Law:

$$\text{EMF} = \oint \overline{E} \cdot d\bar{l} = -\frac{\partial}{\partial t}\int\int_A \overline{B} \cdot d\bar{s} \tag{41}$$

over the coil, so we can write the instantaneous voltage for N_{turns} turns of the coil area A:

$$V_{\text{coil}} = A N_{\text{turns}} \cdot \frac{\partial}{\partial t}(B_{\text{airgap}}(t)) \tag{42}$$

Since the airgap field strength $B_{\text{airgap,max}}$ calculated in Equation 40 will be alternating in polarity as the magnets pass over the coil, we can assume a roughly sinusoidal integrated

field through any coil with time. When the turbine is rotating at a mechanical angular velocity of ω_m, the perceived field changes occur at a rate of

$$\omega_e = \omega_m \cdot \frac{N_{\text{magnets}}}{2} \tag{43}$$

as one full magnetic cycle occurs after two magnets pass a coil. So given the electrical frequency and the maximum field strength, we can model the time-varying field strength through any coil as:

$$B_{\text{airgap}}(t) = B_{\text{airgap,max}} \times \sin(\omega_e t) \tag{44}$$

Substituting Equation 44 into Equation 42 and taking the derivative, we find:

$$V_{\text{coil}}(t) = A N_{\text{turns}} B_{\text{airgap,max}} \omega_e \times \cos(\omega_e t) \tag{45}$$

To account for the entire generator, and all individual coil voltages adding in series, we must multiply by $N_{\text{coils}} = N_{\text{magnets}}$, and we will also rewrite in terms of the mechanical frequency ω_m:

$$V_{\text{generator}}(t) = A N_{\text{turns}} B_{\text{airgap,max}} \omega_m \frac{1}{2} N_{\text{magnets}}^2 \times \cos(\frac{1}{2} N_{\text{magnets}} \omega_m) \tag{46}$$

The RMS voltage can be computed as:

$$V_{\text{generator, RMS}} = \frac{1}{2\sqrt{2}} A N_{\text{turns}} B_{\text{airgap,max}} N_{\text{magnets}}^2 \omega_m \tag{47}$$

Normally, motors and generators are characterized by a back EMF constant, or by an (equivalent) torque constant. For this design, relative to RMS voltages and currents,

$$K_t = K_e = \frac{V_{\text{generator,RMS}}}{\omega_m} = \frac{1}{2\sqrt{2}} A N_{\text{turns}} B_{\text{airgap,max}} N_{\text{magnets}}^2 \tag{48}$$

where SI units are $\frac{Nm}{A} = \frac{Vs}{\text{rad}}$. For the current design, with $A = (0.200'')^2$, $N_{\text{turns}} = 130$, $B_{\text{airgap,max}} = 0.5T$, $N_{\text{magnets}} = 10$, the calculated value is:

$$K_t = K_e = 0.0593 \frac{Vs}{\text{rad}} = 6.21 \times 10^{-3} \frac{V}{\text{rpm}} \tag{49}$$

However, the area of each turn is not $(0.200'')^2$, and in fact there is a large variation of area between the inner and outer turns of each coil. For a square coil with small wires, inner side length l_0, and outer side length $l_0 + 2A$, the average coil area per turn is $l_0^2 + l_0 A + \frac{1}{3}A^2$. Because our coils are almost square with $l_0 = 0.100''$ and $A = 0.100''$ (see generator coil drawing in the appendix), this gives an average coil area of 0.023in^2, instead of 0.04in^2, which is a 42% decrease in A, and also a 42% decrease in K_t, for $K_t = 0.0346 \frac{Vs}{\text{rad}} = 3.62 \times 10^{-3} \frac{V}{\text{rpm}}$. A more detailed numerical model, which accounts for the actual trapezoidal shape of the turns but adds at most 0.04in^2 area per turn (because a turn that is bigger than the magnet will not contribute more flux area), suggests an average coil area of 0.0313in^2, and thus:

$$K_t = 0.0464 \frac{Vs}{\text{rad}} = 4.86 \times 10^{-3} \frac{V}{\text{rpm}} \tag{50}$$

Given the earlier assumptions about the steel being an insignificant factor in the magnetic flux path analysis, it is reasonable to check to verify that the steel does not saturate, and to see what thickness is required to avoid saturation. For 1018 carbon steel, $\mu_r > 100$ for approximately $B \leqslant 1.8T$. In this case, because of Gauss's law for magnetic fields, $B_{\text{airgap}} A = A_{\text{steel}} B_{\text{steel}}$. For the airgap field strength of approximately 0.5 Tesla, saturation of the steel is avoided as long as the steel on either side is approximately 0.056" thick or more.

5.2 Cogging Torque Reduction

The initial generator design made use of the high-permeability steel stator top, but with ten 0.107" (#36) holes drilled around a circle at the same diameter of the magnets. These holes were filled with flat-head #6-32 non-magnetic steel screws, and inserted until they had approximately 0.015" clearance below the stator plate plane. They were then hand-

wound with 36 turns each of 33AWG magnet wire. There was only one continuous stretch of wire for all ten coils, with alternating winding direction for adjacent coils, to make sure that the EMF added properly in series during operation. After winding, a small amount of cyanoacrylate was applied to restrain the wire.

However, while a constant-pressure test rig was able to deliver enough pressure to the turbine to spin this rotor and generate electrical power at 10psi ($\approx$ 68kPa) and higher, human weight on the pressure bladders was not sufficient to spin the rotor at all. This was due to the excessively large cogging torque of the old stator design. It was clear from non-submerged testing that the rotor had a strong preference toward aligning its magnets with the areas of the stator that were not drilled away (i.e. with the center of the magnets fully out of phase with the center of the coils).

A first-order model of cogging torque can help predict the degree of this effect. Given that the magnetic field density is $\frac{1}{2\mu_0}B^2$, and assuming that the magnitude of the magnetic field is constant and equal to 0.5 Tesla, and an air gap of 0.100", we can use the stator-magnet axial area overlap to estimate the roughly sinusoidal cogging torque. At 0° and 36° of mechanical stator rotation, the magnet is fully overlapping the stator. However, at 18°, an area equal to the tap drill circle size is missing. This corresponds to a volume of $\pi \times (\frac{0.107''}{2})^2 \times 0.100'' \times 10$ magnets, for a total energy of 14.6mJ. Assuming a roughly sinusoidal magnetic field energy profile (particularly applicable because of the round hole shapes overlapping square magnets) with a period of 36° mechanical degrees and peak-to-peak amplitude of $14.6\text{mJ} = 2K$, we can write the magnetic field energy:

$$W_m \approx K - K\cos(10 \cdot \theta) \tag{51}$$

and since torque is a derivative of this energy, $T(\theta) \approx 10K\sin(10\theta)$, which gives a peak cogging torque of $10K = 73.0\,\text{mNm}$.

This cogging torque proved to be too great for the rotor to begin motion under human power. Therefore, the system was redesigned as described in this document, with no screws and therefore no voids in the stator back iron.

There are other techniques that might be considered in future work to minimize air-gap length (allowing for a high-permeability material as stator teeth) while still controlling cogging torque. These include having a different number of coils and magnets, so that the cogging torque contributions from individual teeth do not align in phase with each other. However, this would require a more complicated electrical configuration, as it would not allow the coils to be simply wound in series with one another.

5.3 Magnet Holder Design

For the rotor, nickel-plated neodymium type N50 rectangular magnets measuring 5x5x1mm were used (M0516 from Engineered Concepts). For the present configuration, a double thickness (2mm) was used to allow for greater MMF in the magnetic circuit. In order to align the magnets radially around the rotor, a magnet holder was machined from aluminum.

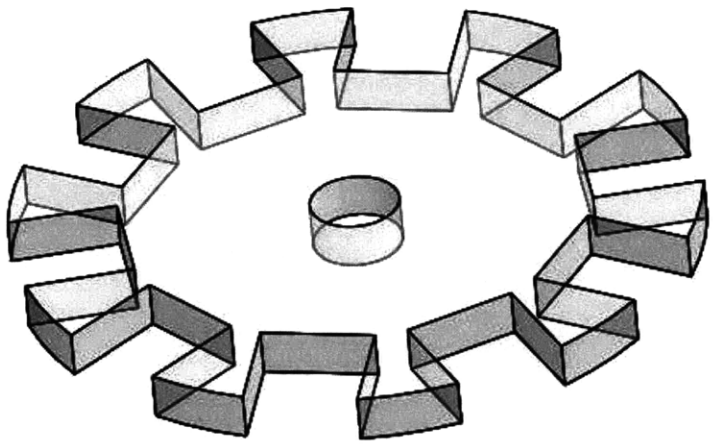

Figure 28. Magnet holder: top view

As shown in Figure 28, the magnet holder is a 2D piece of aluminum, which has the same thickness as the stack of two magnets (2mm). The center hole fits on to the turbine rotor top piece, and one face of the magnet holder rests against the face of the rotor top piece.

The magnet holder is intentionally made from a non-magnetic material. Aluminum was used because of its easy availability and good machinability, but a plastic or a non-magnetic stainless steel could also be used.

Because its contours are completely two-dimensional, and because sharp interior corners are required to match the rectangular magnets, cutting the part via CNC abrasive waterjet was an ideal match as a manufacturing process. Sharp interior corners are not available via conventional milling, so the waterjet's sub-0.015″ kerf diameter allowed for an extremely tight cut.

After the waterjet, a hand file was used to eliminate rough edges and to properly fit the magnet holder onto the rotor top piece. No adhesive was used. The magnets were inserted into the 10 slots, with two magnets per slot, and with alternating north/south poles facing outward in each slot. No adhesive was used on the magnets themselves, either – being placed against the high-μ_r steel rotor top kept them (and the magnet holder) firmly affixed.

5.4 Coil Design and Fabrication

As described earlier, the first iteration of the stator electromagnetics had 36 turns of 33 AWG magnet wire wire wound around 10 #6-32 flat-head screws. However, due to the cogging torque issues mentioned, a new design was pursued.

While most traditional motors and generators have steel teeth around which coils can be wound, this also imposes cogging torque issues as described earlier. To truly eliminate cogging torque, there can not be any materials which are have $\mu_r \neq 1$ distributed non-rotational-symetrically in the proximity of the magnets. So instead of forming coils around steel teeth, we can switch to alternative non-paramagnetic/ferromagnetic materials, or form them around nothing at all.

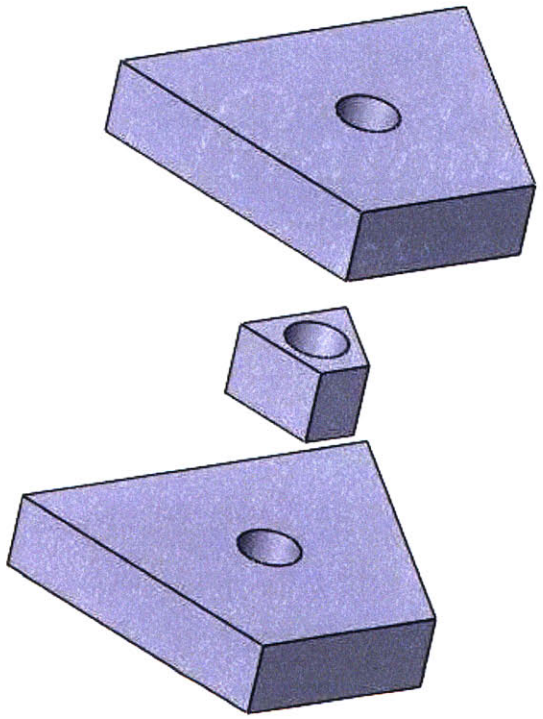

Figure 29. Generator coil form, exploded

With the help of Don Fyler and Andrew Pinkham at Draper, self-supporting coils of magnet wire were produced that served as the new stator windings. First, a coil form was produced that served as the template for the coil, as show in Figure 29. Using 2mm (0.079″) thick plastic, trapezoidal forms to fill the (unwound) center of the coil, plus two for the top and bottom, were formed. A single 1/16″ clearance hole for a #0-80 screw

was drilled through all three. A #0-80 $\times$ 1″ screw and nut was used to clamp down on the form.

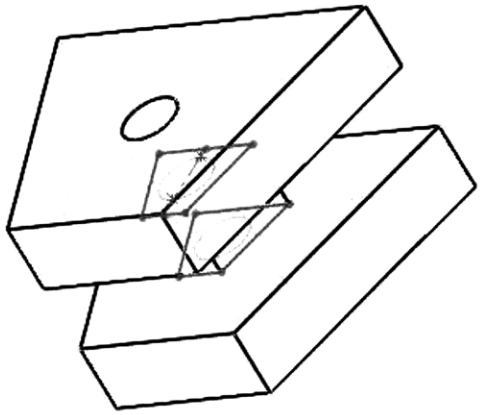

Figure 30. Generator coil form, collapsed wireframe

The 36 AWG magnet wire used here has a special insulation overcoat composition that was labeled "self-bonding" or "Bondeze No. 2". This insulation coat is an epoxy resin adhesive, which is activated by exposure to isopropyl alcohol.

Special tooling in the magnetics laboratory at Draper Laboratory was used to manufacture. The coil winding setup involved a constant-tension magnet wire dispenser, plus a lathe-like motor-driven spindle and turn counter.

The procedure for coil winding was as follows:

1. Tighten and mount #0-80 screw with coil forms. Set winding control for "Top Going", 25 turns.
2. Repeat 5x: run, add 1-2 drops isopropanol, reset counter. (130 turns total; counter adds one per run)
3. Cut with $\sim 6-8''$ of wire remaining. Remove #0-80 screw with coil forms.
4. Blow dry with cool air, 10 seconds.
5. Hot air gun, 30 seconds.

6. Cool down, 30 seconds.

7. Loosen #0-80 nut, disassemble, and gently use tweezers to remove coil from form.

The above procedure evolved after experimentation to yield good separation from the form and a strong self-supporting coil. It was repeated for each of the ten coils. Each coil was individually placed and glued to the painted steel stator top piece using cyanoacrylate. This had the added advantage of adding to the strength of the coil itself.

The two leads from each coil pass through a single hole in the steel stator top plate. The hole is then sealed with standard two-part epoxy against the internal water pressure.

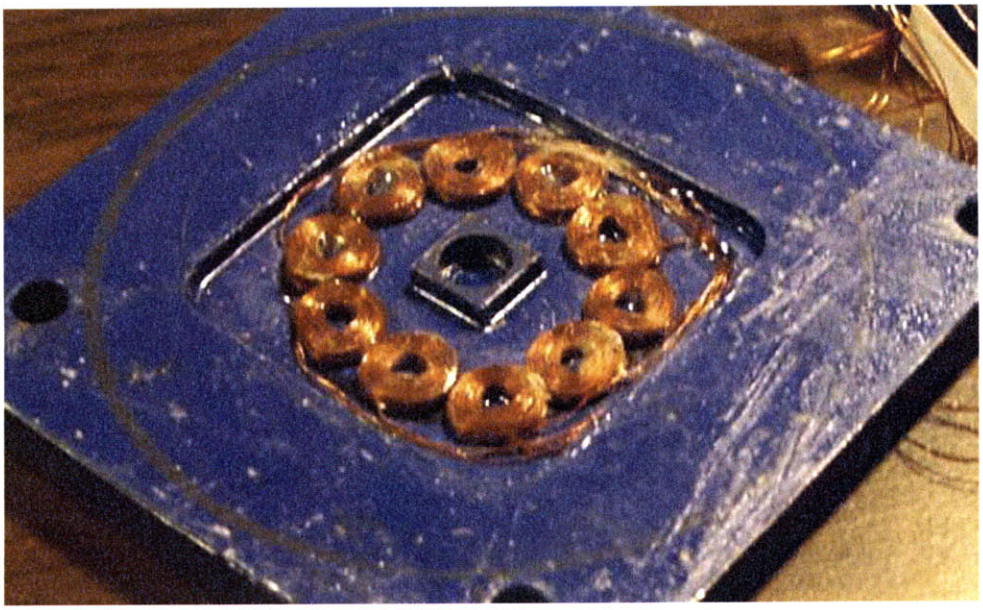

Figure 31. Generator coils mounted on stator top plate

Externally, the ten coils are wired in series. A two-channel oscilloscope was used to correctly determine the polarity of each coil. The rotor was spun by hand, while the traces from two coils were monitored on the scope. In this way, it was possible to assign the proper polarity to all coils so that the EMF generated from each would add and not cancel.

Figure 32. Generator stator coils externally connected in series

As shown in Figure 32, a small prototyping printed circuit board is attached to the exterior of the stator top plate, providing a simple attachment point for the 20 magnet wires to be connected in series.

5.5 Maximum Extractable Power

For a voltage source V and source resistance R, the maximum power transfer theorem indicates that the greatest instaneous power deliverable to a matched load (also of resistance R) is equal to $\frac{V^2}{4R}$. Given the back EMF constant of the generator and its DC resistance, the maximum power as a function of angular velocity is:

$$P_{\max}(\omega) = \frac{K_e^2}{4R}\omega^2 \tag{52}$$

For the best estimate value of K_e calculated earlier in Equation 50, and of $R = 32.3\Omega$ measured for our coils,

$$P_{\max}(\omega) = 1.67 \times 10^{-5} \cdot \omega^2 \left[\frac{\text{Watts}}{(\text{rad}/s)^2}\right] = 1.83 \times 10^{-7} \cdot \omega^2 \left[\frac{\text{Watts}}{(\text{rpm})^2}\right] \tag{53}$$

However, it should additionally be noted that by using only the DC electrical resistance, there is the inherent assumption that the rotor is being driven by a "constant speed" source – that it will maintain a constant ω for any torque (such as the torque that would be applied because of the current running through the coils while generating electricity). In reality, a constant pressure source will mean that there is an additional resistance R_{mech} to be transformed in series with the electrical resistance $R_{\text{elec}} = 32.3\,\Omega$, reflecting the change in speed for a particular electromagnetic torque loading, so that this new total impedance $R_{\text{mech}} + R_{\text{elec}}$ (or really its non-linear curve) is what should be used for matching for maximum power extraction.

5.6 Eddy Current Loss Analysis

Inside the steel plate of the stator, the time-varying magnetic fields will cause induced voltages. Given the finite conductivity of the steel, this will cause currents to flow, and consequently will cause resistive power dissipation in the material.

To get intuition about the magnitude of the eddy current losses, we first need to consider Ohm's law in the material:

$$\overline{J} = \sigma \overline{E} \tag{54}$$

where $\overline{J}$ is current density $[A/m^2]$, σ is conductivity $[\frac{1}{\text{ohm} \cdot m}]$, and $\overline{E}$ is the electric field vector $[V/m]$. The power dissipation per unit volume is the product of the current density and the field strength:

$$\overline{p}_{\text{loss}} = \overline{J} \cdot \overline{E} = \sigma \| \overline{E} \|^2 \tag{55}$$

The total power dissipation will be equal to this density $\bar{p}_{\text{loss}}$ integrated over the active volume of the steel.

While numerical techniques are often used to estimate the induced electric field $\overline{E}$ and therefore the power dissipation, it is also possible to obtain a rough analytical estimate that yields more intuition about what design variables can be controlled.

For this estimate, we will consider a cylindrical disc with height h and radius R, exposed to a uniform but time-varying magnetic field $B_z(t)$ that is oriented only axially with the cylinder. This is analogous to the section of steel on the stator directly underneath one of the magnets as it is rotating. From Maxwell's equations we can write,

$$\overline{\nabla} \cdot \overline{E} = 0 \tag{56}$$

$$\overline{\nabla} \times \overline{E} = -\frac{\partial \overline{B}}{\partial t} \tag{57}$$

Since we expect no electrical field or variation in the axial direction, $\overline{E}_z = 0$ and $\frac{\partial E_x}{\partial z} = 0 = \frac{\partial E_y}{\partial z}$. This allows us to simpify the curl operator:

$$\overline{\nabla} \times \overline{E} = \hat{z}\left(\frac{\partial E_y}{\partial x} - \frac{\partial E_x}{\partial y}\right) \tag{58}$$

and given the cylindrical geometry, we can propose a trial solution:

$$\overline{E}(x, y) = K(-y\hat{x} + x\hat{y}) \tag{59}$$

which does in fact satisfy the zero-divergence property, and also satisfies the boundary condition of zero $\overline{E}$ perpendicular to the cylindrical edge (required to ensure that no currents would be flowing at that edge). Applying the curl above, we find

$$\overline{\nabla} \times \overline{E} = 2K\,\hat{z} \tag{60}$$

Now, if we consider the fundamental component of the time-varying magnetic field due to the magnets passing by to be sinusoidal,

$$\overline{B}(t) = \hat{z}\, B_{\max} \sin(\omega_e t) \tag{61}$$

where ω_e is the electrical frequency and $B_{\max}$ is the peak flux density. Equating the curl from Equations 57 and 60, and substituting in Equation 61, we find

$$K(t) = \frac{1}{2} B_{\max} \omega_e \sin(\omega_e t) \tag{62}$$

This allows us to know the full electric field distribution in the cylinder as a function of time. From Equation 55, we can now calculate the total ohmic power dissipation due to eddy currents:

$$P(t) = \int\int\int \sigma \|E\|^2 \, \mathrm{dV} = \sigma K^2(t) 2\pi h \int_0^R (\sqrt{x^2+y^2})^2 \, r\, dr = \sigma K^2(t) 2\pi h \int_0^R r^3 dr \tag{63}$$

$$P(t) = \frac{1}{2} \sigma K^2(t) \pi h R^4 \tag{64}$$

The time-averaged power dissipation can be obtained by observing that $K^2(t)$ and therefore $P(t)$ is dependent on $\sin^2(\omega_e t)$, the average value of which is $\frac{1}{2}$. The average power dissipation is then:

$$\overline{P} = \frac{1}{4} \sigma B_{\max}^2 \omega_e^2 \pi h R^4 \tag{65}$$

The power dissipation in Equation 65 is for a single cylindrical region of the stator plate experiencing a uniform but time-varying magnetic field. One such region exists for each of the ten magnets used in the rotor, so for ten magnets, the total power dissipation would be the above multiplied by ten.

$$\overline{P}_{\text{eddy}} = N_{\text{magnets}} \cdot \frac{1}{4} \sigma B_{\max}^2 \omega_e^2 \pi h R^4 \tag{66}$$

To estimate the actual losses, we can substitute in appropriate parameters: $\sigma = (1.6 \times 10^{-7}\,\text{ohm} \cdot m)^{-1}$ for the low-carbon steel plate, $B_{\max} \approx 0.5$ Tesla, $h = 0.150''$ steel thickness, and $R = 0.100''$ as an approximation to the $0.200''$ square magnet size. We then find

$$\overline{P}_{\text{eddy}} = 1.95 \times 10^{-6} \omega_e^2 \tag{67}$$

so for example for $\omega_e = (80\text{Hz} \times 2\pi)$, $\overline{P}_{\text{eddy}} = 0.493$ Watts. This is a substantial amount of power dissipation at this scale.

However, Equation 66 also provides clues as to how to reduce the impact of eddy current losses.

First, these losses can be dramatically reduced by choosing a material with lower electrical conductivity σ, such as ferrite. (Steel has conductivity of the order $10^6 \frac{1}{\Omega m}$, while various ferrites are commonly on the order of 10^0 to $10^{-3} \frac{1}{\Omega m}$.)

Second, the thickness of the stator plate can be reduced, although this will have competing effects with $B_{\max}$ and adjusting flux concentration in the plate, possibly leading to magnetic saturation of the material.

Finally, the effective radius R can be reduced, which is the technique used in transformer and motor laminations. By breaking up conductive paths and thus adding more paths along which $\overline{E} \cdot \hat{n} = 0$, the eddy current losses can be greatly reduced. Since the dependence is on R^4, attemps in this direction are likely to result in swift improvements. However, particularly in an axial-flux machine like this one, it is difficult to build laminations axially while retaining structural integrity and a secure fluid seal.

However, all of these techniques present opportunities for the reduction of eddy current losses and future improvement of this design.

6 Shoe Integration

This chapter will describe the requirements involved in integrating the fluidic system with a shoe.

While the size of the turbine's active components are pursued on a scale that may lead to integration within the sole of the shoe, full miniaturization was not the purpose of this project. Instead, the shoe integration thrust of this thesis focused on developing an effective mechanical interface between the pressure exerted by the wearer's foot and the resultant fluid pressure.

As described previously, one deformable fluid bladder will be located under the heel of the foot, and the other under the ball of the foot. While walking, the user will naturally alternate pressure between these reservoirs. The fluid chambers in the shoe must simultaneously and robustly meet several requirements.

First, the bladders must conform to the shoe and the foot. This is important to providing a comfortable walking experience. Shape conformity is also important because it allows the stress of the walker's weight to be distributed more evenly around the foot and around the device.

The bladders and in-shoe plumbing must accept the pressure of walking. In walking use, the full weight of the person may be on one bladder. The bladders should not rupture under this pressure, or under repeated pressurize-depressurize cycles.

The shoe bladders must also accept the static pressure of standing. In this case, the full weight is distributed in some configuration between both shoe bladders.

In a quest for robustness, the fluid bladders must also accept the pressure generated by the user jumping – whether jumping in place, or for example jumping from a vehicle or stair. This will lead to instanteous forces well in excess of the wearer's weight, and almost certainly this will pose the maximum pressure constraint on the design of the bladders.

Finally, the shoe bladders must provide a low-loss connection to the heel and ball fluid reservoirs.

6.1 Original Laminated Design

The original design for a shoe insert consisted of a piece of 0.125" thick transparent acrylic.

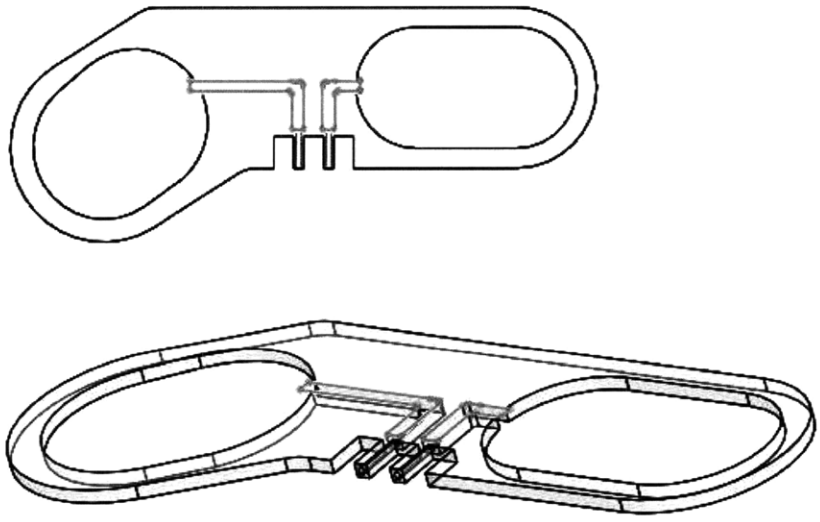

Figure 33. Original laminated shoe insert design

The acrylic was cut in a 2D pattern on a CNC waterjet, yielding a pattern shown in Figure 33. The heel and ball chambers were simply voids in the acrylic. On top and bottom, the acrylic was bonded to rubber cut to the exterior outline of the acrylic. This

was intended to form a deformable but leak-proof seal, and form the chambers themselves in the volume between the rubber layers.

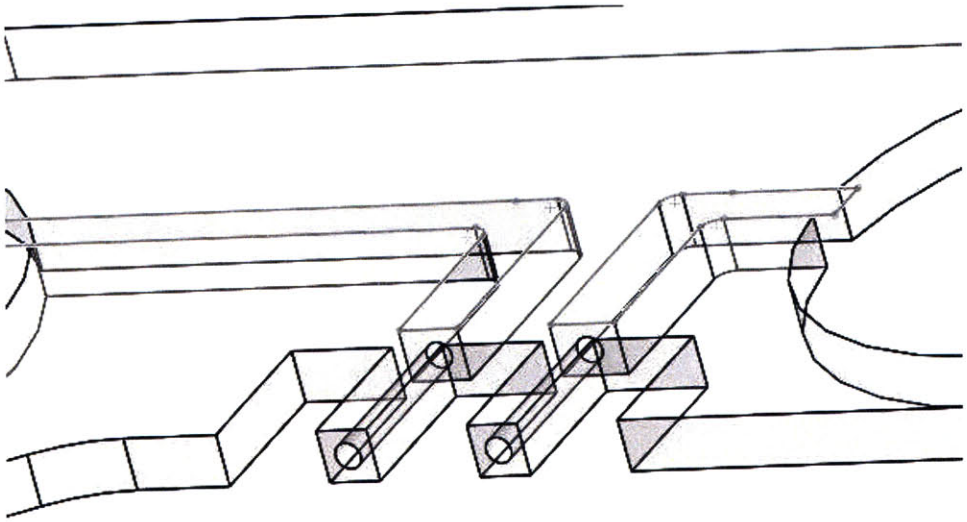

Figure 34. Original laminated shoe insert design, port closeup

In order to connect to the fluid chambers, two small 0.062" (1/16") diameter holes were drilled in the plane of the acrylic, connecting the outside to the chambers, as shown in Figure 34. These ports were then externally bonded to tubing using conventional epoxy. This allowed for the reservoir to make fluid contact outside the sealed rubber chamber.

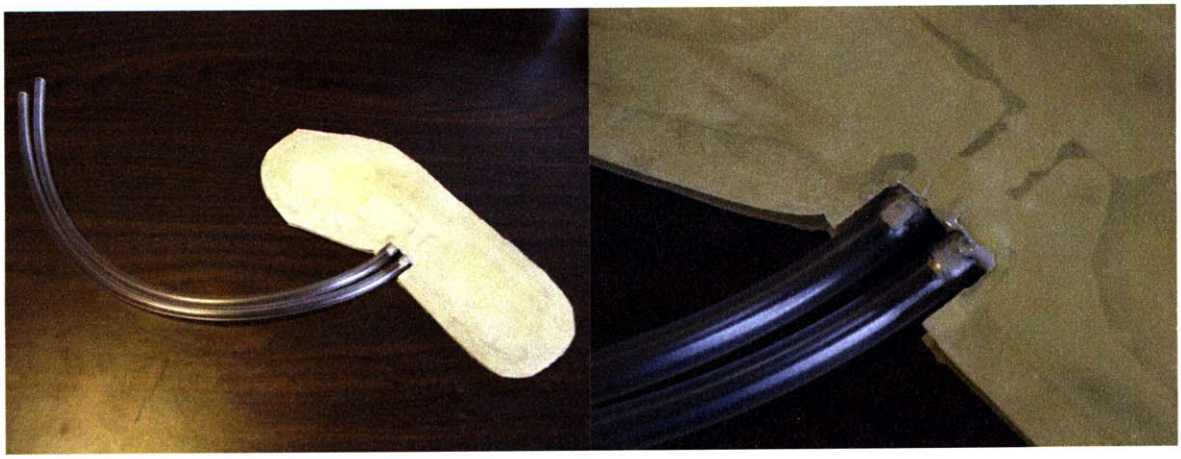

Figure 35. Original laminated shoe insert photos

In general, this laminated design presented several practical issues under testing. First, while it is impossible to quantify, the rigid acrylic piece was extremely uncomfortable to the user. Being flat, it did not conform to the arch of the foot, and therefore was subjected to extraordinary stress under the user's weight. The sharp edges of the waterjet-cut acrylic were dulled very little by the rubber layers, and therefore were almost directly felt by the user.

Additionally, although various adhesives were tested, none were found to have suitable strength to hold under the user's weight while the bladder was filled with air or water. In general, it is believed that this is because this design relies on the peel strength of the adhesive interface, which is typically an adhesive's weakest mode. The fluid-filled chamber pressed the rubber away from the plane of the acrylic, leading to a line of stress where the rubber and acrylic meet. Instead of the full area of the adhesive bearing the shear, only the thin line contact is forced to resist the entire chamber pressure. This led to fast failures, and this design was abandoned.

Another way to make this design might be to have a semi-rigid clamp screwed together around the edge of the rubber, so that static friction and not peel strength is responsible for the integrity of the seal. However, this would still probably present the earlier problem of being uncomfortable to the wearer.

6.2 Rubber Bladder Design

In order to address both the comfort and the pressure integrity concerns of the original design, a second attempt used pre-made rubber bladders, manufactured by Perma-Type

Rubber (Plainville, CT). These are essentially industrial balloons, with standard-size tubes attached.

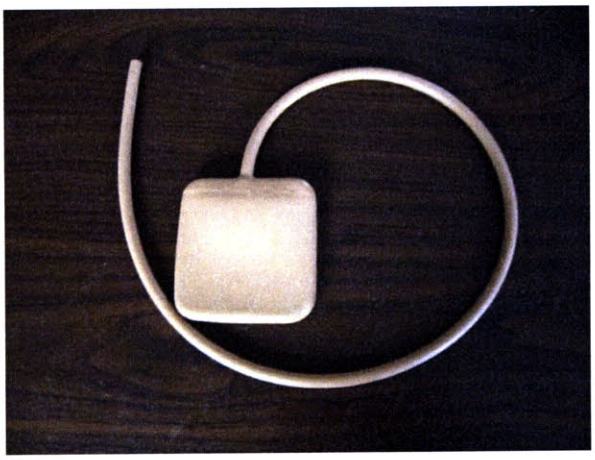

Figure 36. Rubber bladder photo

While little technical data was available, the bladders used had a 3" square uninflated profile, a nominal tube internal diameter of 3/16", a tube length of approximately 23", and a rubber wall thickness of 0.030".

The rubber used in the bladders was explicitly described to me as incompatible with oils, so that another solution or another material would need to be found if an alternative turbine working fluid were to be used.

No pressure rating was available from the technical staff at the company. Under testing, it was found that when pressure was applied unevenly to the surface, the bladder would often deform just as a balloon would, with a weak area expanding rapidly to counter the pressure. Again like a balloon, this localized expansion led to areas that were under much more mechanical stress than others.

Ultimately, with in-shoe testing, the rubber bladders also failed for this reason – pressure

would lead to localized yielding and then failure of the rubber. While it was clear that the bladder as a whole could withstand the pressure, the expansion of local areas swiftly led to failure.

After consultation with the staff at the manufacturer of the bladder, a "pillowcase" was constructed to attempt to constrain the bladder from undesirable, uneven expansion.

6.3 Pillowcase Design

In any balloon, such as the rubber bladders described previously, there will be small variations in the material thickness or local Young's modulus. Additionally, non-spherical shapes, like the rounded-rectangle design of the bladders used here, will mean that stress will tend to concentrate in some areas preferentially instead of others.

Under pressure, this means that weaker or more-stressed areas will deform more in response to the internal fluid pressure (which is constant over the entire internal surface area). This quickly becomes a two-dimensional surface example of the "weakest link in a (one-dimensional) chain" concept, where the first failure of any component part causes the entire structure to fail.

Early testing of the fluid-filled rubber bladders inside a shoe led to broken bladders and fluid-soaked shoes. It was observed that small patches of the rubber bladder (generally near the throat connection to the tube, or near the rounded-rectangle corners) would expand dramatically and in a non-uniform way with the rest of the bladder. Under enough pressure (and body weight was enough), these areas would expand to 1 to 3 cm diameter hemispherical bulges, become visibly very thin, and then rupture.

Figure 37. Rubber bladder with sewn ripstop nylon pillowcase

To counter this, a "pillowcase" of ripstop nylon was sewn around the rubber bladder with ordinary cotton thread. Under normal conditions, the pillowcase bears no stress, whether the bladder is full or empty – it instead sits somewhat loosely around the bladder. However, if the bladder is expanding unevenly as in the modes described above, the weaker part of the bladder will now have to act against the pillowcase. By deforming the pillowcase outward, the material will be forced to pull inward at another part of the bladder, thus transferring the force and ensuring a significantly more even distribution of bladder expansion.

This was found to be a reliable solution to the bladder failure issue. Additionally, the ripstop nylon material provides an extra layer of protection between the rubber bladder and any undesired particulates / sharp objects within the shoe (i.e. sand, small rocks, and other accumulated debris).

7 Fluidic Rectification

One key objective of this project is to study the feasability of using one-way fluidic check-valves, the fluidic equivalent to diodes, for rectifying the alternating pressure from the shoe into a one-polarity DC pressure. This is important for turbine-based designs because it means that the turbine does not have to work bidirectionally (which itself poses significant design constraints). Also, with fluidic rectification, the rotor does not have to stop and restart on every half-step, which means that the operating point can remain close to a maximally-efficient speed.

Various electrical rectifier implementations (Si/Ge diode, LEDs, active op-amp rectifiers, diode-connected FETs) may have different properties (turn-on voltage, steepness of current-voltage relationship, maximum forward current, maximum reverse voltage), and these properties may affect the efficiency of a rectification system. Similarly, these properties will vary for different fluidic check valve implementations, and will affect the efficiency of the system.

Two check valve types were tested for use in this configuration.

7.1 Spring-loaded Ball Check Valve

The first type of check valve tested was a spring-loaded ball check valve (McMaster-Carr part number 7757K41). A spring, made of type 302 stainless steel, presses a small ball, made of type 316 stainless steel, against a flexible seat, made of Buna-N, an elastomer with particularly good chemical resistance to oils. The valve body itself is made of polypropylene. All these properties together would allow for the valve to be used with a satisfactory selection of alternative turbine working fluids.

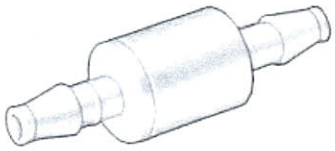

(McMaster-Carr 7757K41)

Figure 38. Spring-loaded ball check valve

As shown in Figure 38, the valve has barbed ends for 1/8" tube connections on either end. With no pressure applied, the spring holds the ball against the valve seat, which completely blocks fluid flow. When the pressure applied on the ball overcomes the extension spring's force, the spring and ball deflect and allow fluid to flow through the valve.

7.2 Elastomeric Duckbill Check Valve

The second type of valve tested is known as a "duckbill" check valve because the active element has two mostly-flat rubber flaps. The elastomeric duckbill is made of silicone, and the valve housing is made of acrylic. These valves are generally designed for medical use, so compatibility with alternative working fluids would require further study.

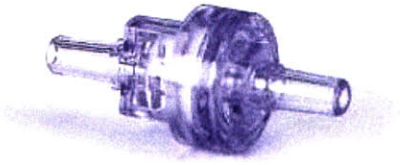

(Vernay Supravalve CVA-02)

Figure 39. Elastomeric duckbill check valve

As shown in Figure 39, this valve has a transparent housing, and in the photo, the forward direction is from right to left. The halves of the acrylic housing are joined to form a pressure-bearing flange around the perimeter of the silicone duckbill to constrain it in place, while the duckbill itself lies in the rectangular region on the left.

When no pressure is applied, the flaps of the duckbill are largely left to their natural position, which may leave some path for fluid flow. When forward pressure is applied, the duckbill flaps separate and the flow path widens. But when reverse pressure is applied, the duckbill flaps are forced together, tightly sealing the flow path.

Also from Figure 39 one can observe that no tube barbs are present to securely hold a tube in place on the inlet or outlet side of the valve. Instead, cyanoacrylate was applied in the annulus to seal the tube to the valve.

7.3 Check Valve Characterization

Just as an electrical diode is characterized by its current vs. voltage relationship, a curve which can be measured experimentally, a flow rate vs. pressure curve can be measured for these check valves.

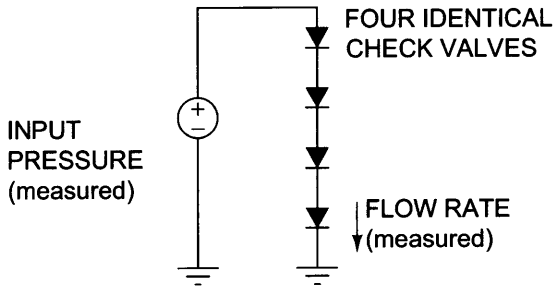

Figure 40. Electrical-equivalent check valve characterization setup

Because only minimal data was available from the vendors / manufacturers of the check valves, they were manually characterized using the constant-pressure test setup used for testing the turbine. Because the pressure drop of each valve should be low, four identical valves were placed in series for the measurements, yielding four times the pressure drop of a single valve, as shown in Figure 40. Since the gauge resolution was only 1psi (6.8kPa), this allowed for substantially better resolution when averaged for a single valve.

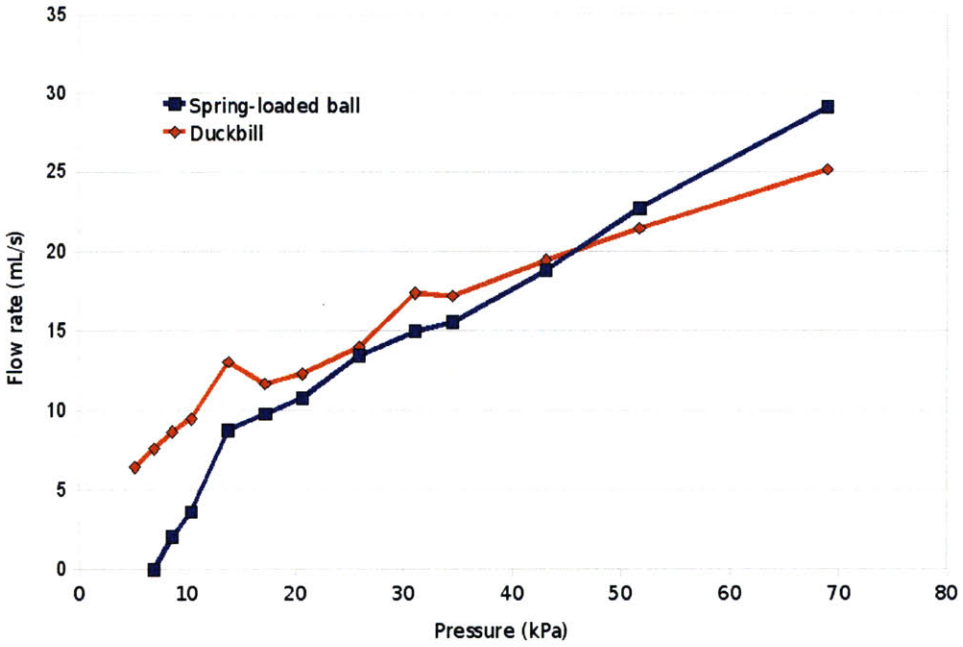

Figure 41. Measured check valve performance

The data shown in Figure 41 is for a single check valve of either type, computed by dividing the measured four-in-series pressure by four. Because of the absence of manufacturer data, this should be a valuable reference for future small-scale fluidic system designers.

As expected, the zero-flow-rate crossing of the duckbill check valve was not measurable with this setup, because the application of any non-zero pressure caused flow. Also as expected, this was not the case with the spring-loaded valve, which required roughly 6.9-8.6 kPa (1.0-1.2 psi) to begin flow. This matches well with the manufacturer data, which claims 1psi "cracking pressure". In comparison, the duckbill's "cracking pressure" is negative.

One unexpected feature of the tests was that for the spring-loaded valve only, at total test pressures of 172-276 kPa (25-40psi), there was an audible buzzing sound emitted from the check valves while the test was in progress. While this phenomenon was not pursued, it is believed that at these higher pressures, less and less headroom is left for the line pressure

regulator to drop. (The voltage source depicted in Figure 40 is actually a line pressure source with a pressure regulator, similar to a linear voltage regulator in the electrical domain.) In that situation, any transient instabilities in the flow or pressure may adversely affect the continuous supply of flow through the regulator, possibly leading to this oscillation. In any case, this was not pursued further for this project, but might be worth evaluating when designing systems at these higher-pressure, higher-flow operating points.

In general, the resistance presented by the valves was surprisingly high. As described in Equation 17, pressure drop losses in a plumbing system can often be characterized as $\Delta P = K(\frac{1}{2}\rho\bar{v}^2)$. Using the average velocity on the basis of a 0.125" tube ID, the duckbill check valve has an average K of about 14.5. Because of the zero flow at non-zero pressure, the K for the spring-loaded check valve can not be calculated in the same way, but using the data over the range of 13.8-69.0 kPa only (2-10 psi), the average K of the spring-loaded ball check valve is about 17.6. These represent significant flow obstacles, where the pressure drop required to navigate the value is K many times the kinetic energy density of the flow. (The kinetic energy density of the flow is essentially equal at the inlet and outlet of the valve, but the pressure drop indicates that this much was removed from the potential energy density of the flow.)

Another way to get a handle on the energy losses in the check valves is to again consider an electrical equivalent. For a diode and its current vs. voltage curve, the product $I * V$ at any point on that curve represents the power dissipation in the diode.

Similarly, for any given point on Figure 41, the product of the pressure drop coordinate and the flow rate coordinate express the power dissipation in the check valve. For example, for the duckbill check valve at 20.7 kPa (3psi) pressure drop, a flow rate of 12.3

mL/s was measured. With unit conversions, the product (20.7×10^3 Pa)($12.3 \frac{\text{mL}}{s}$)($\frac{1m^3}{10^6\,\text{mL}}$) = 0.25 Watts! At our scale, a quarter of a watt represents a tremendous amount of energy being uselessly dissipated in a single valve.

7.4 Full-Wave Bridge Rectifier

The original system design called for a full-wave bridge rectifier.

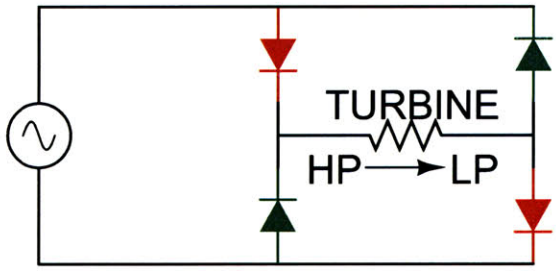

Figure 42. Full-wave bridge rectifier

As shown in Figure 42, four check valves are used. Regardless of the instantaneous polarity of the driving pressure source, the fluid flows through the turbine in only one direction, from the high pressure (HP) inlet side to the low pressure (LP) outlet side. Either the red-colored valves will allow fluid flow, or the green ones, but not both.

The advantage of this system design is that the turbine can be driven essentially 100% of the time, which should help it remain spinning and also allow for more power extraction.

The disadvantage of using a full-wave bridge rectifier is that for flow in either direction, the flow must now pass through the turbine plus two check valves. With the duckbill check valves and a 12.3 $\frac{\text{mL}}{s}$ flow rate described earlier, each check valve will cause 0.25W of power dissipation, for a total of 0.5 Watts.

This is a substantial amount of power dissipation, and during testing, it in fact in proved to be too much to overcome the static friction of the turbine system under walking pressure.

7.5 Other Rectification Alternatives

Because this radial outflow turbine (and most designs) was able to generate power in only one flow direction, other rectification alternatives must be considered if the pressure drop due to two check valves is insurmountable.

7.5.1 No rectification

The radial outflow turbine described in this document will produce a torque only when fluid flows from inside (axially) to outside (tangentially). If fluid is forced to flow in the other direction, it will impart zero net torque to the rotor, because fluid enters and leaves with no angular momentum. Therefore it is indeed possible to run the turbine with the fluid pumped first in the forward direction (which does cause a torque and causes the rotor to accelerate), and second in the reverse direction (which theoretically causes zero torque and therefore no change in the angular momentum of the rotor).

While the return half of the journey will still experience various pressure drops through the turbine and plumbing as the flow is accelerated, decelerated, and turned axially, it will do no useful work. Therefore, the wearer of the shoe turbine will still be exerting effort but not adding to the extractable energy of the system.

Still, the no-rectification setup is the only option if the pressure drop losses due to the available check valves is too great. This proved to be the case in the course of this project, so the results presented later will be with no rectification.

7.5.2 Half-wave rectification

Another alternative strategy which was tested only briefly is to use explicit half-wave rectification.

In a slight departure from the electrical analogy, a single diode in series with the load will not suffice. This is because there is a fixed amount of fluid ("charge") within the circuit, and a return path must be provided.

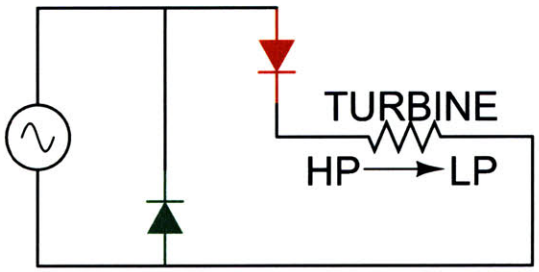

Figure 43. Half-wave bridge rectifier

As shown in Figure 43, this return path is provided by a single check valve which essentially "shorts" the pressure source when pressure is applied in the reverse direction. This allows the fluid to switch chambers but bypasses the "resistance" (and pressure drop) of the load (turbine).

In principle, this means that only one check valve pressure drop is experienced in series with the turbine. However, it has the same disadvantage as the no rectification case, where the turbine is only driven by 50% of the available fluid work. But this may reduce the load on the wearer in comparison to the no rectification case, because the return path will experience little resistance.

Ultimately, this strategy was tested, but the pressure drop due to the single check valve was still too great to allow for sufficient energy to be delivered to the turbine to overcome static friction.

8 Results

This chapter will describe the measured results and associated calculations in characterizing the overall performance of the device.

Because this is a device intended for human interaction, there is a significant degree to which non-repeatability plays a role in the inconsistency of human action. Therefore, the performance of the device is measured in three modes instead of only the walking mode. This gives a more reliable and quantifiable performance metric for comparison with other energy harvesting devices and future energy harvesting devices of this class.

8.1 Turbine Rotor Performance

The first set of performance measurements were performed with only the rotor and turbine, and not the generator. This allowed for estimation of losses due solely to the fluid and mechanical interfaces. This was done with the plastic stator top plate, described earlier, so zero contribution from eddy current losses was possible.

8.1.1 Rotor Nozzle Area Correction Factor

First, the rotor was taken out of the turbine, and was conneted to a constant-pressure water source in a way that allowed fluid flow from inlet to outlet but did not allow for

rotation of the rotor. Because the true "injector area" was known from the machining steps as $2 \cdot (0.040'')^2 = 2.065 \times 10^{-6}\ m^2$, this test was used to determine the "effective injector area" by assuming that the entire pressure drop occured across the nozzle.

Pressure (kPa)	Flow Rate (mL/s)	Effective Area (m^2)	Area Correction Ratio
69	16.3	1.39×10^{-6}	0.67
103	22.6	1.57×10^{-6}	0.76
138	25.8	1.55×10^{-6}	0.75
207	31.1	1.53×10^{-6}	0.74

Table 6. Rotor only, measured results

The data in the left two columns of Table 6 were measured with the setup as described above. The "Effective Area" was calculated from the flow rate and pressure by assuming that out a nozzle transforms pressure potential energy into kinetic energy, leading to a outlet velocity of

$$v_{\text{ideal nozzle}} = \sqrt{2\frac{\Delta P}{\rho}} \tag{68}$$

where ΔP is the pressure across the nozzle, and ρ is the fluid density. Effective area was then calculated as:

$$A_{\text{effective}} = \frac{\dot{V}}{v_{\text{ideal nozzle}}} \tag{69}$$

and the Area Correction Ratio was defined as:

$$\text{ACR} = \frac{A_{\text{effective}}}{A_{\text{mechanical}}} \tag{70}$$

Over the data presented in Table 6, the average ACR ≈ 0.73, for a total effective nozzle

area of $1.51 \times 10^{-6} m^2$.

It should be noted that this contraction in area is typical in any sharp outlet, and is simply a fact from the shape of the fluid flow. The fact that a contraction is occurring is not in itself a source of loss. In fact, this Area Correction Ration is often called a Discharge Coefficient, and for a sharp orifice, it is typically on the order 0.6 to 0.7, so our measurement appears initially consistent [21].

8.1.2 No-load turbine testing

Now, still with the plastic stator top but with the turbine otherwise fully assembled, the rotor performance was measured under no-load conditions by optically measuring the rotor speed through the transparent stator top. For a series of constant-pressure inputs, the flow rate and corresponding no-load rotor speed were measured.

Pressure (kPa)	Flow Rate (mL/s)	Rotor Speed (rpm)
34	11.7	1140
69	16.6	1560
103	21.0	2130
138	25.0	2400
172	26.2	2670
207	30.3	3090
241	31.4	3180
276	35.5	3570
344	39.1	4020

Table 7. Measured no-load turbine testing data

A simple model is applied to estimate turbine losses. Under no load conditions, the torque due to the rotor ejecting fluid tangentially is completely opposed by all torques due

to losses:

$$T_{\text{loss}} = \rho \dot{V} r_2 \left(v_{\text{rel}} - \omega r_2\right) \tag{71}$$

where $v_{\text{rel}} = \frac{\dot{V}}{A_{\text{effective}}}$, the exit velocity relative to the rotating rotor, and r_2 is the radius of the nozzle. Then, the torque losses are modeled with quadratic regression:

$$T_{\text{loss}} = B \cdot \omega + C \cdot \omega^2 \tag{72}$$

where the B component is linear with angular speed, as is likely the case for bearings in the system, and the C component is proportional to the square of angular speed, as is likely the case for any fluid drag components. Regression on the data with these two parameters yields $B = 2.392 \times 10^{-6} \frac{Nm}{(\text{rad}/s)}$ and $C = 5.234 \times 10^{-8} \frac{Nm}{(\text{rad}/s)^2}$, and found a very good fit with a $R^2 = 0.9963$. **The fact that just 2 parameters can be used to strongly fit to 9 datapoints suggests that the quadratic model for loss torques is an excellent match to the actual device behavior.**

Now, considering that with a possible load we could write the steady-state external torque delivered to the generator as:

$$T_{\text{ext}} = \rho \dot{V} r_2 \left(v_{\text{rel}} - \omega r_2\right) - T_{\text{loss}} \tag{73}$$

or as power:

$$P_{\text{ext}} = \omega \rho \dot{V} r_2 \left(v_{\text{rel}} - \omega r_2\right) - B\omega^2 - C\omega^3 \tag{74}$$

With this equation, the curve of expected output power versus operating speed can be

plotted for each pressure level:

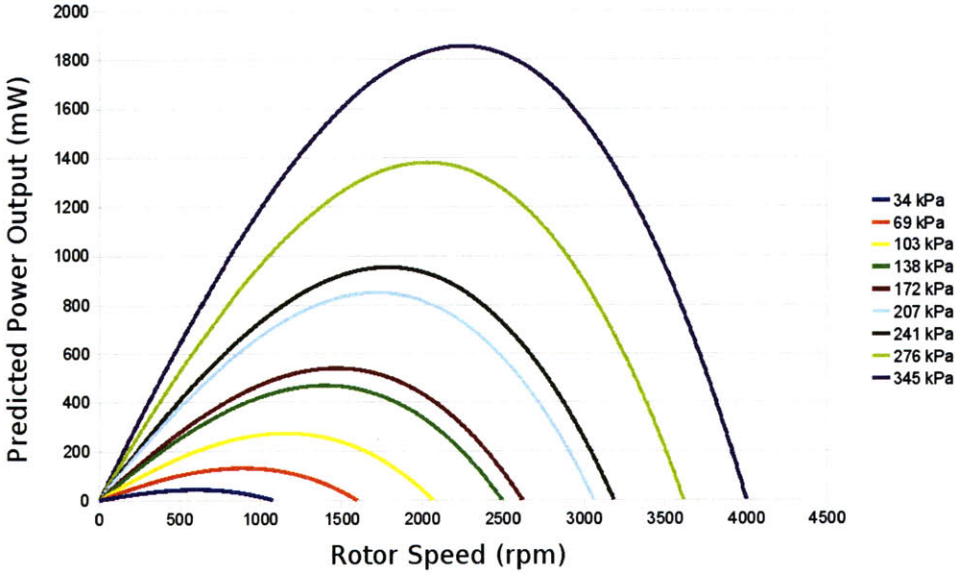

Figure 44. Turbine predicted power curve from no-load loss measurements

The graph in Figure 44 is simply Equation 74 evaluated with the $\dot{V}$ of the turbine measured at that speed, and with the B and C loss model parameters as estimated earlier from the experimental data. Notice that each curve intersects the zero-power-output level at the rotor speed measured in Table 7, showing how the B and C parameters give rise to this behavior under no-load conditions.

It does not include any generator effects, and is simply an estimate of the mechanical power availability. This graph shows that for a given input pressure, this is some optimal turbine speed that allows for maximal power extraction before higher-order losses become detrimental.

We can also evaluate the maximum of each of these curves, and given the measured input power (as a product of pressure and flow rate), we can calculate a estimated peak

mechanical efficiency:

Pressure (kPa)	Best Speed (rpm)	P_{ext} at Best Speed (mW)	Efficiency
34	598	42.5	10.5%
69	892	129.7	11.3%
103	1158	271.6	12.5%
138	1399	467.2	13.6%
172	1470	539.1	12.0%
207	1720	848.3	13.5%
241	1790	951.2	12.5%
276	2033	1377.6	14.1%
345	2251	1854.9	13.8%

Table 8. Turbine predicted maximum mechanical efficiency from no-load loss measurements

The efficiencies shown in Table 8 are only for energy conversion from the potential energy of the fluid flow to kinetic energy extractable as torque. They are based on a model with measured loss parameters. The generator is not included in this model. However, for an ideal lossless generator that could fully convert mechanical torque to electrical power, and with no eddy current losses in a back iron, P_{ext} would represent the electrical power output.

This analysis demonstrates why the no-load speed is a useful figure for characterizing the mechanical efficiency of this type of turbine.

8.2 Constant Pressure Input Results

With the turbine driven from a constant pressure source, we can examine the steady-state performance of the turbine. This is done without any check valves or fluid bladders. The turbine inlet is connected to the adjustable pressure regulator, and the turbine outlet is left free to the atmosphere. The flow rate is measured, and when multiplied by the pressure, gives the overall fluid power input to the turbine.

8.2.1 Raw Data

For each pressure setting, two electrical parameters are measured: RMS voltage, and electrical frequency. The time required for the flow to fill a 500mL calibrated volume was also recorded. These measurements were done twice, first with no electrical load (open circuit), and then with a 33Ω resistor (matched to the measured resistance of the generator windings) as an electrical load on the turbine.

The raw data is presented here:

Pressure (psi)	f_e (Hz)	V_{rms} (V)	500mL fill time (s)
5	0	0	58.8
8	20.9	0.438	41.4
10	44.5	0.995	33.0
15	76.0	1.732	26.1
20	106.3	2.360	22.8
25	149.6	3.392	20.2
30	167.4	3.565	18.7
40	212.0	4.48	16.2
50	253.1	5.39	13.3

Table 9. Measured data, turbine under constant pressure, unloaded ($R_L = \infty$)

Pressure (psi)	f_e (Hz)	V_{rms} (V)	500mL fill time (s)
5	0	0	46.6
8	15.1	0.146	38.3
10	27.5	0.338	31.5
15	55.1	0.630	26.0
20	79.9	0.978	23.3
25	97.5	1.236	20.3
30	124.9	1.493	18.6
40	172.9	2.146	16.0
50	207.1	2.456	13.3

Table 10. Measured data, turbine under constant pressure, loaded ($R_L = 33$ ohms)

For the results in both Tables 9 and 10, instability in the pressure reading was present at the 50psi range, which was near the maximum rating of the pressure regulator, and was

also likely close to the available supply pressure. In this instability, the pressure was observed to vary by approximately ± 5 psi.

At the higher pressure levels, it was definitely possible to feel the 33Ω resistor getting hot due to the electrical power dissipation.

8.2.2 Speed and Power Analysis

The raw measured data shown above in Tables 9 and 10 will now be adapted to provide useful data about the turbine and generator performance.

The electrical frequency can be converted to the mechanical frequency by dividing by the number of magnetic pole pairs, $\frac{N_{\text{magnets}}}{2} = 5$. This lets us use the electrical measurement of frequency to determine the mechanical speed.

Input power P_{in} is simply the fluid power available at the inlet, which is the product of the pressure drop times the flow rate. Output power P_{out} is electrical power. The output RMS voltage can be used along with the load impedance to calculate output power delivered to the load, simply as $\frac{V^2}{R}$.

All other conversions presented are simply unit conversions.

Pressure (kPa)	Rotor Speed (rpm)	Flow Rate (mL/s)	P_{in} (mW)
34.5	0	8.5	293
55.2	251	12.1	666
68.9	534	15.2	1045
103.4	912	19.2	1981
137.9	1276	21.9	3024
172.4	1795	24.8	4267
206.8	2009	26.7	5531
275.8	2544	30.9	8512
344.7	3037	37.6	12960

Table 11. Measured turbine performance under constant pressure, unloaded ($R_L = \infty$)

In the unloaded case, no electrical power is delivered to the load, so no output power is calculated.

Pressure (kPa)	Rotor Speed (rpm)	Flow Rate (mL/s)	P_{in} (mW)	P_{out} (mW)
34.5	0	10.7	370	0.0
55.2	181	13.1	720	0.6
68.9	330	15.9	1094	3.5
103.4	661	19.2	1989	12.0
137.9	959	21.5	2959	29.0
172.4	1170	24.6	4246	46.3
206.8	1499	26.9	5560	67.5
275.8	2075	31.3	8618	139.6
344.7	2485	37.6	12960	182.8

Table 12. Measured turbine performance under constant pressure, loaded ($R_L = 33$ ohms)

As shown in Tables 11 and 12, the rotor does not begin to spin until somewhere between 34.5-55.2 kPa (5-8 psi) is applied. This is because of the torque due to static friction in the various components of the turbine being greater than the torque generated by the change in direction of the fluid passing through the rotor.

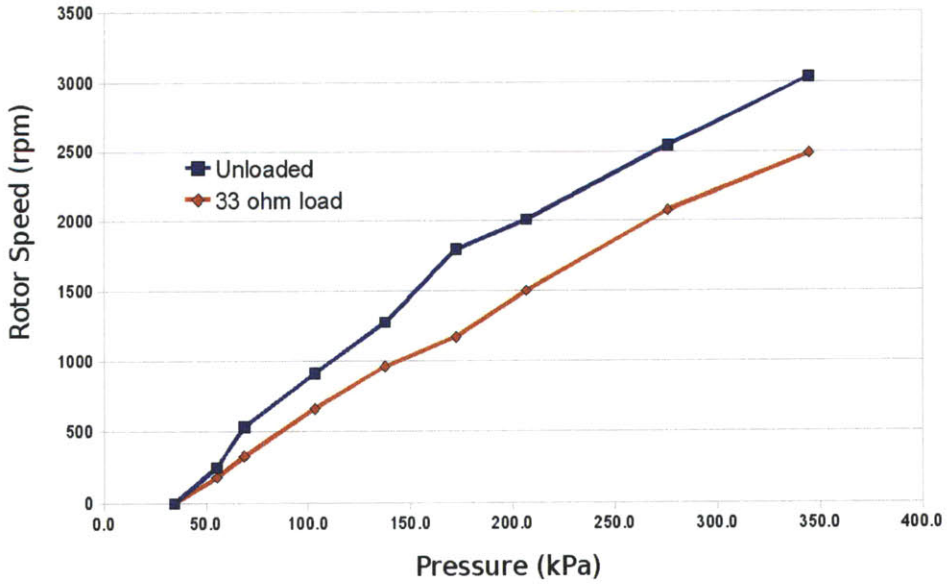

Figure 45. Measured data, turbine under constant pressure, rotor speed vs. pressure

As shown in Figure 45, the mechanical speed of the rotor is a function of the applied pressure. The zero crossing of both curves demonstrates the static friction of the system. It is also important to note that at any given pressure, the speed is lower when the generator is electrically loaded than when it is unloaded. Theoretically, when unloaded, the fluid torque is cancelled only by the friction in the system – an equilibrium which sets the operating speed of the system. But when an electrical load is applied, the fluid torque is cancelled by the sum of the frictional torques plus the torque due to the current running through the generator coils.

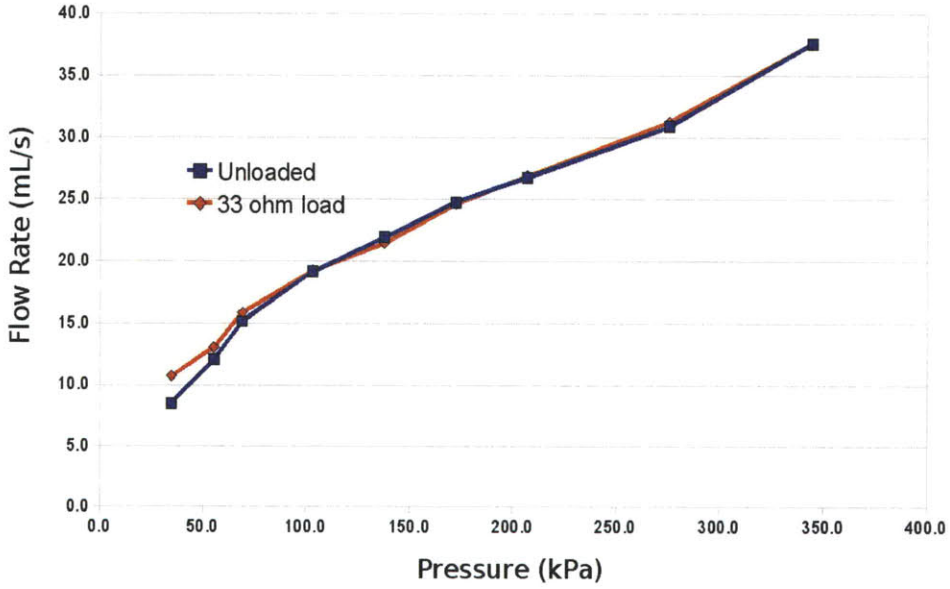

Figure 46. Measured data, turbine under constant pressure, flow rate vs. pressure

Figure 46 demonstrates that the turbine essentially has a single curve for flow rate versus pressure, just as any "one-port" fluidic device should. The presence of an electrical load (and of the corresponding reduced rotational speed) does not appear to have any significant impact on this curve. This validates the earlier turbine modeling assumption that the mass flow rate (and therefore the v_{rel} velocity relative to the rotating nozzle) is unaffected by a change in ω.

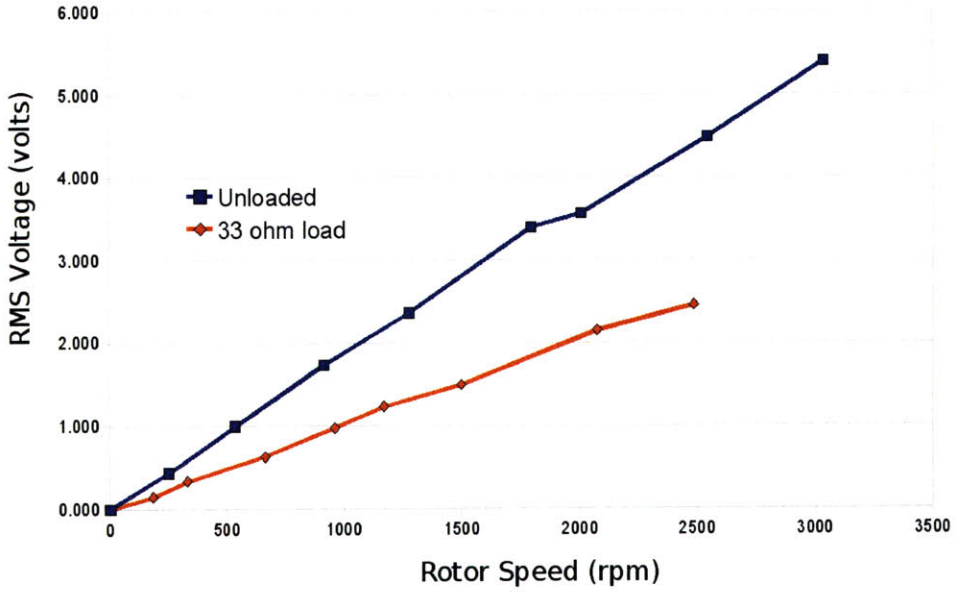

Figure 47. Measured data, turbine under constant pressure, RMS voltage vs. speed

The data purely from the generator side in Figure 47 allows us to estimate the back-EMF constant of the generator, and also the resistance of the coils at that frequency. From the "unloaded" (open-circuit) curve, we can find the slope to be approximately $1.77 \times 10^{-3} \frac{\text{Volts}}{\text{rpm}} \approx 0.0169 \frac{\text{Volts}}{\text{rad/s}}$. This is the back-EMF constant of the generator.

Our back-EMF model calculations in Equation 50 yielded an estimated $K_t = 0.0464 \frac{\text{Volts}}{\text{rad/s}}$, which means that our measured $K_t = 0.0169 \frac{\text{Volts}}{\text{rad/s}}$ is 63% lower than what was predicted. This could have a number of explanations, including weaker than expected magnets, fringing magnetic fields, improper alignment between coils and magnets, shorted coil turns, or other issues.

In contrast to the "unloaded" curve, the "loaded" curve has a slope of approximately $1.01 \times 10^{-3} \frac{\text{Volts}}{\text{rpm}} \approx 0.0096 \frac{\text{Volts}}{\text{rad/s}}$. Assuming the generator output impedance is purely real, and given the known load resistance of 33Ω, the loaded curve should display an output that is approximately $\frac{R_{\text{load}}}{R_G + R_{\text{load}}}$ times as big as the unloaded curve for a given mechanical speed. In this case, this implies $R_G = 24.5\Omega$. This is slightly lower than expected because the DC resistance of the coils, as measured with a voltmeter, is 32.3Ω. While there are some phenomenon that might explain a lower apparent resistance at operating frequency, like a distributed shunt capacitance in parallel with the coil windings (particularly since the coils are submerged in water, which has a high dielectric constant), the source of this effect was not pursued further during this project.

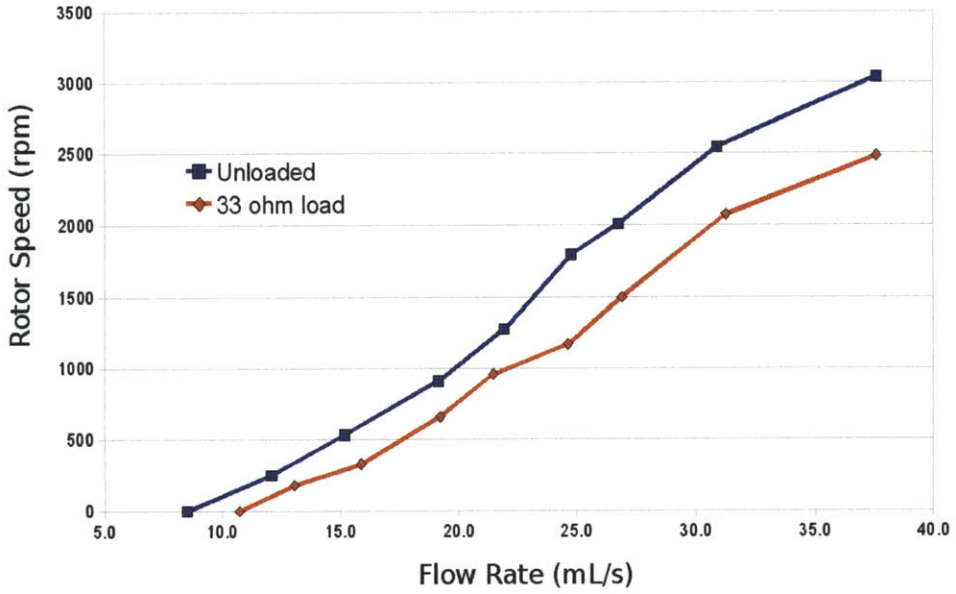

Figure 48. Measured data, turbine under constant pressure, speed versus flow rate

Figure 48 highlights the fact that the rotor speed is related both to the fluid flow rate and the generator load. In a lossless system, or even one where losses are at least proportional to rotor speed and its power series, both curves should theoretically intersect the zero-speed axis at the same flow rate. However, in combination with cogging torque and other sources of non-uniformity that may apply at zero speed, the electrical load may indeed prove to slightly increase the barrier needed for continuous rotation to begin.

8.2.3 Efficiency Analysis

As in any energy harvesting project, efficiency is the key metric of performance. However, in a project like this that is dependent on time-varying human inputs, it is hard to accurately and repeatably characterize the input power into such a system. Instead, the performance from a constant-pressure water source is used to generate efficiency data.

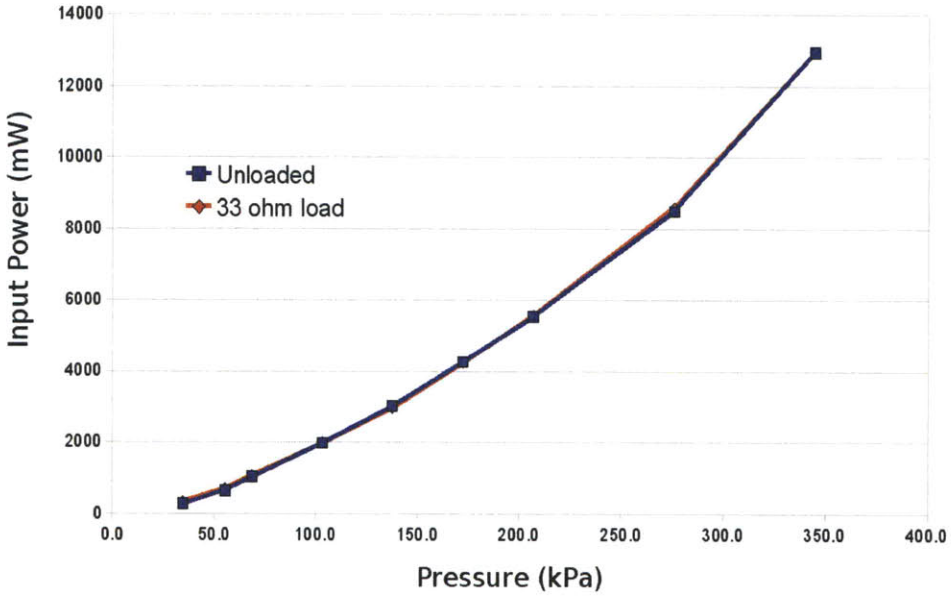

Figure 49. Measured data, turbine under constant pressure, input power versus pressure

As shown in Figure 49, the input power for any given pressure is approximately equal regardless of whether the generator is loaded or not. This is because, as shown before in Figure 46, the flow rate changes little with the load. This input power is a measure of the full work available to a lossless fluidic system – an ideal generator and turbine – as a result of the product of the pressure and flow rate.

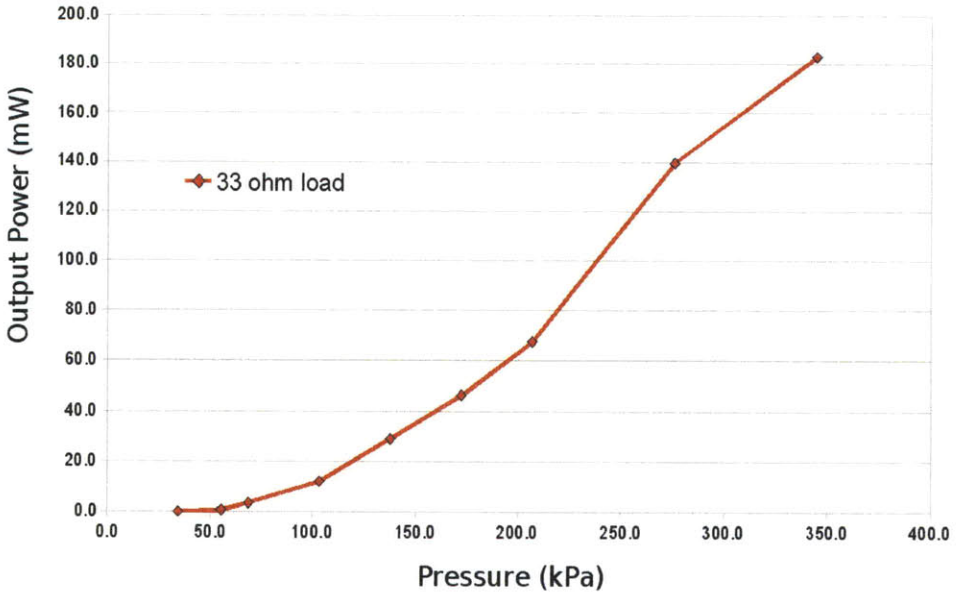

Figure 50. Measured data, turbine under constant pressure, output power versus pressure

The output power of the generator can only be measured under load, and is charted in Figure 50. While the power output does depend on the magnitude of the load itself, the several different resistive loads were tested, and this 33Ω load was found to provide the maximum power output. In any case, the output power results in Figure 50 are promising, showing significant power generation capabilities for a reasonable range of human-generated pressures.

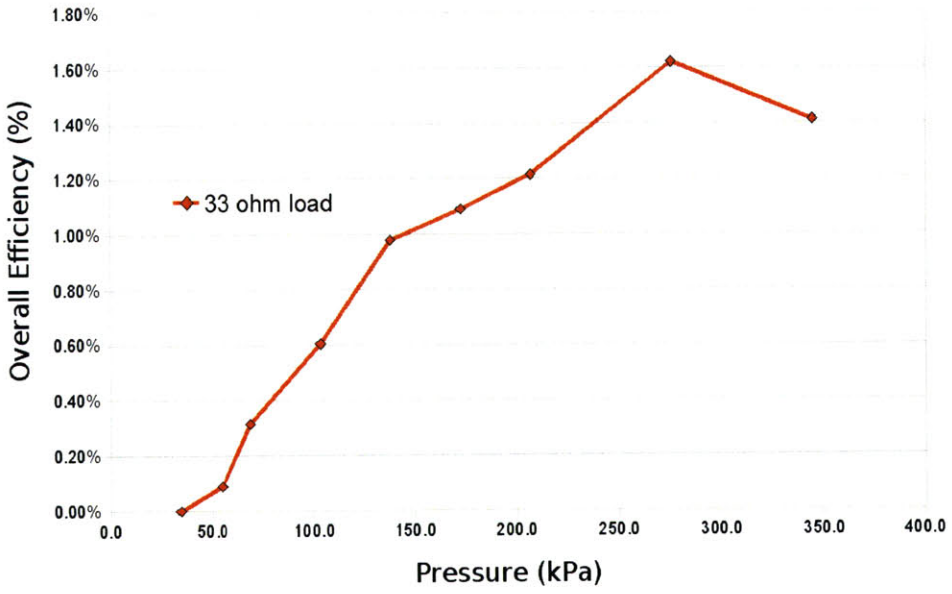

Figure 51. Measured data, turbine under constant pressure, efficiency versus pressure

The efficiency as shown in Figure 51 is calculated simply as the ratio of output electrical power to input fluid power. Therefore, this efficiency includes all stages of the energy

conversion process, from potential energy in the flow, to fluid kinetic energy in the nozzles, to kinetic and potential energy of the spinning turbine rotor, to magnetic field energy, and finally to electrical energy delivered into a low-impedance load. However, because this is constant-pressure data, it does not include losses due to rectification or other losses at the shoe-fluid interface.

In any case, the system demonstrates efficiencies of approximately 0.5% to 1.5% over the range of approximately 100 kPa to 250 kPa. Initially, the efficiency increases with pressure (and input power), as the static losses (like cogging torque and static friction) become less significant. However, the last data point (at the end of our operational pressure test range) indicates that efficiency may begin to diminish at some point, indicating other effects like growing losses due to eddy current losses, or mechanical vibrations leading to increased friction.

In any case, this efficiency curve is the primary metric that should be used to compare against future generations of micro-scale turbines.

8.2.4 Eddy current loss analysis

By comparing the no-load speeds from Table 7, where the plastic stator top was used, to the no-load speeds from Table 11, where the steel top was used, we can determine the influence of eddy current losses.

By repeating the procedure used to generate Figure 44, where the no-load speeds are fit against a quadratic loss model, but this time using the steel top data (except without the 5psi and 8psi readings which demonstrate static friction), we now find a regression fit of

$B = 2.051 \times 10^{-5} \frac{\text{N m}}{(\text{rad/s})}$ and $C = 2.707 \times 10^{-8} \frac{\text{N m}}{(\text{rad/s})^2}$. (The quality of fit is slightly worse: $R^2 = 0.953$.)

While it is confusing that the C parameter dropped by 48% when compared to the plastic stator top case, the fact that the B parameter jumped by a factor of 8.57 makes sense. As expected, the torque due to eddy currents is directly proportional to speed, which is what the B loss parameter represents. While Equation 67 suggests a contribution to B of $1.95 \times 10^{-6} \frac{\text{N m}}{(\text{rad/s})}$, the actual contribution to B appears to be about one order of magnitude larger. It is suspected that this may be due to flux concentration in the steel back iron, and because eddy current losses are known to be proportional to the square of peak flux density, flux concentrations still well below saturation could easily cause a 10x increase in losses over what was calculated earlier.

In any case, given the new B and C quadratic torque loss model parameters, we can re-evaluate the performance of the turbine.

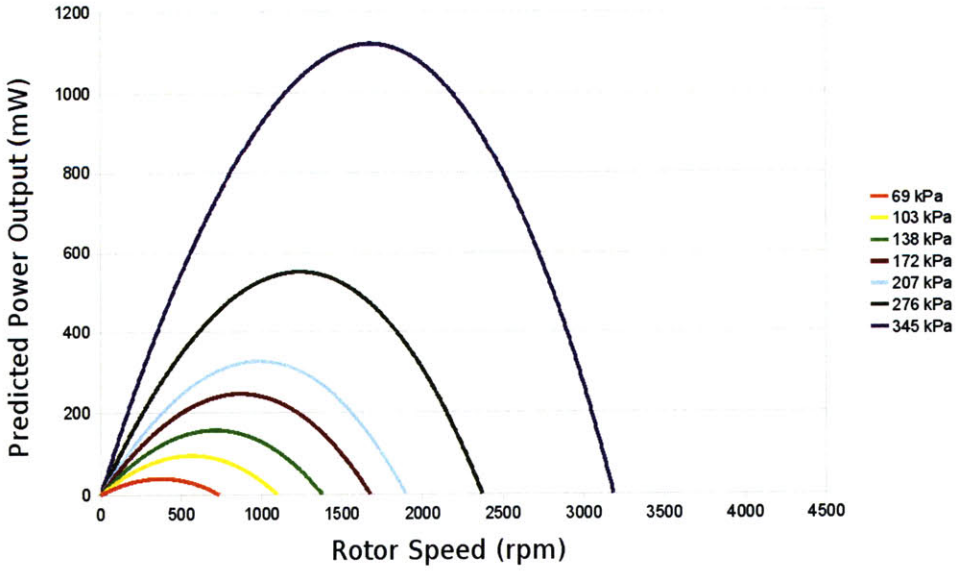

Figure 52. Turbine predicted power curve after eddy current loss measurements

In this case, because the fit is not as strong, the no-load speeds implied by Figure 52 do not exactly fall on the measured locations from Table 11. However, it is still useful to compare Figure 52 with Figure 44, which did not include eddy current effects. Again, Figure 52 does not include any generator effects except for eddy current losses due to the back iron, and only predicts the availability of mechanical shaft power to a perfectly efficient generator.

As before, we can also evaluate the maximum of each of these curves, and given the measured input power (as a product of pressure and flow rate), we can calculate an estimated peak mechanical efficiency:

Pressure (kPa)	Best Speed (rpm)	P_{ext} at Best Speed (mW)	Efficiency
69	375	38.7	3.7%
103	566	94.3	4.8%
138	713	156.5	5.2%
172	872	245.4	5.8%
207	989	326.1	5.9%
276	1242	550.7	6.5%
345	1682	1120.2	8.6%

Table 13. Turbine predicted maximum mechanical efficiency with measured eddy current loss

It is clear from comparing Table 13 to Table 8, which did not account for eddy current losses, that eddy current losses have a dramatic effect on the efficiency of this turbine. While the plastic top no-load measurements predicted peak efficiencies in the range of 10-14%, the steel top no-load measurements are in the 4-6% range. Clearly, reducing the impact of eddy current losses should be a top priority in future work.

8.3 Constant Human Weight Input

After assessing the system performance under constant pressure, the next step toward evaluating its performance in a more realistic use case it to demonstrate it under constant human weight input. A test subject will stand with full weight on the heel of a shoe, inside which the pillowcased rubber bladder has been installed. As long as there is enough fluid in the bladder to ensure that the foot does not directly contact the underlying shoe, the bladder will be under pressure great enough to withstand the weight of the test subject.

This is not a preferred test regime for comparing the performance of different systems because repeatability is difficult. Any shift in weight, plus difficulty of balancing on ones heel (on a fluid-filled bladder!) for an extended period of time, is likely to result in significant variations in measured results. Nonetheless, it is useful because it can address the startup transient as well as the expected pressure under which the system is likely to operate.

With the full weight of the $\sim$ 70kg test subject on the heel bladder, the static pressure (no flow allowed) was measured at approximately 150 kPa (22 psi). This is near the center of the test range of our turbine in the earlier set of constant-pressure tests.

The human-weight-input tests were performed with a full bladder of approximately 100 to 150mL water, and with various resistive loads connected to the generator. An HP 54111D digital sampling oscilloscope was used for its particularly long sample memory, which enabled high-time-resolution capture for the entire waveform. This let us accurately look at both the overall shape plus the detail of the waveform.

8.3.1 19 Ohm Resistive Load

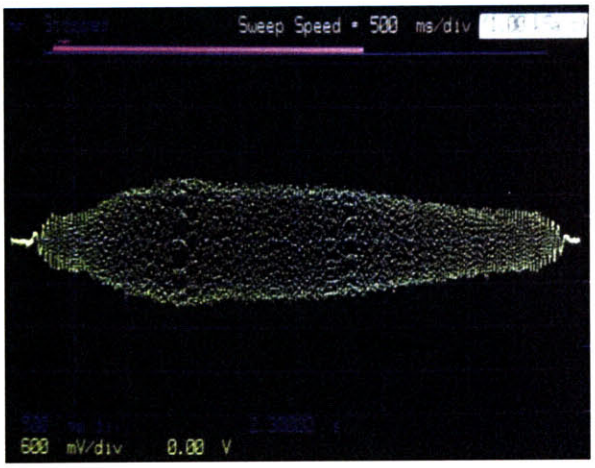

Figure 53. Constant human weight input, 19 ohm load, full capture

The oscilloscope capture shown in Figure 53 is at 500ms/div horizontal and 600mV/div vertical. The entire waveform lasts about 4.5 seconds.

The long duration of this waveform may suggest that the rotor flow channels are too small, or that there is simply too much fluid filling the bladders during these tests.

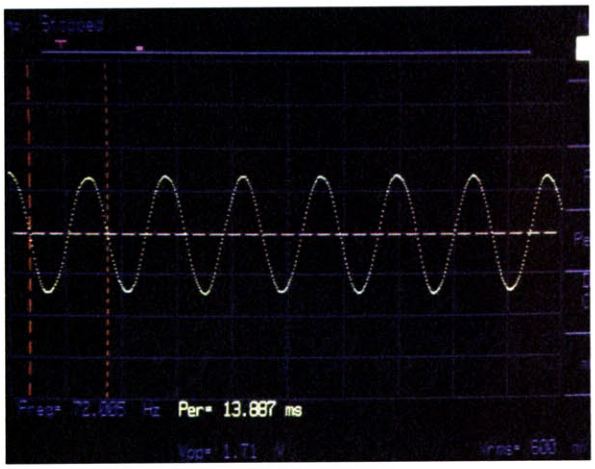

Figure 54. Constant human weight input, 19 ohm load, mid-stream closeup

The close-up shown in Figure 54 was taken from a location in the middle of the Figure 53 wave, and shows the periodic EMF waveform from the generator, at a horizontal scale of 10ms/div. Using the oscilloscope's onboard measurement utility, the signal has an elec-

trical frequency of 72.005 Hz, and a RMS voltage of 600mV. This electrical frequency corresponds to a **864 rpm** mechanical rotor speed. Into the resistive 19Ω load, this represents a power of **18.9 mW**.

8.3.2 33 Ohm Resistive Load

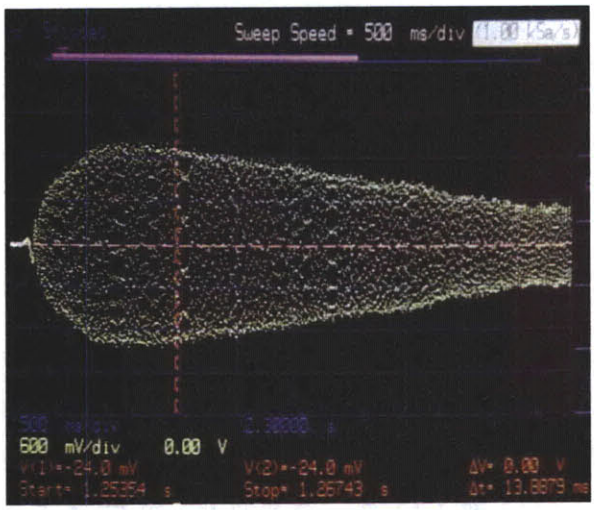

Figure 55. Constant human weight input, 33 ohm load, full capture

Now with a larger resistance load (this time matched to the measured 32.3 ohm generator winding resistance), Figure 55 uses the same 500ms/div horizontal and 600mV/div vertical scale as Figure 53. Again, the signal lasts about 5 seconds, although this may vary due to how much the bladder was pre-filled before the test.

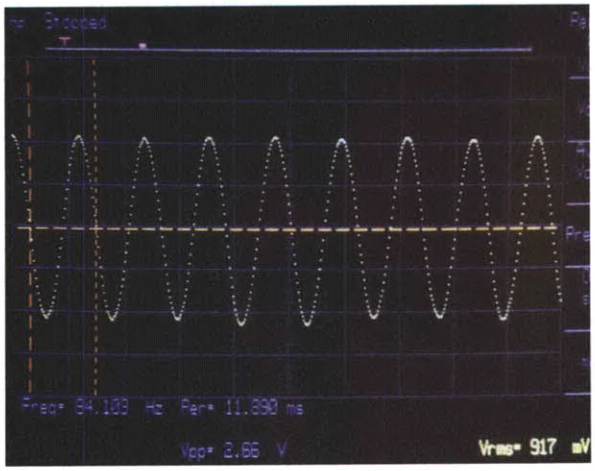

Figure 56. Constant human weight input, 33 ohm load, mid-stream closeup

Figure 56 is a zoomed section of Figure 55, with horizontal scale 10ms/div. Again using the measurement utility, the electrical frequency is 84.103 Hz, and the RMS voltage is 917mV. This electrical frequency corresponds to a **1009 rpm** mechanical rotor speed. Into the resistive 33Ω load, this represents a power of **25.5 mW**.

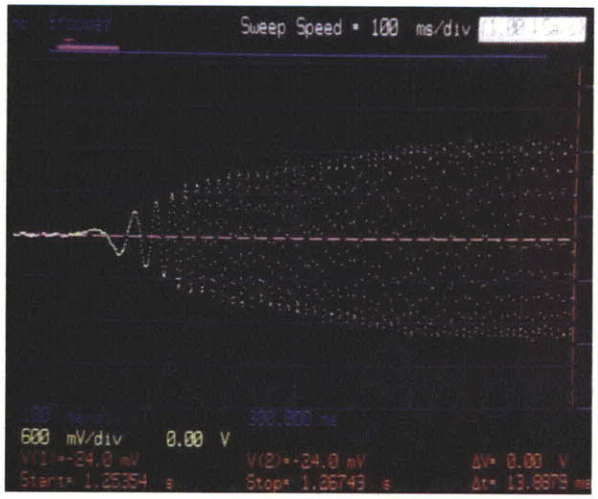

Figure 57. Constant human weight input, 33 ohm load, initial rise closeup

The human weight test also provides an opportunity to examine the system transients in a way that the constant pressure turbine/generator testing did not. Figure 57 shows a zoomed section of Figure 55, specifically the initial starting transient with horizontal scale 100ms/div. It is clearly possible to see that the turbine gains energy growing to its maximum speed with a time constant very roughly on the order 200ms. This shows that the turbine is effectively storing energy in the form of angular momentum.

8.3.3 47 Ohm Resistive Load

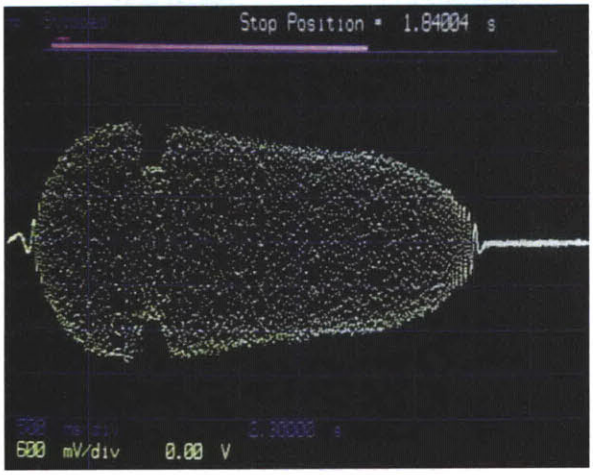

Figure 58. Constant human weight input, 47 ohm load, full capture

As before, Figure 58 shows the full capture with a higher resistive load, again with the same 500ms/div horizontal and 600mV/div vertical scale as Figures 53 and 55. This time, the entire signal appears to last only about 4 seconds. There is also a transient dip in the measured voltage at around 2.5 seconds, which reflects the typical problems experienced with trying to stay balanced on the bladder for an extended period of time.

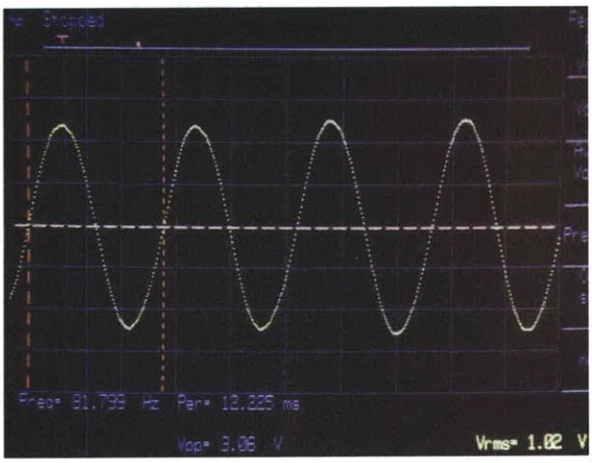

Figure 59. Constant human weight input, 47 ohm load, mid-stream closeup

The close-up in Figure 59 shows an electrical frequency of 81.799 Hz and an RMS voltage of 1.02 volts. This electrical frequency corresponds to a **982 rpm** mechanical rotor speed. Into a resistive 47Ω load, this represents a power of **22.1 mW**.

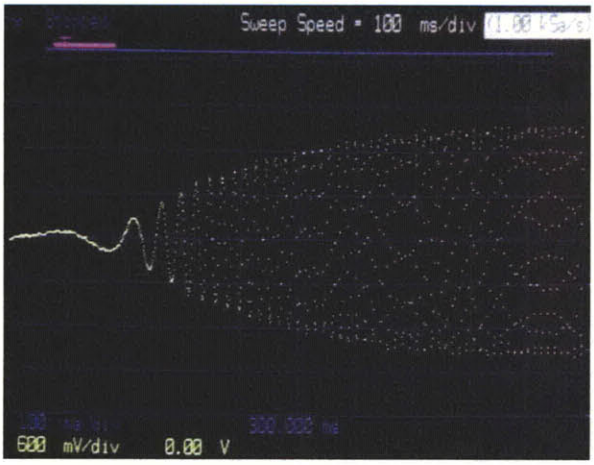

Figure 60. Constant human weight input, 47 ohm load, initial rise closeup

The initial rise transient is examined again in Figure 60. While the overall voltage is higher here than in Figure 57 (due to the higher load resistance), this again suggests a time constant on the order of $\sim$200ms.

8.3.4 Summary

Load	Rotor Speed (rpm)	RMS Voltage (Volts)	Output Power (mW)
19Ω	864	0.600	18.9
33Ω	1009	0.917	25.5
47Ω	982	1.020	22.1

Table 14. Constant human weight input measurements, summary of results

The results from the above tests are summarized in Table 14. However, it should be noted that all measurements were taken at arbitrary mid-waveform locations, and as can be seen from Figures 53, 55, and 58, the signal can vary greatly during the waveform. Additionally, there was variability to the fluid fill level and the standing balance/coordination of the test subject.

8.4 Walking Step Input

The final set of tests to characterize the device is to test the device in-shoe while walking,

as it would be used in its intended application. As with the constant human weight input, there is significant variability due to posture and balance and consistency, but to an even larger degree in this case because of the dynamic motion required. Stride length and step frequency are among the many factors that will influence the power output results.

As before, it was not possible to use the fluidic rectification for these tests, because the losses in the check valves were too great to allow the turbine to spin at all. Therefore, there was insufficient time for inertia to build up in the rotor to keep the system spinning during the entire walk cycle.

In order to explore the effect of varying walking paces on the device, three different walking speeds were tested: 0.4Hz, 0.6Hz, and 0.9Hz. This is for a full cycle of walking: 0.4Hz indicates that the left and right feet *both* take a step within a 2.5s period. The walking speeds are approximate and are estimated from the actual data.

8.4.1 Slow walking pace (0.4 Hz)

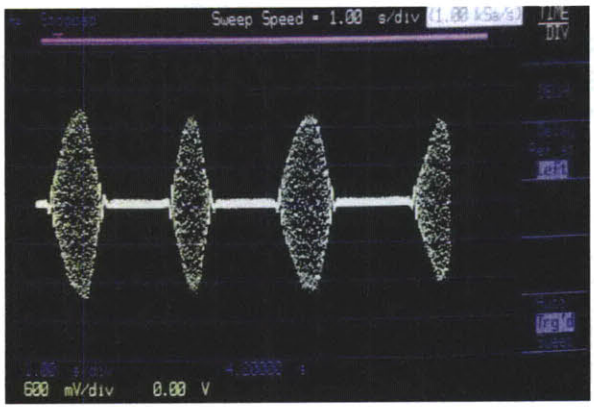

Figure 61. Walking turbine output, slow pace, full capture

As shown in Figure 61, the slow-pace walk generator output captured three and a half heel strike events in the approximately 8-second capture window.

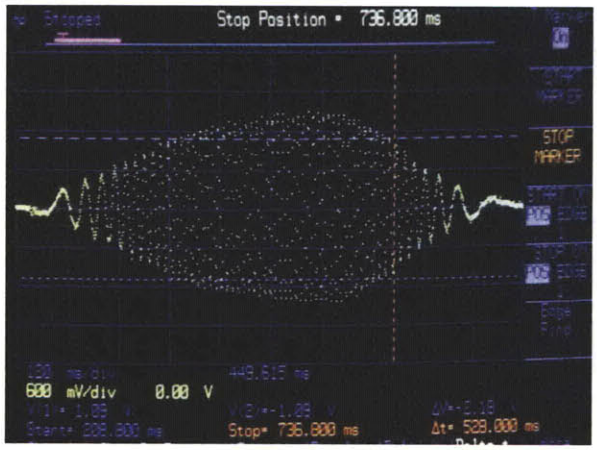

Figure 62. Walking turbine output, slow pace, step #1

Using the 8192-sample memory of the oscilloscope, the generator output of each individual step was examined under zoom, as shown in Figure 62. In order to make a simple estimate of the electrical energy delivered to the 33Ω electrical load, a rectangular voltage-time window was established. As shown in the figure, the horizontal voltage markers were set to $\pm\,1.09$ volts (2.18 volts peak-peak), and the vertical time markers were then set to locations where the envelope of the generator output intersected the horizontal voltage lines, in this case with a $\Delta t = 0.528$ seconds.

Therefore, a conservative lower bound for the energy delivered during this step is to assume that the signal is sinusoidal at exactly 2.18 volts peak-to-peak for 0.528 seconds, and zero elsewhere. This yields an energy of $\frac{V_{\text{rms}}^2}{R_L}(\Delta t) = \frac{(2.18/2/\sqrt{2})^2}{33}(0.528) = 9.50\,\text{mJ}$.

This process was repeated for each step to compile the following table:

Step #	Start (s)	End (s)	Threshold (Volts)	Time Above (s)	Energy (mJ)
1	-0.06	1.02	± 1.09	0.528	9.50
2	2.28	3.10	"	0.352	6.34
3	4.40	5.52	"	0.485	8.73
4	7.10	n/a	n/a	n/a	n/a

Table 15. Walking turbine output, slow pace, energy lower bound

The total energy captured in these three steps is 24.57mJ, at an average pace of $\frac{(7.10 - -0.06)}{3} = 2.39$ seconds (0.42 Hz). The lower bound for walking cycle average power is then $\frac{24.57\text{mJ}}{2.39s \times 3} = 3.43\text{mW}$.

8.4.2 Medium walking pace (0.6 Hz)

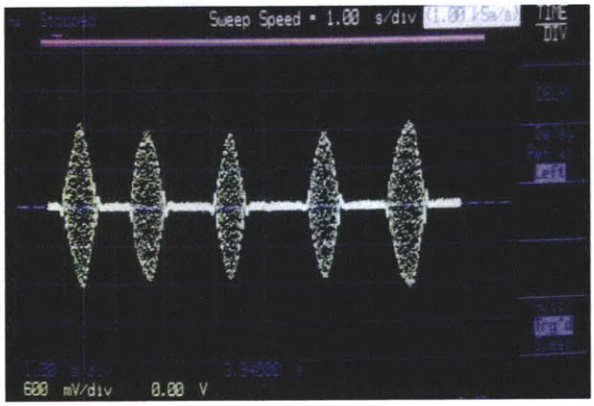

Figure 63. Walking turbine output, medium pace, full capture

At a slightly faster walking pace, five steps were captured as shown in Figure 63. The lower bound for the step-by-step energy was approximated as before:

Step #	Start (s)	End (s)	Threshold (Volts)	Time Above (s)	Energy (mJ)
1	-0.06	0.58	± 0.90	0.285	3.50
2	1.26	1.94	"	0.358	4.39
3	2.96	3.56	"	0.264	3.24
4	4.84	5.42	"	0.269	3.30
5	6.36	7.14	"	0.406	4.98

Table 16. Walking turbine output, medium pace, energy lower bound

This capture yielded a total energy of 19.41 mJ, at an average pace of $\frac{(6.36 - -0.06)}{4} = 1.61$ seconds (0.62 Hz), for an average power lower bound of $\frac{19.41\,\text{mJ}}{1.61s \times 5} = 2.41\text{mW}$.

8.4.3 Fast walking pace (0.9 Hz)

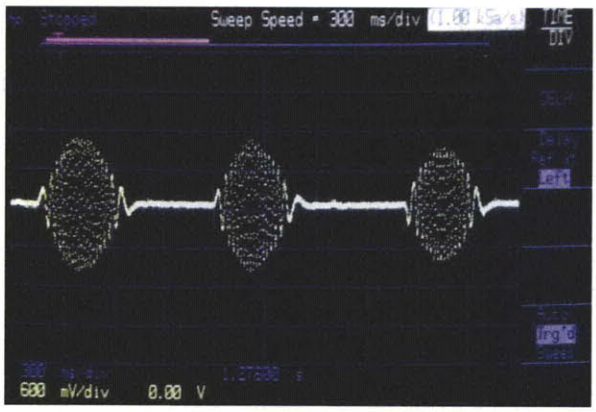

Figure 64. Walking turbine output, fast pace, full capture

The procedure was repeated again for an even faster pace, and this time three steps were captured as shown in Figure 64. (Note that the horizontal scale is now 300ms/div, not 1s/div.)

Step-by-step power lower bounds were calculated via the same metric, yielding the following results:

Step #	Start (s)	End (s)	Threshold (Volts)	Time Above (s)	Energy (mJ)
1	-0.06	0.53	± 0.72	0.300	2.36
2	0.98	1.52	"	0.248	1.95
3	2.09	2.63	"	0.222	1.74

Table 17. Walking turbine output, fast pace, energy lower bound

The total energy capture is 6.05 mJ, at an average pace of 1.08 seconds (0.93 Hz), for an average delivered power lower bound of 1.87mW.

8.4.4 Trapezoidal Voltage Model

While the lower-bound rectangular technique shown in Figure 62 gives clear energy measurements that are easy to compute and see visually from the recorded voltage waveforms, they significantly underestimate the actual power delivered, because they both underestimate the magnitude and duration of the voltage input.

To compute a more accurate power measurement, the zoomed step waveform (as in Figure 62) for each step was measured for its envelope peak-to-peak voltage at each horizontal division. This was used to create a trapezoidal approximation to the voltage envelope.

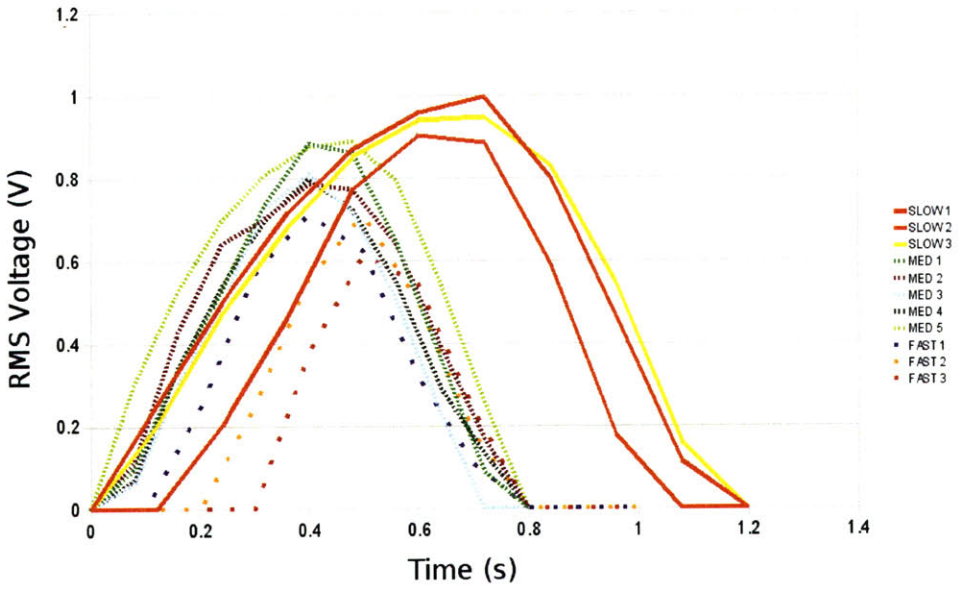

Figure 65. Walking turbine output, trapezoidal RMS voltage model for each step

This trapezoidal voltage model, as shown in Figure 65, was used to provide a much better approximation to the electrical power delivered for each step. After the measurements are taken, the total energy delivered for each trapezoidal segment is calculated:

$$E_{\text{segment}} = \int \frac{V^2_{\text{envelope, rms}}(t)}{R_L}\,\text{dt} \tag{75}$$

$$E_{\text{segment}} \approx \frac{1}{R_L}\left(\frac{y_0^2 + y_0 y_1 + y_1^2}{3}\right)\Delta t \tag{76}$$

where y_0 and y_1 are the RMS voltage at the start and end of each segment. These segment energies are then summed for each step to yield a total trapezoidal estimated energy for that step.

Pace	Step #	"Rectangular" Lower Bound (mJ)	Trapezoidal Estimate (mJ)
Slow	1	9.50	15.59
Slow	2	6.34	10.01
Slow	3	8.73	15.16
Medium	1	3.50	7.18
Medium	2	4.39	6.93
Medium	3	3.24	5.56
Medium	4	3.30	5.86
Medium	5	4.98	9.69
Fast	1	2.36	4.04
Fast	2	1.95	3.33
Fast	3	1.74	2.47

Table 18. Walking turbine output, energy output per step

This new trapezoidal voltage model estimate is much closer to the actual energy delivered for each step, because it takes into account the shape of the step waveform.

8.4.5 Summary

Using the new estimates of the energy output for each step, the average power delivered while walking at various speeds can be calculated more accurately:

Walking Pace	Walking Pace (Hz)	Average Electrical Power Delivered (mW)
Slow	0.42	5.7
Medium	0.62	4.4
Fast	0.93	3.1

Table 19. Final single-shoe walk-cycle-averaged power delivery

The results are tabulated in Table 19, which shows the average electrical output power delivered to a load, using the average energy delivered over the recorded steps. The final single-shoe electrical power output of the system is approximately 3.1 to 5.7 mW, varying with walking pace.

9 Conclusions and Recommendations

This thesis demonstrated the design of a wearable-scale radial outflow turbine integrated with an axial-flux electromagnetic generator, and ultimately delivered 3.1 to 5.7 mW of electrical power to a resistive load at low electrical impedance when walking at various normal speeds.

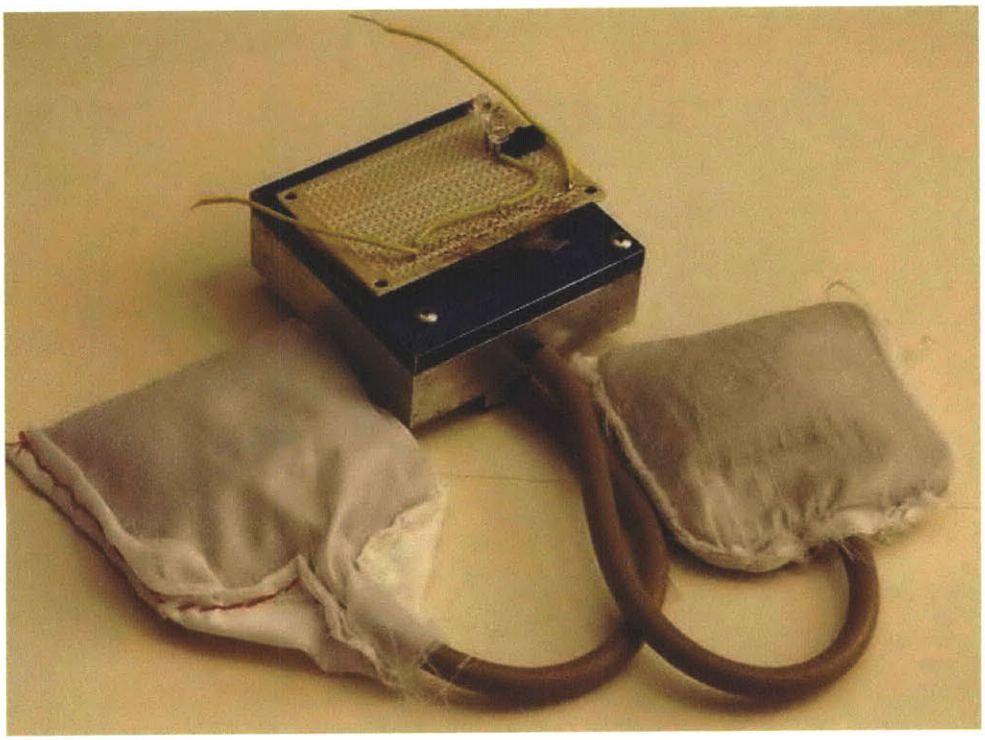

Figure 66. Full energy harvesting system, outside of the shoe

The design and fabrication process included several novel features, including a functioning

hydraulic turbine built at a scale far smaller than previously described in the literature, reliable shoe bladders capable of comfortably and reliably conveying pressurized fluid to and from the shoe, integration of the electromagnetic generator within the turbine itself, and pursuit of fluidic rectification strategies to allow for continuous operation.

Some aspects of the project were not as successful as desired. In particular, the unacceptably high pressure drop due to the check valves tested forced the fluidic rectification strategy to be abandoned for this project.

Figure 67. Full energy harvesting system, mounted in and on the shoe

9.1 Comparison to Calculations and Loss Analysis

In order to get a sense for the magnitude of various losses in the system, we can look at

one operating point and examine the energy balance of the turbine and generator system. At an operating pressure of 207kPa (30psi), the loaded turbine was found to run at 1499rpm, and delivered 67.5mW into a resistive load (see Table 12). The input fluidic power is 5560mW. Some sources of loss, based on earlier calculations, include 67mW in the resistance of the generator coils, 505mW in eddy current losses and other torques proportional to ω, 105 mW in viscous drag losses and other torques proportional to ω^2, and most importantly, 4531 mW in energy still left in the output kinetic energy stream. Within about 5% (rounding and modeling error), the delivered output plus all these losses equals the fluidic input power. The reason that a significant amount of energy is left in the output kinetic energy stream is that the rotor is spinning so slowly, although as explained in the discussion of turbines without guide vanes, the very best we can do with this design still would theoretically leave 50% of the input energy in the kinetic energy output stream. This kinetic energy in the output stream is not captured and is simply dissipated in viscous interactions within the stator body.

The performance of the various system components diverged from the modeled performance at several points, and these divergences cascade into substantially lower overall performance. A particular concern is that since the power output of the generator is proportional to ω^2, the reduced-speed operating point significantly affected and limited the power output of the system compared to what was expected from the model. At the operating point discussed above, the generator is extracting 135mW of mechanical power (half of which is immediately dissipated resistively within the generator itself). In order to compensate, a generator with higher $\frac{K_t^2}{R}$ should be pursued to allow for sufficient power output at lower speeds.

9.2 Comparison to Other Implementations

Other implementations of shoe-based energy harvesting currently have been shown to generate significantly higher power levels than the device described in this thesis. At low electrical impedances, the highest demonstrated power has been about 93mW while walking via a piezoelectric-based system [7], or 1.2 W while walking via a turbine-based system [19]. At high electrical impedances (on the order of 10^6 ohms), powers of 600-800mW have been reported [1] [9], but the efficiency in converting this pulsed, high-voltage, low-current power to a range useful to digital and analog devices has been poor [15].

While others suggest the possibility of high power density on the order of 1 W/g from resonant piezoelectric systems [4], these are modeled and not demonstrated results, and such an implementation relies on passive or active check valves operating at extremely high frequencies (necessitating small openings), which would almost certainly be a tremendous source of energy loss. (In addition, it should be noted that the same designers with the the 1W/g calculation in 1999 were responsible for the 93mW in 455g working prototype in 2009, reflecting the enormous difficulties of implementing these kinds of energy harvesting systems.)

9.3 Suggestions for Future Study

The results of this thesis suggest several areas of study which would yield rapid and significant improvements in the performance of this device.

First, the problem of fluidic rectification should be addressed, and a check valve capable of low-loss operation should be designed or selected. This thesis work attempted to use off-the-shelf check valves to ease manufacturability, but the actual check valve requirements

here differ from the requirements of typical check valve users. In particular, reverse leakage at near-zero pressure is not a concern, and the operating frequency is not particularly high. Implementation of low-loss fluidic rectification would immediately double the working duty cycle of the device and therefore the output power, and would ideally also allow the device to continue spinning continuously, which would reduce the losses due to static friction.

Next, a second-generation turbine design should be constructed, particularly with stator guide vanes (like the Fourneyron or Francis design) to eliminate the problem of substantial kinetic energy remaining in the turbine outlet flow. This would add complexity to the manufacturing of the device, but it would still allow for a compact, radial flow, largely 2D structure. Additionally, the flow area could be scaled up to allow for greater flow rates and therefore more power output since it took several seconds for the fluid bladders to discharge fully in this implementation.

Finally, the generator design should be modified to allow for higher power output. Two relatively straightforward steps in this direction would be first to add a low conductivity ferrite plate as a back iron material, which would substantially reduce eddy current losses, and next to add a second set of magnets and coils on the bottom side of the rotor, immediately doubling the available power for a given rotor speed. This would also reduce the axial load on the ball bearing due to magnetic attraction, which would reduce friction losses in the bearing and extend the ball bearing lifetime.

With these improvements, it is likely that a turbine-based footstep energy harvesting device will be competitive with or outperform other footstep energy harvesting implementations.

Bibliography

[1] James F. Antaki, Gina E. Bertocci, Elizabeth C. Green, Ahmen Nadeem, Thomas Rintoul, Robert L. Kormos, and Barlet P. Griffith. A Gait-Powered Autologous Battery Charging System for Artificial Organs. *J. American Society for Artificial Internal Organs*, 41(3), 1995.

[2] E Cravalho, J Smith Jr, J Brisson II, and G McKinley. *Thermal-Fluids Engineering: 2.006 Course Notes*. MIT, Spring 2006.

[3] J. M. Donelan, Q. Li, V. Naing, J. A. Hoffer, D. J. Weber, and A. D. Kuo. Biomechanical Energy Harvesting: Generating Electricity During Walking with Minimal User Effort. *Science*, 319(5864), 2008.

[4] N Hagood et al. Development of Micro-Hydraulic Transducer Technology. In *Proc. 10th Int"l Conf. Adaptive Structures and Technologies*, 1999.

[5] Schaeffler Group. FAG Roller Bearing Technical Information, 1999. http://www.fag.com/mediaDB/rel%20PubLanguage/114061/PubFile/-/-/-/schaeffler_internet/TI_WL_43-1190_de_en.

[6] Jeffrey Yukio Hayashida. Unobtrusive Integration of Magnetic Generation Systems into Common Footwear, 2000.

[7] C A Howells. Piezoelectric energy harvesting. *Energy Conversion and Management*, In Press, Corrected Proof, 2009.

[8] Robert Komarechka. US Patent 6,239,501: Footwear with Hydroelectric Generator Assembly, 2001.

[9] Roy Kornbluh, Ron Pelrine, Qibing Pei, Richard Heydt, Scott Stanford, Seajin Oh, and Joe Eckerle. Electroelastomers: Applications of Dielectric Elastomer Transducers for Actuation, Generation, and Smart Structures. *Proceedings of SPIE*, 4698, 2002.

[10] J P Marsden and S R Montgomery. Plantar power for arm prosthesis using body weight

transfer. In *in Human Locomotor Engineering, Inst. of Mechanical Engineers*, pages 277–282, 1971.

[11] R D McLeish and J F D Marsh. Hydraulic power from the heel. In *in Human Locomotor Engineering, Inst. of Mechanical Engineers*, pages 126–132, 1971.

[12] E Oberg, F D Jones, H L Horton, and H H Ryffel. *Machinery's Handbook*. Industrial Press Inc, 26th edition, 2000.

[13] U.S. Department of Defense. Wearable Power Prize Rules. http://www.dod.mil/ddre/prize/topic_wp_rules.html.

[14] Lawrence C. Rome, Louis Flynn, Evan M. Goldman, and Taeseung D. Yoo. Generating Electricity While Walking with Loads. *Science*, 309(5741):1725–1728, 2005.

[15] Nathan S. Shenck. A Demonstration of Useful Electric Energy Generation from Piezoceramics in a Shoe. Master's thesis, Massachusetts Institute of Technology, 1999.

[16] Martyn R. Shorten. Running Shoe Design: Protection and Performance, 2000. http://www.biomechanica.com/docs/publications/docs/Shortenhoe.pdf.

[17] Thad Starner and Joseph A. Paradiso. Human Generated Power for Mobile Electronics, 2004. http://www.media.mit.edu/resenv/pubs/books/Starner-Paradiso-CRC.1.452.pdf.

[18] Y Toriumi, Y T Kanai, M Akira, and H M Takashi. Japanese Patent 2008-208766: Build a Power Plant Rotating Mechanism (in Japanese), 2008.

[19] Y Toriumi, S Matsumoto, and T Shodai. Performance of a New Walking-Power Generator Using a Turbine. *The 2008 IEICE General Conference*, 2008.

[20] P J Weisbach. *A Manual of the Mechanics of Engineering and of the Construction of Machines*. Wiley and Sons, 1878.

[21] Frank M. White. *Fluid Mechanics*. McGraw-Hill, fifth edition, 2003.

10 Appendix A: Mechanical Drawings

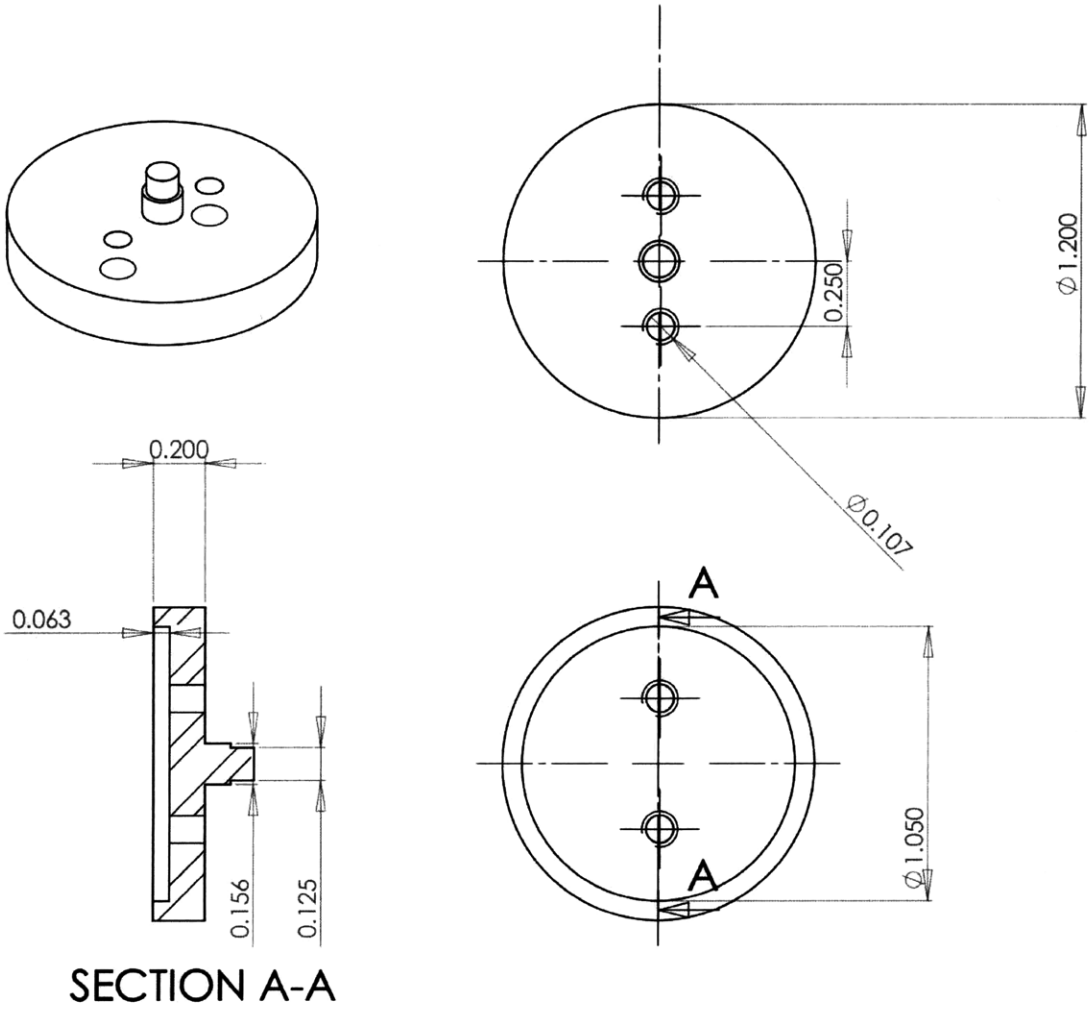

Figure 68. Rotor top piece drawing

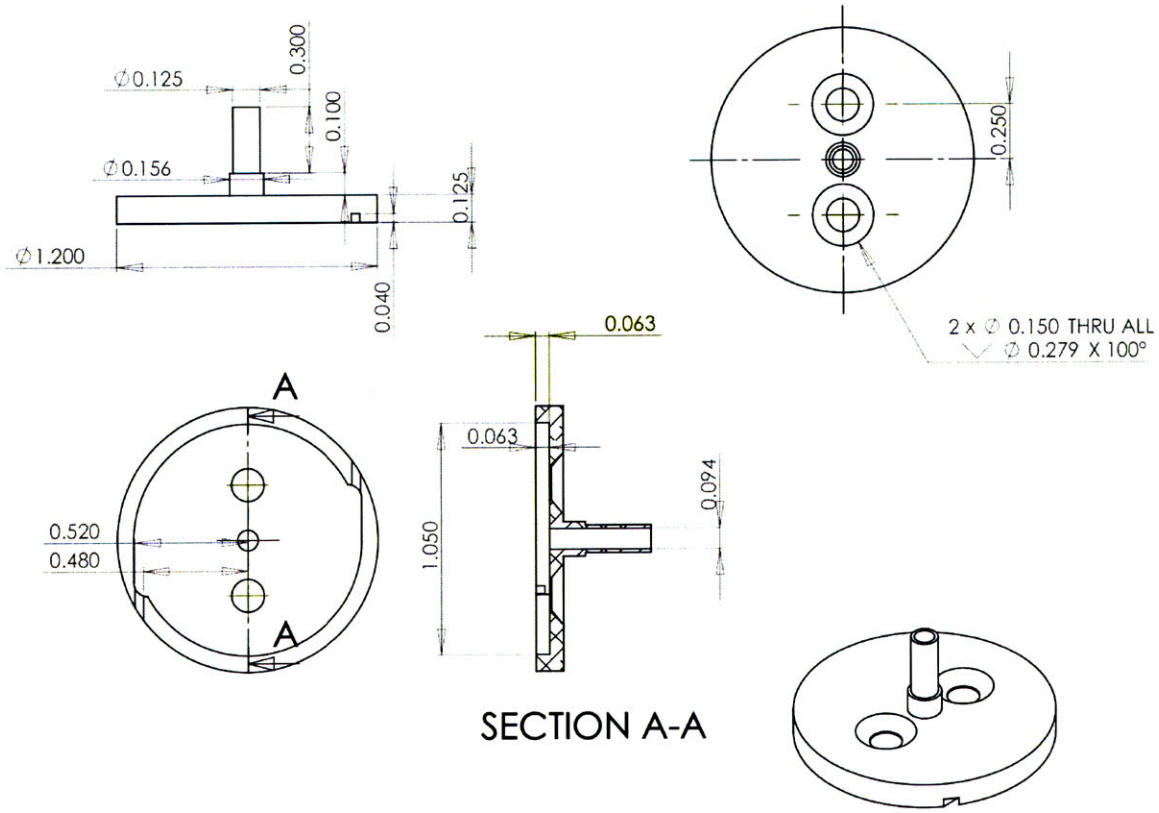

Figure 69. Rotor bottom piece drawing

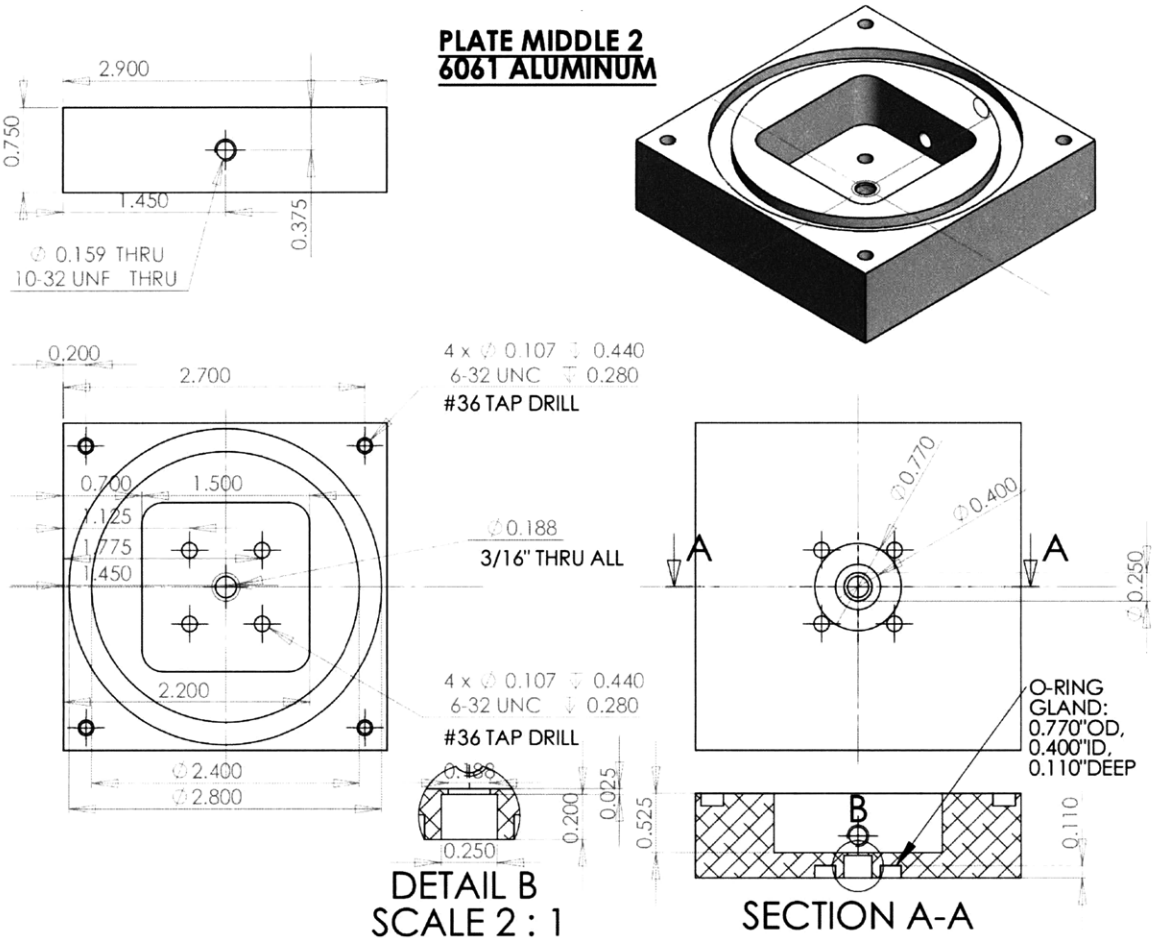

Figure 70. Stator middle plate drawing

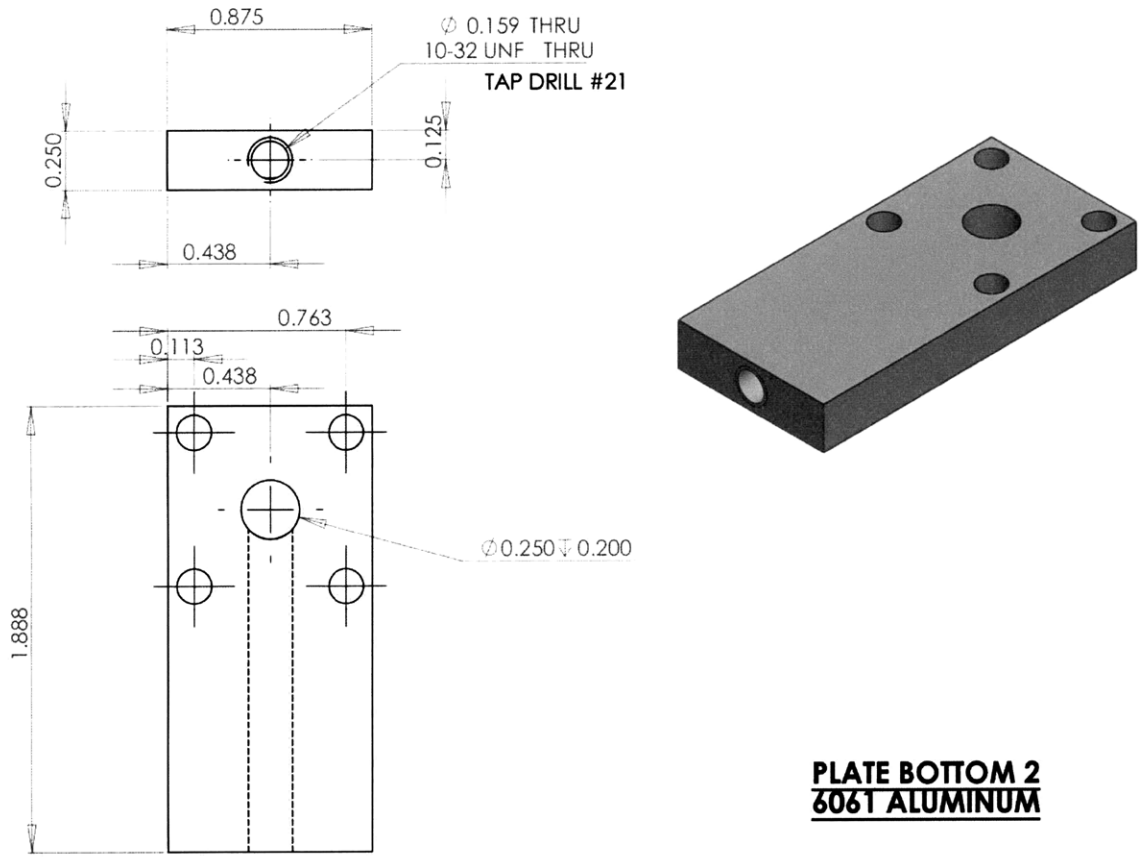

Figure 71. Stator bottom plate drawing

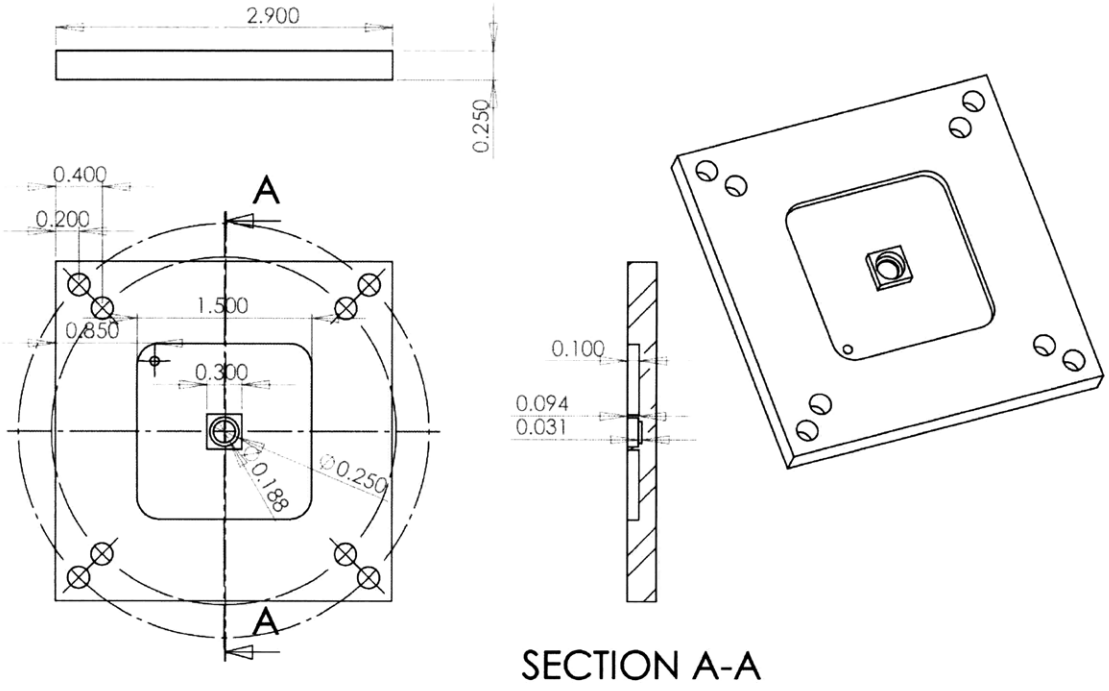

Figure 72. Stator top plate drawing

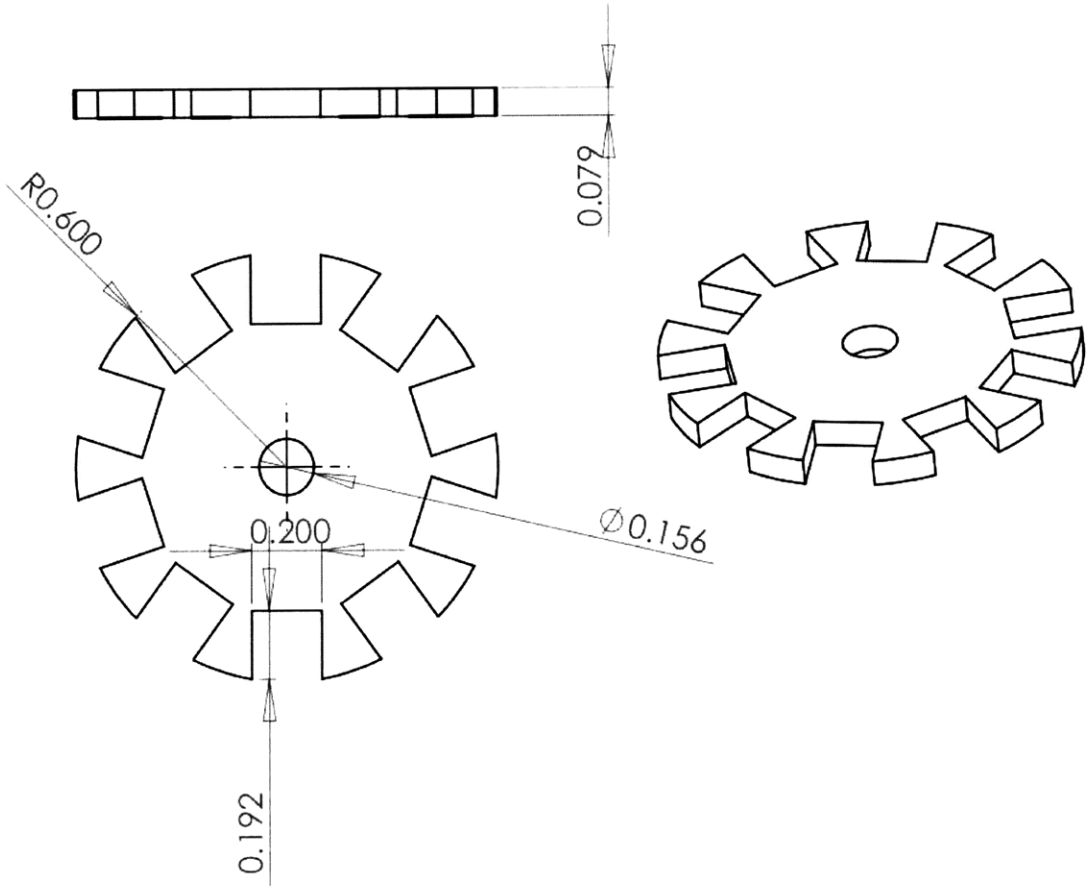

Figure 73. Magnet holder drawing

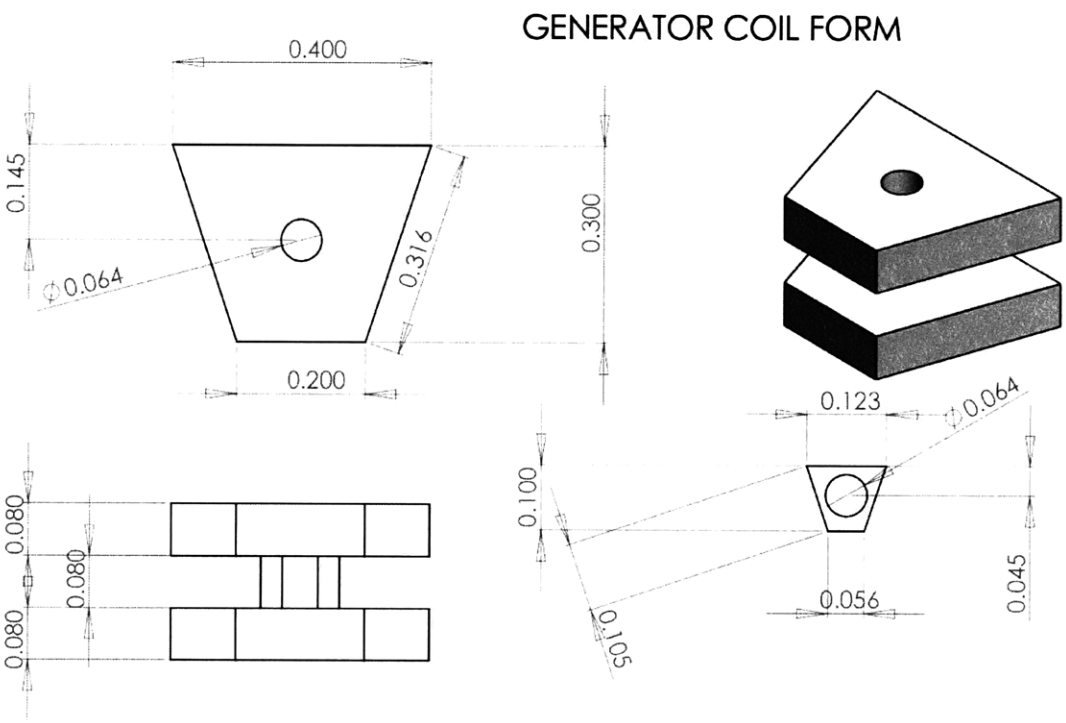

Figure 74. Generator coil form drawing